

Towards Practical Fixed-Wing Aircraft with Electroaerodynamic Propulsion

by

Arthur Brown

B.A.Sc., Engineering Science, University of Toronto (2016)
S.M., Aeronautics and Astronautics, Massachusetts Institute of Technology (2018)

Submitted to the Department of Aeronautics and Astronautics
in partial fulfillment of the requirements for the degree of

Doctor of Philosophy in Aeronautics and Astronautics

at the

Massachusetts Institute of Technology

June 2023

©2023 Arthur Brown. All rights reserved.

The author hereby grants to MIT a nonexclusive, worldwide, irrevocable, royalty-free license to exercise any and all rights under copyright, including to reproduce, preserve, distribute and publicly display copies of the thesis, or release the thesis under an open-access license.

Authored by: Arthur Brown
Department of Aeronautics and Astronautics
May 23, 2023

Certified by: Steven R.H. Barrett
H.N. Slater Professor of Aeronautics and Astronautics
Thesis supervisor

Certified by: Wesley L. Harris
Charles Stark Draper Professor of Aeronautics and Astronautics

Certified by: Mark Drela
Terry J. Kohler Professor of Aeronautics and Astronautics

Accepted by: Jonathan P. How
R. C. MacLaurin Professor of Aeronautics and Astronautics
Chair, Graduate Program Committee

Towards Practical Fixed-Wing Aircraft with Electroaerodynamic Propulsion
by
Arthur Brown

Submitted to the Department of Aeronautics and Astronautics on May 23, 2023
in partial fulfillment of the requirements for the degree of
Doctor of Philosophy in Aeronautics and Astronautics

ABSTRACT

Electroaerodynamic (EAD) propulsion is a novel means of generating thrust via collisions between ions and neutral molecules. EAD thrusters have no moving parts, and are therefore almost silent; they may therefore be useful for aircraft propulsion in applications where silence is valuable. Previous research has shown that EAD for fixed-wing, heavier-than-air aircraft propulsion is feasible. The goal of this thesis is to determine whether a fixed-wing EAD aircraft can be practical; i.e., with sufficient payload, range/endurance, and flight performance to be of interest in some initial application.

Two initial applications are identified, both of which may benefit from low noise: surveillance and last-mile package delivery. Nominal mission requirements are developed. Three aircraft design case studies are presented: an uncrewed aircraft powered by unducted EAD thrusters for a surveillance mission, a family of uncrewed aircraft powered by multistaged ducted (MSD) EAD thrusters for a package delivery mission, and an uncrewed MSD-powered monoplane for a surveillance mission. MSD thrusters are more powerful and efficient than equivalent unducted EAD thrusters, in part because the duct contributes to thrust. Multidisciplinary design optimization frameworks, including models for thruster performance, aerodynamics, structures, weights, and power electronics, are developed as part of the case studies.

Excess thrust for climb is the driving requirement for EAD fixed-wing flight: a practical aircraft requires more thrust than a feasible one, in order to climb. The MSD surveillance monoplane and package-delivery aircraft can fly their nominal missions, including climb requirements. However, they require improvements in three technological areas, relative to today's state of the art: efficient ion generation methods, low-pressure-loss thruster electrodes, and lightweight power converters are required. The package delivery mission also requires improvements in battery specific power. Plausible technological development paths in all four areas are identified.

EAD propulsion for surveillance and package delivery aircraft can be practical if the requisite technological improvements can be obtained. The technologies' identification, as well as the parameters by which improvement is quantified, is a key contribution of this thesis. Future work should focus on demonstrating the technological improvements, enabling the development of a fixed-wing, heavier-than-air EAD aircraft with practical capabilities.

Thesis Supervisor: Steven R.H. Barrett
Title: H.N. Slater Professor of Aeronautics and Astronautics

Acknowledgements

Firstly, I would like to acknowledge my thesis committee: Profs. Steven Barrett, Wesley Harris, and Mark Drela. I would also like to similarly acknowledge my thesis readers: Profs. Joaquim Martins and Prof. William Crossley. Over the years, you have all given me great advice (professional and otherwise); I've benefitted a lot from your perspectives.

Secondly, I would like to acknowledge my EAD colleagues. I could not have done this alone: I've been working within a larger team of graduate students and UROPs, and learning and benefitting from all of you. I particularly want to acknowledge Dr. Nicolas Gomez Vega. Over the years, I've learned a tremendous amount from you about EAD thruster physics; I have been equally impressed with your professionalism, as well as your putting up with my endless EAD-related questions.

Next, I would like to acknowledge my Laboratory for Aviation and the Environment (LAE) colleagues. I may not be the most extroverted individual around, but I still appreciate the effort that the lab members go to creating a welcoming environment. In particular, I would like to acknowledge the contributions of Prakash Prashanth and Carla Grobler: thank you both for all that you have done for me and for the LAE.

I would like to acknowledge my mentors, especially Profs. Steven Barrett and Wesley Harris. You've had my back when I needed it, and I appreciate that. Thanks in no small part to your support and advice, I feel ready to take the next steps in my career.

I would like to acknowledge my non-research friends and social groups. In particular, I would like to thank the Academy for Courageous Minorities in Engineering (ACME) membership and leadership, for welcoming me in as an international student still finding my way in America. I am grateful for ACME's safe and supportive environment, and I hope that I was able to help maintain a similar environment for other ACME members. I feel similarly about the Black Graduate Student Association (BGSA): another welcoming and supportive group. Finally, I would like to acknowledge the leaders of AeroAfro, which I co-founded almost five years ago. I feel confident leaving the organization in your hands.

I would like to acknowledge my family, including my siblings (Rebecca & Edgar), my parents, and my entire extended family. Thank you for continuing to support me during all the years that I've been away from home.

Lastly, but certainly not least, I would like to acknowledge Dr. Jordie Kamuene. After being on this PhD journey together for all these years, I am proud to finally write this paragraph using your new and well-earned professional title!

Table of contents

Acknowledgements	3
Table of contents	4
Nomenclature	9
Abbreviations	11
List of figures	12
List of tables	16
1 Introduction	19
1.1 Overview of electroaerodynamic propulsion	19
1.2 Literature review	19
1.3 Research question	22
1.4 Thesis contributions and structure	25
2 Characterization of EAD propulsion systems	26
2.1 Background and overview	26
2.2 Exposed EAD thrusters	26
2.2.1 Overview	26
2.2.2 Equations	28
2.2.3 Discussion	30
2.3 Ducted EAD thrusters	34
2.3.1 Overview	34
2.3.2 Equations	35
2.3.3 Discussion	38
2.4 Batteries	41
2.5 Power conversion	42

2.6	Chapter conclusions	44
3	Design of aircraft with exposed EAD thrusters	45
3.1	Background and overview.....	45
3.2	Methods.....	46
3.2.1	Mission requirements.....	46
3.2.2	Architecture enumeration.....	49
3.2.3	Multidisciplinary design optimization	54
3.2.4	Thruster models	56
3.2.5	Power-electronics models	57
3.2.6	Aircraft mass, drag, and structural models	58
3.2.7	Dimensional models.....	64
3.3	Results	68
3.3.1	Design optimization results.....	68
3.3.2	Architecture selection	70
3.3.3	Selected architecture overview	72
3.3.4	Prototyping and flight testing.....	75
3.3.5	Discussion: climb requirements	77
3.4	Chapter conclusions	82
4	Design of aircraft with ducted EAD thrusters for package delivery.....	83
4.1	Background and overview.....	83
4.2	Methods.....	86
4.2.1	Mission requirements.....	86
4.2.2	Architecture enumeration.....	87
4.2.3	Multidisciplinary design optimization	89

4.2.4	Thruster models	90
4.2.5	Power-electronics models	91
4.2.6	Aircraft mass, drag, and structural models	91
4.2.7	Dimensional models.....	95
4.3	Results	99
4.3.1	Design optimization results.....	99
4.3.2	Ionization energy	101
4.3.3	Stage loss coefficient	103
4.3.4	Power-converter specific power	108
4.3.5	Battery specific power	110
4.4	Chapter conclusions	112
5	Design of aircraft with ducted EAD thrusters for surveillance.....	113
5.1	Background and overview.....	113
5.2	Methods.....	113
5.2.1	Mission requirements.....	113
5.2.2	Vehicle architecture	114
5.2.3	Multidisciplinary design optimization	115
5.2.4	Thruster and power-electronics models	116
5.2.5	Aircraft mass, drag, and structural models	117
5.3	Results	118
5.3.1	Design optimization results.....	118
5.3.2	Comparison with the V3 biplane	120
5.3.3	Comparison with the MSD package-delivery aircraft	122
5.3.4	Climb requirements.....	123

5.3.5	Ionization energy	124
5.3.6	Stage loss coefficient	125
5.3.7	Power-converter specific power	126
5.3.8	Battery specific power	127
5.4	Chapter conclusions	128
6	Future work.....	129
6.1	Additional mission requirements	129
6.2	MSD thruster development	130
6.3	Power electronics modeling and development.....	130
6.4	Airframe prototyping and flight testing	131
6.5	Acoustic characterization	132
6.6	Environmental effects	133
6.7	Unsteady effects	134
7	Conclusions.....	136
Appendix A	Exposed thruster experimental data	141
Appendix B	Induced drag of biplanes and tandem wings	144
Appendix C	V3 wing structural model.....	145
Appendix D	V3 wing airfoil drag model	147
Appendix E	Thruster drag model adjustments for wake velocity	148
Appendix F	Cylinder drag model.....	149
Appendix G	V3 sketches	150
Appendix H	V3 dimensional data.....	151
Appendix I	V3 mass breakdown.....	153
Appendix J	V3 performance data	155

Appendix K	V3 aerodynamic design.....	157
Appendix L	V3 mass and drag model issues.....	161
Appendix M	Package delivery aircraft 3-view sketches	163
Appendix N	MSD thruster optimization model modifications.....	165
Appendix O	MSD box wing modeling details.....	166
Appendix P	Package delivery aircraft hover balance model.....	168
Appendix Q	Package delivery aircraft dimensional data.....	172
Appendix R	Package delivery aircraft mass breakdowns.....	175
Appendix S	Package delivery aircraft performance data	176
Appendix T	MSD surveillance monoplane 3-view sketches	180
Appendix U	MSD surveillance monoplane dimensional data.....	181
Appendix V	MSD surveillance monoplane mass breakdown	182
Appendix W	MSD surveillance monoplane performance data	183
References.....		184

Nomenclature

A	= cross-sectional area	p	= specific power
AR	= aspect ratio	$p(\mathbf{x})$	= posynomial function of \mathbf{x}
b	= span	Q	= drag interference factor
C	= tail volume coefficient	Re	= Reynolds number
C_D	= 3-dimensional drag coefficient	S	= area, or shear stress
C_d	= 2-dimensional drag coefficient	SA	= wetted surface area
C_f	= skin-friction coefficient	s	= factor of safety
C_L	= lift coefficient	$s(\mathbf{x})$	= signomial function of \mathbf{x}
c	= leading coefficient, or chord	T	= thrust
\bar{c}	= mean aerodynamic chord	$\frac{t}{c}$	= thickness-to-chord ratio
D	= drag	V	= voltage
D_i	= induced drag	Vol	= volume
d	= gap spacing, or diameter	v	= velocity
E	= energy, or Young's modulus	v_v	= rate of climb
e	= charge, or specific energy	W	= weight
e_{Oswald}	= Oswald efficiency	x	= design variable, or distance
FF	= form factor	\mathbf{x}	= vector of design variables
f	= mass fraction	ΔP	= total duct pressure rise
g	= gravitational acceleration	$(\Delta P)_{\text{EAD}}$	= stage EAD pressure rise
h	= height	$(\Delta P)_{\text{loss}}$	= stage pressure losses
j	= current density		
j_{MG}	= Mott-Gurney current density	β	= sideslip angle
K_L	= stage loss coefficient	γ	= climb angle
k	= constant	Δ	= deflection
L	= lift	ε	= electric permittivity
l	= length	η	= efficiency
m	= mass	λ	= taper ratio
$m(\mathbf{x})$	= monomial function of \mathbf{x}	μ	= ion mobility
\dot{m}	= mass flow rate	ν	= kinematic viscosity
N	= limit load factor	ρ	= air density
n	= number of stages	σ	= interference factor, or stress
P	= power, or pressure	ϕ	= thruster exit area ratio

$(\)$	= nondimensional property	$(\)_{\text{planar}}$	= planar wing property
$(\)_{\text{accel}}$	= ion acceleration property	$(\)_{\text{pod}}$	= fuselage pod property
$(\)_{\text{boom}}$	= tail or thruster boom property	$(\)_{\text{profile}}$	= profile drag property
$(\)_{\text{box}}$	= box wing property	$(\)_{\text{ref}}$	= reference property
$(\)_{\text{cap}}$	= spar cap property	$(\)_{\text{root}}$	= wing root property
$(\)_{\text{core}}$	= spar core property	$(\)_{\text{spar}}$	= wing spar property
$(\)_{\text{corona}}$	= corona thruster property	$(\)_{\text{usable}}$	= pod usable volume property
$(\)_e$	= thruster exit property	$(\)_V$	= vertical property
$(\)_{\text{eff}}$	= effective property	$(\)_{\text{VT}}$	= vertical tail property
$(\)_{\text{FT}}$	= forward thruster(s) property	$(\)_W$	= wing property
$(\)_H$	= horizontal property	$(\)_{\text{wall}}$	= duct wall property
$(\)_{\text{HT}}$	= horizontal tail property	$(\)_{\text{wire}}$	= electrode wire(s) property
$(\)_{\text{HVPC}}$	= power converter property	$(\)_1$	= freestream property
$(\)_{\text{in}}$	= input property	$(\)_2$	= duct entrance property
$(\)_{\text{iw}}$	= ionic-wind property	$(\)_3$	= duct exit property
$(\)_{\text{induced}}$	= induced drag property	$(\)_4$	= property far downstream
$(\)_{\text{ion}}$	= ion generation property	$(\)_\infty$	= freestream property
$(\)_{\text{out}}$	= output property		

Abbreviations

AAM	=	Advanced Air Mobility
AC	=	Alternating current
AVL	=	Athena Vortex Lattice
CAD	=	Computer-Aided Design
CG	=	Center of gravity
DBD	=	Dielectric barrier discharge
DC	=	Direct current
EAD	=	Electroaerodynamic
EHD	=	Electrohydrodynamic
EMI	=	Electromagnetic interference
FAA	=	Federal Aviation Administration
FEP	=	Fluorinated ethylene propylene
GP	=	Geometric programming
HALE	=	High-altitude long-endurance
HAPS	=	High-altitude pseudo-satellite
HVPC	=	High-voltage power converter
LE	=	Leading edge
MDO	=	Multidisciplinary design optimization
MG	=	Mott-Gurney
MIT	=	Massachusetts Institute of Technology
MSD	=	Multistaged ducted
NACA	=	National Advisory Committee for Aeronautics
NASA	=	National Aeronautics and Space Administration
NIAC	=	NASA Innovative Advanced Concepts
NRP	=	Nanosecond repetitively pulsed
RC	=	Radio control
RIE	=	Rotary ionic engine
RMS	=	Root mean square
SP	=	Signomial programming
TE	=	Trailing edge
TPS	=	Thermal protection system
UAM	=	Urban air mobility
UAV	=	Uncrewed aerial vehicle
VSP	=	Vehicle Sketch Pad
VTOL	=	Vertical takeoff and landing
V2	=	Version 2
V3	=	Version 3
2D	=	Two-dimensional
3D	=	Three-dimensional

List of figures

Figure 1: CAD rendering of the V2 EAD prototype airplane, from Ref. [14].	20
Figure 2: A diagram of an exposed wire-to-airfoil EAD thruster that uses a DC corona discharge to generate ions.	27
Figure 3: A diagram of an exposed, decoupled wire-to-airfoil EAD thruster that uses a dielectric barrier discharge to generate ions.	28
Figure 4: Thrust-to-power vs. thrust experimental data for several electrode gap spacings, taken from Ref. [18].	31
Figure 5: Voltage vs. thrust experimental data for several electrode gap spacings, taken from Ref. [18].	31
Figure 6: An array of exposed EAD thruster electrode pairs.	32
Figure 7: Normalized thrust vs. normalized electrode spacing for arrays of exposed wire-to-cylinder EAD thrusters. Experimental data is obtained from Gilmore & Barrett [9].	32
Figure 8: Side-view diagram of an MSD thruster, showing the inlet, duct, and nozzle.	35
Figure 9: Diagram of one MSD thruster stage.	35
Figure 10: An array of exposed EAD thruster electrode stages.	38
Figure 11: An MSD thruster with identical electrode array dimensions.	38
Figure 12: A schematic of the V2 power-conversion system, including the battery, power converter, and EAD thruster array. The power-converter circuit diagram is taken from Ref. [13].	42
Figure 13: Concept of operations for the V3.	46
Figure 14: An image of the RQ-11B Raven, taken from Ref. [73].	47
Figure 15: A leading-edge thruster.	49
Figure 16: A trailing-edge thruster.	49
Figure 17: A tandem thruster.	50
Figure 18: Multistaging, without alternating polarity.	51
Figure 19: Multistaging, with alternating polarity.	51
Figure 20: A monoplane configuration.	52
Figure 21: A biplane configuration.	52

Figure 22: A tandem wing configuration.....	52
Figure 23: Side view of the V3 biplane, showing the tail-boom dimensions.....	64
Figure 24: Mass breakdown for aircraft with exposed thrusters.....	69
Figure 25: Drag breakdown for aircraft with exposed thrusters.....	70
Figure 26: Loiter endurance vs. maximum planar wingspan, for vehicles with exposed thrusters.....	71
Figure 27: Side view of the V3, showing the thruster array design.....	72
Figure 28: The as-built V3 prototype, shown in the MIT Johnson track just before indoor flight testing. Left to right: Nicolas Gomez Vega, James (Jamie) Abel, the author, and Nicholas Perovich.....	75
Figure 29: The V3 on its launcher, in preparation for a flight test on MIT's Briggs field. Left to right: Christopher Vargas (holding the left wing), the author, and Alazar Lemma (holding the right wing).	76
Figure 30: Thrust vs. climb rate for the V3 at loiter speed.....	79
Figure 31: Thrust-to-weight ratio vs. climb rate for the V3 at loiter speed.....	79
Figure 32: Thrust-to-weight vs. climb rate.....	80
Figure 33: Endurance vs. climb rate.....	80
Figure 34: A potential alternate architecture for the V3, with an additional row of exposed thrusters.....	81
Figure 35: A potential alternate architecture for the V3, including a tandem wing with 3-stage integrated thrusters.....	81
Figure 36: Concept of operations for the MSD VTOL package-delivery aircraft.....	83
Figure 37: Isometric view of the monoplane in wingborne flight.....	88
Figure 38: Isometric view of the monoplane in hover.....	88
Figure 39: Isometric view of the box wing in wingborne flight.....	89
Figure 40: Isometric view of the box wing in hover.....	89
Figure 41: A cutaway of the monoplane fuselage pod.....	95
Figure 42: Front view of an MSD thruster duct, showing the electrode geometry.....	96
Figure 43: Mass breakdown for the MSD VTOL package-delivery aircraft.....	100
Figure 44: Cruise drag breakdown for the MSD VTOL package-delivery aircraft.....	100

Figure 45: Vehicle takeoff mass vs. ionization energy.....	101
Figure 46: Vehicle takeoff mass vs. stage loss coefficient	104
Figure 47: Side view of a proposed geometry for a streamlined electrode unit. Each unit consists of an emitter, a collector (black cylinders), and an ion source (yellow).....	106
Figure 48: Thruster stage loss coefficient as a function of grid geometry model for the monoplane.	107
Figure 49: Thruster stage loss coefficient as a function of grid geometry model for the box wing.	107
Figure 50: Vehicle takeoff mass vs. power-converter specific power.....	108
Figure 51: Vehicle takeoff mass vs. battery specific power	110
Figure 52: Isometric view of the surveillance monoplane.....	115
Figure 53: Mass breakdown for the MSD surveillance monoplane.	119
Figure 54: Loiter drag breakdown for the MSD surveillance monoplane.	119
Figure 55: Takeoff mass vs. required climb rate for the MSD surveillance monoplane.....	124
Figure 56: Takeoff mass vs. ionization energy for the MSD surveillance monoplane.....	125
Figure 57: Takeoff mass vs. stage loss coefficient for the MSD surveillance monoplane.....	125
Figure 58: Takeoff mass vs. power-converter specific power for the MSD surveillance monoplane.	126
Figure 59: Takeoff mass vs. battery specific power for the MSD surveillance monoplane.....	127
Figure 60: Thrust vs. thrust-to-power for a single-stage DC corona thruster with positive polarity.	141
Figure 61: Thrust vs. thrust-to-power for a single-stage DC corona thruster with negative polarity.	141
Figure 62: Thrust vs. thrust-to-power for a single-stage DBD thruster with positive polarity... 141	
Figure 63: Thrust vs. thrust-to-power for a two-stage thruster, with a negative DC corona first stage and a positive DC corona second stage. The first collector chord is 50 mm.....	142
Figure 64: Thrust vs. thrust-to-power for a two-stage thruster, with a negative DC corona first stage and a positive DC corona second stage. The first collector chord is 330 mm.....	142
Figure 65: Thrust vs. thrust-to-power for a two-stage thruster, with a negative DC corona first stage and a positive DBD second stage. The first collector chord is 50 mm.....	142

Figure 66: Thrust vs. thrust-to-power for a two-stage thruster, with a negative DC corona first stage and a positive DBD second stage. The first collector chord is 330 mm.....	142
Figure 67: Front view of the V3.....	150
Figure 68: Side view of the V3.....	150
Figure 69: Top view of the V3.....	150
Figure 70: Isometric view of the V3.....	150
Figure 71: The modified Aquila SM airfoil used for the V3 wing.....	157
Figure 72: The modified HT14 airfoil used for the V3 thruster collectors.....	157
Figure 73: AVL model of the V3.....	158
Figure 74: Trefftz plot for the V3, showing lift as a function of spanwise location Y (in cm)..	159
Figure 75: Front view of the monoplane in wingborne flight.....	163
Figure 76: Front view of the monoplane in hover.....	163
Figure 77: Side view of the monoplane in wingborne flight.....	163
Figure 78: Side view of the monoplane in hover.....	163
Figure 79: Top view of the monoplane in wingborne flight.....	163
Figure 80: Top view of the monoplane in hover.....	163
Figure 81: Front view of the box wing in wingborne flight	164
Figure 82: Front view of the box wing in hover.....	164
Figure 83: Side view of the box wing in wingborne flight	164
Figure 84: Side view of the box wing in hover.....	164
Figure 85: Top view of the box wing in wingborne flight.....	164
Figure 86: Top view of the box wing in hover	164
Figure 87: Side view of the monoplane, showing the hover balance model parameters.....	168
Figure 88: Side view of the box wing in hover (top), during transition (middle) and in wingborne flight (bottom). The thruster moment arms, the thruster pivot locations (blue circles with black crosses) and the center of gravity are also shown.....	169
Figure 89: Front view of the MSD surveillance monoplane.....	180
Figure 90: Side view of the MSD surveillance monoplane.....	180
Figure 91: Top view of the MSD surveillance monoplane.....	180

List of tables

Table 1: Specifications for the V2 EAD prototype.....	21
Table 2: The Wright Brothers' aircraft development milestones, taken from Refs. [50]–[52]....	23
Table 3: Pack-level battery sizing parameters for the V2, compared with existing batteries.....	41
Table 4: Sizing parameters for the V2 power converter.....	43
Table 5: Specifications for both versions of the Raven.	47
Table 6: Mission profile, showing the requirements for each mission segment.....	48
Table 7: V3 architectural options.....	53
Table 8: Problem formulation for a signomial program.	55
Table 9: Number of free variables, number of constraints, and typical solve times on a laptop computer for design optimization of the selected V3 architecture.	56
Table 10: Power-electronics sizing parameters.	58
Table 11: Aircraft-level sizing parameters for vehicles with exposed thrusters.....	58
Table 12: Mass models for vehicles with exposed thrusters.....	60
Table 13: Structural models for vehicles with exposed thrusters.	61
Table 14: Profile drag models for vehicles with exposed thrusters.	63
Table 15: Wing sizing parameters for vehicles with exposed thrusters.....	65
Table 16: Tail volume coefficients and aspect ratios for vehicles with exposed thrusters.....	67
Table 17: Summary of the design optimization results for aircraft with exposed thrusters.	68
Table 18: An overview of design optimization data from the V3, compared with the V2.....	73
Table 19: V3 thruster gap spacings.....	73
Table 20: Potential climb-rate requirements.....	78
Table 21: Characteristics of package delivery aircraft in development.....	86
Table 22: Mission profile, showing the requirements for each mission segment.....	87
Table 23: Number of free variables, number of constraints, and typical solve times on a laptop computer for design optimization of the package-delivery aircraft.	89
Table 24: Thruster model parameter values.....	90
Table 25: Power-electronics sizing parameters.	91
Table 26: Aircraft-level sizing parameters for vehicles with ducted thrusters.	92

Table 27: Mass, profile drag, and structural models for vehicles with ducted thrusters.	93
Table 28: Thruster and nacelle model parameter values.	97
Table 29: Tail volume coefficients for vehicles with ducted thrusters.	98
Table 30: Summary of the design optimization results for the MSD package-delivery aircraft. .	99
Table 31: Ionization energies for alternative ion sources.	102
Table 32: Stage loss coefficients, estimated using Equation (75).	105
Table 33: Mission profile for the MSD surveillance aircraft, showing the requirements for each mission segment.....	114
Table 34: Number of free variables, number of constraints, and typical solve times on a laptop computer for design optimization of the MSD surveillance monoplane.	115
Table 35: Thruster and power-electronics sizing parameters for the surveillance monoplane... .	116
Table 36: Profile drag models specific to the MSD surveillance monoplane.....	117
Table 37: Summary of the design optimization results for the MSD surveillance monoplane.. .	118
Table 38: Design parameters in the Breguet range equation for the V3 biplane and the MSD surveillance monoplane.	120
Table 39: Summary of mission requirements and input parameters that differ between the MSD surveillance and MSD package-delivery vehicles.	123
Table 40: Emitter wire local Reynolds numbers and associated flow regimes.	135
Table 41: Data summary for the EAD aircraft designed in this thesis, as well as for the V2. ...	139
Table 42: Exposed thruster fit RMS errors.	143
Table 43: Detailed dimensional data for the V3.	151
Table 44: Mass breakdown for the V3.....	153
Table 45: Detailed performance data for the V3.	155
Table 46: Incidence and dihedral angles for the V3 components.	158
Table 47: Requirements and analysis results for each flight condition analyzed in AVL.....	159
Table 48: Estimated center-of-gravity locations for the monoplane and box wing.....	170
Table 49: Results from the hover balance analysis.....	170
Table 50: Dimensional data for the monoplane.....	172
Table 51: Dimensional data for the box wing.....	174
Table 52: Mass breakdown for the monoplane.....	175

Table 53: Mass breakdown for the box wing aircraft	175
Table 54: Mission segment time, distance travelled, and battery energy consumed.....	176
Table 55: Performance data by mission segment for the monoplane.	176
Table 56: Performance data by mission segment for the box wing.	178
Table 57: Dimensional data for the MSD surveillance monoplane.....	181
Table 58: Mass breakdown for the MSD surveillance monoplane.....	182
Table 59: Performance data by mission segment for the MSD surveillance monoplane.	183

1 Introduction

1.1 Overview of electroaerodynamic propulsion

Electroaerodynamic (EAD) propulsion, also known as electrohydrodynamic (EHD) propulsion, is a novel means of generating thrust in air without any moving parts. EAD thrusters work by generating ions near an emitter electrode, and accelerating them towards a collector electrode by applying a voltage between the emitter and collector. While travelling to the collector, the ions collide with other neutral molecules, which then accelerate, forming an ionic wind. Thrust is generated via Newton's Third Law: neutral molecules are forced backwards, so the neutral molecules then push the thruster forwards.

The main hypothesized advantage of EAD propulsion for aircraft (relative to propellers) is reduced noise, due to the lack of moving parts. This may be an advantage because noise from aircraft operations can annoy local residents, leading to community opposition towards said operations. This is a known issue for helicopters [1], urban air taxis [2], and uncrewed aerial vehicles [3], [4], as well as for other types of aircraft. Initial acoustic experiments suggest that an EAD thruster can be 20 dB quieter (99% quieter, or two orders of magnitude quieter) than a propeller, while producing the same amount of thrust [5].

1.2 Literature review

The first peer-reviewed experimental study on EAD propulsion for in-atmosphere applications was published by Christenson & Moller in 1967 [6]. They conducted a theoretical and experimental analysis, showing that thrust can be generated using EAD. Experimental work by Masuyama & Barrett [7] obtained EAD thrust-to-power ratios comparable to or greater than typical values for modern jet engines. These findings were broadly confirmed by Monrolin et al. [8]. In a follow-on study, Gilmore & Barrett [9] theoretically and experimentally quantified EAD thrust density. While the obtained thrust densities were at least two orders of magnitude lower than that of a typical jet engine and about half as large as those of propellers, they were (in theory) still high enough to power a small uncrewed aerial vehicle (UAV).

EAD thrusters typically require electrode voltages on the order of tens of kilovolts, higher than what could be obtained from batteries onboard a small UAV. A high-voltage power converter

(HVPC) was developed by He et al. [10], [11] to generate the required high voltages. Its specific power (output power divided by mass) was approximately 1.03 kW/kg, 5-10 times higher than existing off-the-shelf solutions*. A power converter with a similar application and specifications was developed later by Zhao et al. [12].

These advances in EAD thruster and power-conversion technology were combined in the first fixed-wing, heavier-than-air EAD airplane to achieve steady level flight [13], [14]. This aircraft was developed at MIT; it is hereafter referred to as the V2, or Version 2[†]. It had eight EAD thrusters, arranged in an array. It also carried a lithium-ion battery pack, power from which was provided to the thruster array via the power converter. The aircraft was radio-controlled, with two servos (elevator and rudder) and an RC transmitter and receiver. It achieved steady level flight in November 2017, demonstrating that “solid-state” fixed-wing electric flight (i.e., without any moving parts in its propulsion system) is feasible. The V2 development and test flights were reported by Xu et al. [13]; additional details are given by Gilmore [15] and by Brown et al. [14].

A CAD rendering of the V2, taken from Ref. [14], is shown in Figure 1.

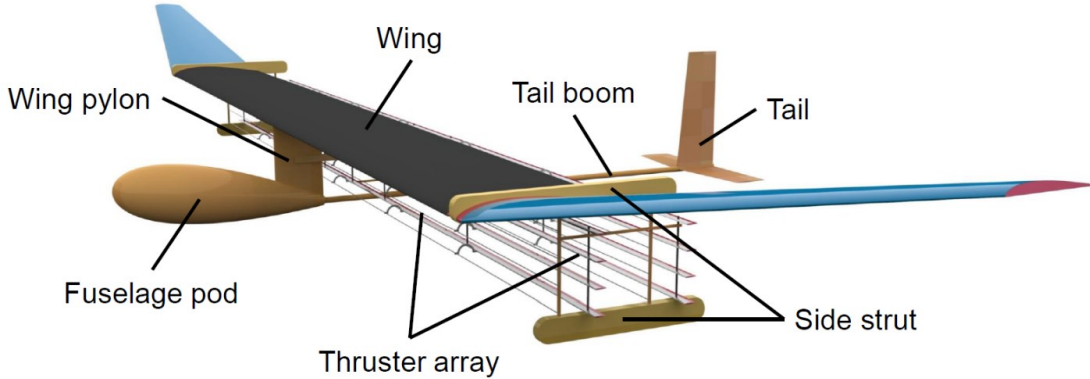


Figure 1: CAD rendering of the V2 EAD prototype airplane, from Ref. [14].

Specifications for the V2, obtained from [13], [14], are given in Table 1.

* Power converters with similar voltage and power requirements are used in X-ray machines and electrostatic precipitators [10]. These applications are ground-based, where mass is less of a concern than for aircraft.

[†] Two earlier aircraft prototypes were built. The first was the V0, which was used to develop and improve the structural and mass models used for design. The second was the V1, which was not capable of maintaining steady level flight.

Table 1: Specifications for the V2 EAD prototype.

Length	2.0 m
Wingspan	5.14 m
Wing aspect ratio	17.9
Thruster gap spacing	50 mm
Takeoff mass	2.45 kg
Battery mass	0.23 kg
Power-converter mass	0.51 kg
Cruising speed	4.8 m/s
Thrust	3.2 N
Lift-to-drag ratio	8
Battery nominal voltage	200 V
Thruster operating voltage	40.3 kV
Battery power draw	620 W
Power-converter efficiency	85%
Endurance	90 s

While the V2 aircraft represents a step forward for EAD technology, it cannot be described as practical. It only ever flew indoors, it carried no payload, and its endurance was limited to 90 s. Also, its overall efficiency (defined as the product of thrust and flight speed, divided by battery power draw) was 2.5%. For comparison, battery-powered electric aircraft are expected to have overall efficiencies of 70-90% [16].

Research into the design and development of EAD thrusters at MIT has continued since the V2 test flights. For example, Xu et al. [17] conducted experiments on decoupled thrusters with a dielectric barrier discharge (DBD) ion source; they obtained improvements in both thrust per unit span and thrust-to-power, compared to the thrusters used on the V2. A study led by the same author [18] showed that improvements in thrust per span and thrust-to-power can also be obtained by increasing the thruster gap spacing; leakage current and reverse emission, two non-ideal effects that reduce thruster performance, were identified and quantified. Research and development at MIT into decoupled thrusters [19], [20] and reverse emission [21] was continued by other authors.

The studies referenced in the preceding paragraph are mostly experimental, but theoretical developments have occurred as well. For example, Gilmore & Barrett [22] developed theoretical

models for the effects of altitude and freestream velocity on EAD thruster performance. Gomez-Vega et al. [23] developed models for multistaged ducted (MSD) EAD thrusters, in which multiple miniaturized EAD thruster stages are enclosed in a duct. They showed that MSD EAD thrusters can be more thrust-dense and more efficient than their exposed counterparts. This is in part because the duct contributes to thrust, as is the case in ducted fans. Numerical methods at various levels of fidelity have also been applied to model EAD thrusters [18], [24], [25].

While this research is focused on EAD propulsion for fixed-wing, heavier-than-air aircraft, other approaches are available. For example, Casado & Greig [26] develop a conceptual design of a fixed-wing planetary flyer for exploration of Mars. Their vehicle was powered by DBD thrusters on the upper wing surface; it required wireless power transmission from a ground-based source. Note that the term “aircraft” is by definition restricted to vehicles that fly in air; i.e., in Earth’s atmosphere. Meanwhile, Poon et al. [27] and He et al. [28] developed EAD-powered, lighter-than-air blimps, and flight tested them indoors. Khomich & Rebrov [29] developed a heavier-than-air vertical lifter, or ionocraft, power for which was beamed wirelessly. Drew et al. [30] developed a much smaller ionocraft (about 2 cm across and weighing only 30 milligrams), power for which was provided via a tether. Finally, a rotary ionic engine (RIE) produces thrust by using an EAD device to turn a propeller. Ieta & Chirita [31] developed a rotary ionic engine, and tested it in air, carbon dioxide, and sulfur hexafluoride; the same authors [32] also developed and tested an RIE with contra-rotating propellers. Applications for EAD devices other than propulsion include flow control [33]–[35], aircraft and helicopter noise reduction [36]–[38], fluid pumping [39]–[42], heat transfer enhancement [43]–[45], and air purification via electrostatic precipitation [46]–[49].

1.3 Research question

Previous research [13] has demonstrated that EAD propulsion for fixed-wing aircraft is *feasible*: a fixed-wing, heavier-than-air aircraft powered entirely via EAD (the V2) has achieved steady level flight. However, whether and how EAD aircraft propulsion can be made *practical* has yet to be determined. The research question posed in this thesis can therefore be stated as follows:

Can a practical EAD-powered aircraft be designed and built? A practical aircraft is defined as one with sufficient payload, range and/or endurance, and flight performance to be of interest in some initial application.

Several aspects of this research question deserve discussion. Firstly, the term “aircraft” is restricted to mean a fixed-wing, heavier-than-air vehicle capable of steady level flight under its own power. Aircraft without fixed wings, lighter-than-air aircraft, aircraft lacking an onboard power source[‡], and gliders are excluded from this definition. Secondly, answering this question requires initial applications for EAD to be identified, from which payload, range/endurance, and flight performance requirements for a nominal mission can be determined. The two applications studied in this thesis are surveillance (Chapters 3 and 5) and last-mile package delivery (Chapter 4) missions. A practical aircraft is defined as an aircraft that meets the respective mission requirements. Finally, answering the research question does not necessarily require an aircraft meeting the mission requirements to be built and flight tested; it only requires that one be designed. For this reason, Chapter 3 is primarily focused on design (rather than flight testing), while Chapters 4 and 5 do not include flight testing.

The research question refers to a practical EAD aircraft, rather than an aircraft that is merely feasible (like the V2), or one that has been commercialized. In order to clarify the difference between these three terms (feasible, practical, and commercialized), the Wright Brothers’ aircraft development timeline is used as a case study. Their key milestones, including their first feasible, practical, and commercialized aircraft, are summarized in Table 2 [50]–[52].

Table 2: The Wright Brothers’ aircraft development milestones, taken from Refs. [50]–[52].

	Feasible	Practical	Commercialized
Date and location	December 1903; Kitty Hawk, North Carolina.	September 1905; Huffman Prairie, Ohio.	June/July 1909; Fort Myer, Virginia.
Aircraft name	Flyer I	Flyer III	Military Flyer
Flight performance	First flight: 37 m; 12 s. Longest flight: 260 m; 59 s.	Performance: banks, turns, figure eights; >38-min endurance.	Flew 16.1 km in 15 min with 1 passenger; average speed of 19.0 m/s. Endurance: 72 min.

[‡] Aircraft can alternatively have a ground-based power source. Power is then supplied via a tether or via beamed (wireless) power, as in Casado & Greig [26], Khomich & Rebrov [29], and Drew et al. [30].

Table 2 shows that the Wright Brothers' first feasible aircraft was the Flyer I [50], [51]. This aircraft made four successful flights in December 1903, the last and longest of which lasted almost a minute. The analogous achievement for EAD aircraft was the V2 test flights, each of which lasted approximately 12 s and covered a distance of about 37 m [13]. The Flyer I and the EAD V2 were both feasible; they both represented substantial steps forward for their respective technologies. However, neither aircraft was capable of meeting requirements sufficient to be of interest in an initial application. They cannot therefore be described as practical.

The Wright Brothers' first practical aircraft, called the Flyer III, flew almost two years later [51]. While similar in appearance to the Flyer I, it was a far more capable machine. Unlike its predecessor, it was capable of banks, turns, and figure eights; its longest flight lasted almost 40 minutes. The goal of this thesis is to determine whether similar performance can be achieved with an EAD-powered aircraft. However, the Flyer III was not designed for a specific set of mission requirements. Instead, its main purpose was to demonstrate that sustained, controllable fixed-wing flight was possible. By contrast, this thesis identifies a suitable set of payload, range/endurance, and flight performance requirements.

The Wright Brothers did not sell their first airplane for another four years. This was finally achieved in mid-1909, with the sale of the first Military Flyer to the United States Army [51], [52]. The Army required the Military Flyer to stay aloft with a passenger for at least an hour, and to fly 16.1 km in less than 40 minutes; both requirements were met. The Military Flyer thus became the world's first commercialized aircraft.

Beyond demonstrating practical capabilities, several additional challenges require solutions before an EAD-powered aircraft can be commercialized. For example, ion mobility (a key parameter affecting the performance of EAD systems; see Chapter 2) is known to be sensitive to atmospheric conditions, especially air pressure and humidity [53], [54]. These effects, and their implications for EAD aircraft design, would have to be quantified before a commercial EAD-powered aircraft can be developed. Similarly, issues regarding sensitivity of EAD thrusters to dust, rain, and snow would have to be solved. EAD thrusters would have to be reliable and maintainable, and a business case is required. By restricting the research question to practical (rather than commercialized) EAD aircraft, these issues are beyond the scope of this thesis.

1.4 Thesis contributions and structure

The contributions of this thesis can be summarized as follows. Firstly, mission requirements are identified for two prospective initial applications of EAD aircraft (surveillance and last-mile package delivery), including payload, range/endurance, and flight performance requirements. Secondly, multidisciplinary design optimization frameworks for the design of practical EAD-powered aircraft are developed. The frameworks include models for EAD thruster performance, as well as aerodynamic, structural, mass, and power-electronics models. Finally, an assessment of the applicability of EAD propulsion to both candidate missions is conducted. This thesis identifies four areas in which technological improvements (relative to today's state of the art) are required for EAD aircraft to be practical. Each technological area is parameterized quantitatively, the extent to which improvements are required is determined, and plausible development paths to obtain the required improvements are discussed.

The rest of this thesis is structured as follows. EAD propulsion systems, including exposed EAD thrusters, ducted EAD thrusters, batteries, and power converters, are characterized to a level of detail suitable for aircraft design in Chapter 2. A flight demonstrator aircraft powered by exposed EAD thrusters is designed, built, and flight tested (with a substitute propulsion system) for a nominal surveillance mission in Chapter 3. Next, two aircraft concepts powered by multistaged ducted EAD thrusters are designed for a package delivery mission in Chapter 4. Another concept design study of an aircraft powered by multistaged ducted EAD thrusters, but for a surveillance mission, is presented in Chapter 5. Future work is presented in Chapter 6, before the conclusion in Chapter 7.

2 Characterization of EAD propulsion systems

2.1 Background and overview

The goal of this chapter is to characterize EAD propulsion systems, including thrusters, batteries, and power converters, to a level of detail sufficient to design EAD airplanes. EAD aircraft research is at the intersection of three research disciplines: ionized gases, the branch of physics behind EAD thrust generation; power electronics, which is necessary to design the power converter; and aircraft design, in which thruster and power-converter technology is incorporated into an airframe. This thesis is concerned primarily with the aircraft design aspects of EAD research. While EAD propulsion systems are characterized in this chapter, the principal focus of this thesis (Chapters 3, 4, and 5) is on the design of EAD-powered aircraft. EAD thruster and power-converter technology are covered in more detail in Refs. [7], [9], [17]–[23] and Refs. [10], [11] respectively.

The rest of this chapter is structured as follows. Exposed EAD thrusters are characterized in Section 2.2. Next, ducted EAD thrusters, in which the EAD electrodes are contained inside a duct, are characterized in Section 2.3. Batteries and power converters, including sizing parameters based on the V2 system, are characterized in Sections 2.4 and 2.5 respectively, before the chapter conclusions in Section 2.6.

The model for ducted thrusters in Section 2.3.2 is based on a model developed by Nicolas Gomez Vega, reviewed by the author, and published in Ref. [23]. The model was extended to include duct wall drag by the author; this extended form was previously published by the author and collaborators in Ref. [5]. The model for direct comparison with exposed thrusters in Section 2.3.3 was derived by the author, with some assistance from Nicolas Gomez Vega. Most of the remaining content in this chapter references models developed by other authors.

2.2 Exposed EAD thrusters

2.2.1 Overview

An exposed EAD thruster consists of an emitter electrode and a collector electrode, both of which are exposed to the freestream. The terms *exposed thruster* or *unducted thruster* are used to draw a distinction with ducted EAD thrusters (discussed in Section 2.3); these two terms are used interchangeably in this thesis. The V2 was powered by an array of eight exposed thrusters.

An exposed EAD thruster with a wire-to-airfoil electrode geometry is depicted in Figure 2.

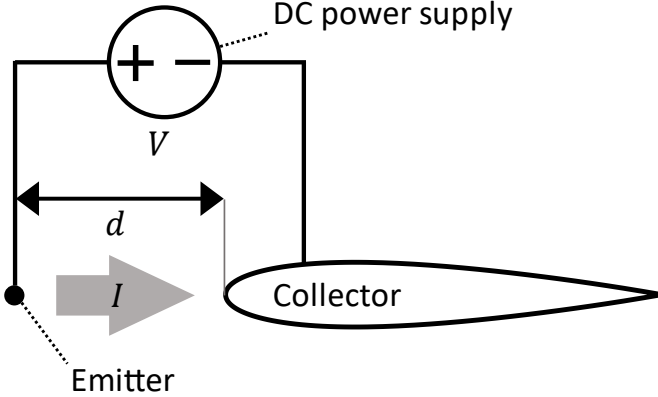


Figure 2: A diagram of an exposed wire-to-airfoil EAD thruster that uses a DC corona discharge to generate ions.

The thruster in Figure 2 consists of an emitter electrode (a cylindrical wire, extending into the page) and a collector electrode (an airfoil, also extending into the page), separated by a gap spacing d . The electrodes are connected by a DC power supply with voltage V , causing an ion current I to flow from the emitter to the collector. Electrode geometries other than wire-to-airfoil have been described in the literature; examples include pin-to-ring [6], wire-to-cylinder [18], and pin-to-mesh [39] geometries.

The thruster in Figure 2 generates ions via a DC corona discharge, a self-sustaining gas discharge that can occur when a DC voltage is applied between two electrodes with an asymmetric geometry [21]. Above a critical voltage known as the corona inception voltage, ions are generated near the electrode with the smaller radius of curvature (i.e., the emitter). DC corona thrusters can generate either positive or negative ions, depending on the polarity of the applied voltage.

In a corona thruster, ion generation and acceleration are coupled: the DC voltage in Figure 2 controls both the ion generation and acceleration processes. This approach has the advantage of simplicity [13]; it is the approach typically used by EAD-powered aircraft in the literature, including the V2 [13], [29], [30]. The alternative is a decoupled thruster, in which the ion generation and acceleration processes are controlled separately. A decoupled wire-to-airfoil thruster is shown in Figure 3.

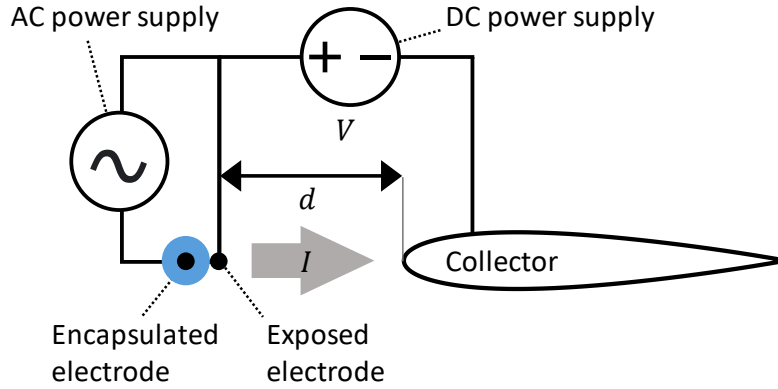


Figure 3: A diagram of an exposed, decoupled wire-to-airfoil EAD thruster that uses a dielectric barrier discharge to generate ions.

Figure 3 includes the applied DC voltage and ion current, as with corona thrusters. However, Figure 3 also includes an AC power supply, connected to a third electrode encapsulated by a dielectric material (blue). This system generates ions via a mechanism known as dielectric barrier discharge (DBD). The AC power supply controls ion generation, while the DC power supply controls ion acceleration; the two processes are thus decoupled. As discovered by Xu et al. [17] and mentioned in Section 1.2, DBD thrusters may offer improvements in both thrust per unit span and thrust-to-power, relative to corona thrusters.

Decoupled thrusters may use ion sources other than DBDs. Example potential ion sources include nanosecond repetitively pulsed (NRP) discharges, the photoelectric effect, photoionization, electron impact, and radioactive decay. These ion sources are discussed in more detail in Ref. [5].

2.2.2 Equations

Physics-based models for both corona and decoupled EAD thrusters are developed in this section. The derivation assumes a steady-state system, and static flow (i.e., zero freestream velocity).

Under these circumstances, the ion current in a corona thruster (Figure 2) can be estimated [21] as

$$\left(\frac{I}{b}\right)_{\text{corona}} = \begin{cases} 0 & \text{for } |V| < |V_0| \\ C_0 \varepsilon \mu \frac{V(V - V_0)}{d^2} & \text{for } |V| \geq |V_0| \end{cases} \quad (1)$$

where I is the current, b is the thruster span, the constant C_0 is a function of electrode geometry, ε is the electric permittivity, μ is the ion mobility, V is the applied voltage, V_0 is the corona inception voltage, and d is the gap spacing.

A decoupled thruster (Figure 3) can be modeled by assuming that the current travels in a thin collisional channel between the emitter and collector, and that the current is limited by space charge. This problem was first studied by Geurst [55] for semiconductor layers, and was subsequently extended by other authors [56], [57]. The resulting equation for current is

$$\left(\frac{I}{b}\right)_{\text{decoupled}} = \frac{2}{\pi} \varepsilon \mu \frac{V^2}{d^2} \quad (2)$$

The leading coefficient in Equation (2) is in general a function of electrode geometry; the factor of $\frac{2}{\pi}$ used here applies if the emitter and collector are modeled as semi-infinite coplanar electrodes [57]. Equation (2) is hereafter referred to in this thesis as the Geurst law.

Thrust can then be predicted as a function of current, using a model derived by Pekker & Young [58]. Normalizing their result by thruster span yields

$$\frac{T}{b} = \frac{d I}{\mu b} \quad (3)$$

where T is thrust. Finally, electrical power draw can be predicted for corona thrusters as

$$\left(\frac{P}{b}\right)_{\text{corona}} = \left(\frac{P}{b}\right)_{\text{accel}} = V \left(\frac{I}{b}\right)_{\text{corona}} \quad (4)$$

and for decoupled thrusters as

$$\left(\frac{P}{b}\right)_{\text{decoupled}} = \left(\frac{P}{b}\right)_{\text{ion}} + \left(\frac{P}{b}\right)_{\text{accel}} \quad (5)$$

$$\left(\frac{P}{b}\right)_{\text{ion}} = \frac{E_{\text{ion}} I}{e b} \quad (6)$$

$$\left(\frac{P}{b}\right)_{\text{accel}} = V \frac{I}{b} \quad (7)$$

where P is the electrical power draw, the subscripts $(\)_{\text{ion}}$ and $(\)_{\text{accel}}$ refer to ion generation and ion acceleration respectively, E_{ion} is the amount of energy required to generate one ion, and e is the elementary charge.

Equation (5) includes separate terms for ion generation and acceleration power, because these processes are separate for decoupled thrusters (Section 2.2.1). Equation (6) shows that ionization power is directly proportional to E_{ion} , the amount of electrical energy required to generate one ion.

The results in Chapter 4 (Section 4.3.2.2) show that E_{ion} varies depending on the ion source, and that ion sources with lower ionization energies can be used to improve EAD aircraft performance.

Ion generation and acceleration mechanisms are coupled for a corona thruster, so a separate term for ionization power in Equation (4) is not required. Instead, ionization power is included implicitly, via the current in Equation (1).

To summarize, corona EAD thrusters can be modeled using Equations (1), (3), and (4). Decoupled thrusters can be modeled using Equations (2), (3), and (5)-(7).

2.2.3 Discussion

Equations (2), (3), and (5)-(7) for decoupled thrusters can be rearranged to yield thrust and thrust-to-power as a function of voltage, gap spacing, and physical constants. If ionization energy is neglected, the result is

$$\frac{T}{b} = \frac{2}{\pi} \varepsilon \frac{V^2}{d} \quad (8)$$

$$\frac{T}{P} = \frac{1}{\mu} \frac{d}{V} \quad (9)$$

Equations (8)-(9) show that there is a tradeoff between thrust and thrust-to-power: manipulating an independent variable to increase thrust will decrease thrust-to-power, and vice versa. For example, Equation (8) shows that increasing voltage increases thrust, but Equation (9) shows that increasing voltage decreases thrust-to-power. The opposite is true for changes in gap spacing.

However, Equations (8)-(9) show that it may be possible to manipulate voltage and gap spacing together, in order to obtain a benefit to one metric without compromising the other. For example, consider what would happen if voltage and gap spacing are doubled simultaneously. Equation (8) shows that thrust is proportional to $\frac{V^2}{d}$, and would therefore double if voltage and gap spacing are both doubled simultaneously. Meanwhile, Equation (9) shows that thrust-to-power is proportional to $\frac{d}{V}$, and would therefore be unaffected. This suggests that better thruster performance can be obtained at higher gap spacings and voltages. A similar theoretical argument can be made for corona thrusters.

Experimental EAD corona-thruster data, including thrust, thrust-to-power, and voltage for several electrode gap spacings, was taken from Ref. [18]. Figures 7(a) and 7(b) from that reference are reproduced here as Figure 4 and Figure 5 respectively.

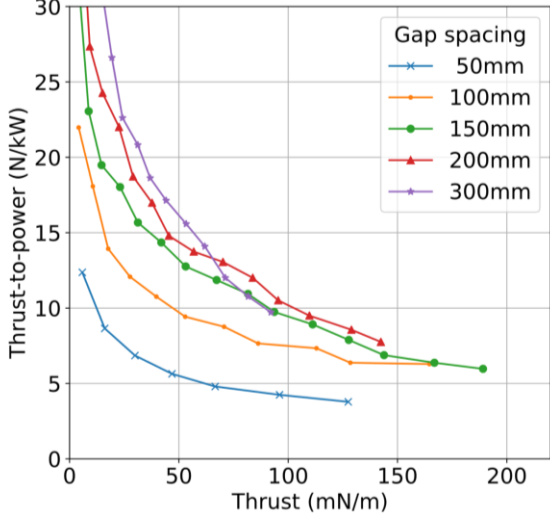


Figure 4: Thrust-to-power vs. thrust experimental data for several electrode gap spacings, taken from Ref. [18].

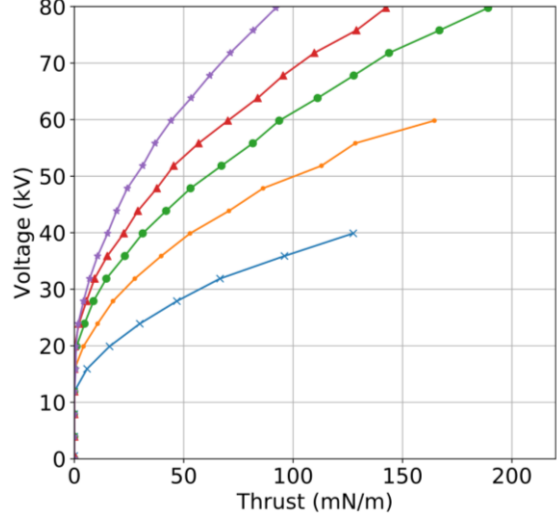


Figure 5: Voltage vs. thrust experimental data for several electrode gap spacings, taken from Ref. [18].

Figure 4 shows that for a fixed electrode gap spacing, an increase in thrust tends to result in a decrease in thrust-to-power, and vice versa. This observation is consistent with the arguments made above using Equations (8)-(9). Figure 4 also shows that the tradeoff between thrust and thrust-to-power improves at higher gap spacings: for a fixed thrust, the thrust-to-power is greater at a higher gap spacing; for a fixed thrust-to-power; the thrust is greater at a higher gap spacing. Figure 5 shows that this improvement can only be obtained at higher voltages: for a fixed thrust, an increase in thrust-to-power requires a higher voltage. Finally, the blue data points in Figure 4 and Figure 5 correspond to a gap spacing of 50 mm, the same value as the V2 thrusters (Table 1). Better performance is obtained, relative to these thrusters, at higher gap spacings. Therefore, it can be predicted theoretically and demonstrated experimentally that better EAD thruster performance for a fixed thruster span, relative to the performance achieved by the V2 thrusters, can be obtained at higher gap spacings and voltages.

However, practical considerations limit the benefits that can be achieved by simply increasing the gap spacing and voltage. They are as follows:

Electrode array size: a larger gap spacing implies a larger thruster array, with greater mass and drag. Recall from Section 1.2 that the V2 was powered by eight emitter-collector pairs, arranged in an array. A diagram of the V2 thruster array, with $n = 2$ stages and $k = 4$ electrode pairs per stage, is shown in Figure 6.

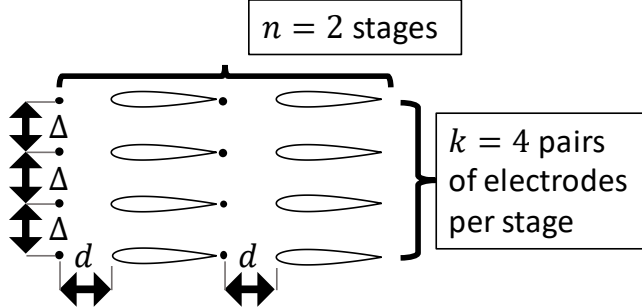


Figure 6: An array of exposed EAD thruster electrode pairs.

Figure 6 shows that each electrode pair in a stage is separated by a vertical spacing Δ . A normalized electrode pair spacing $\frac{\Delta}{d}$ can also be defined. Experimental thrust data from wire-to-cylinder EAD corona thruster arrays was collected by Gilmore & Barrett [9] as a function of $\frac{\Delta}{d}$. Figure 5 of that reference is summarized here as Figure 7. Thrust is normalized to its value when $\Delta = d$.

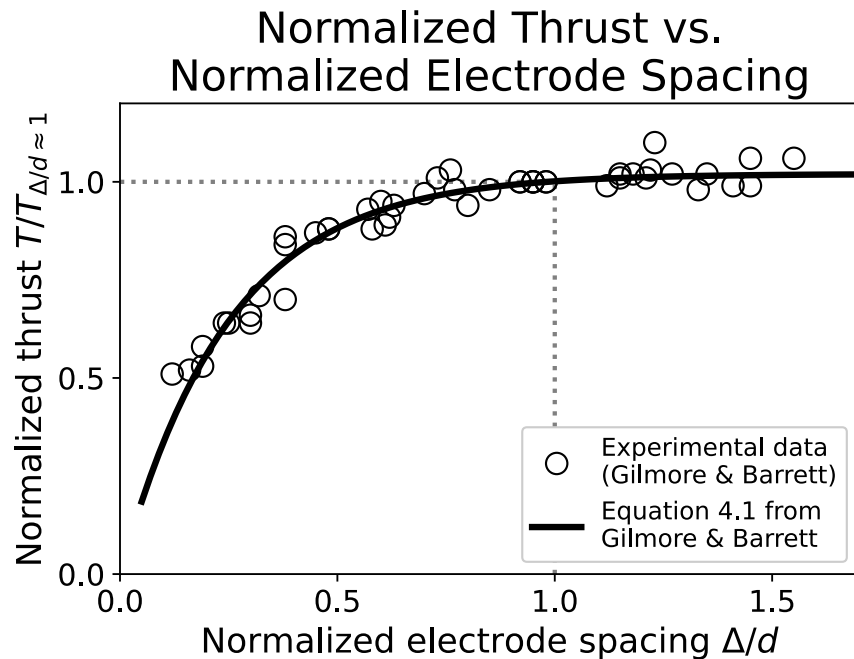


Figure 7: Normalized thrust vs. normalized electrode spacing for arrays of exposed wire-to-cylinder EAD thrusters. Experimental data is obtained from Gilmore & Barrett [9].

Figure 7 shows that thrust declines rapidly for $\frac{\Delta}{d} \lesssim 1$. The experimental data was gathered for gap spacings ranging from 30-80 mm; the decline in thrust appears regardless of gap spacing. Gilmore & Barrett attribute this decline to electric-field interference. More specifically, an investigation of EAD systems with multiple emitters by Lemetayer et al. [59] shows that this decline may be caused by the emitters' electric fields affecting corona inception. Therefore, if gap spacing is increased, electrode vertical spacing must also increase in order to maintain a constant $\frac{\Delta}{d}$, resulting in a larger thruster array with correspondingly higher mass and drag.

Non-ideal effects: Leakage current and reverse emission are two non-ideal effects that are not included in the idealized model in Section 2.2.2. Leakage current is current that flows from the emitter to the surroundings instead of to the collector[§]. Reverse emission (also called counter-ionic wind) refers to ions which are generated at the collector, and flow backwards to the emitter. Both effects become more significant at higher gap spacings and voltages; they both reduce thrust and/or increase electrical power draw.

Xu et al. [18] conducted experiments with wire-to-cylinder EAD thrusters. They showed that reverse emission can be mitigated by increasing the collector (cylinder) diameter, improving thruster performance. For similar reasons, larger collector airfoils or collector airfoils with larger leading-edge radii should help mitigate reverse emission. Reverse emission can also be mitigated by increasing collector span relative to the emitter, or by adding end caps to the collector [21]. Leakage current and reverse emission are discussed further in Refs. [18], [21].

[§] Leakage current is encountered during indoor experiments where current can flow to the building walls. It may also be an issue during takeoff, when current can flow to the ground. However, leakage current is not expected to be an issue in flight, because the aircraft is well away from walls or other surroundings to which current can flow.

Voltage limits: A practical upper limit on voltage is set by spark breakdown (arcing)^{**}, which limited the thruster experiments in Ref. [9] to voltages below 39 kV. The V2 thruster voltage was limited to 40 kV for similar reasons. In addition, higher thruster voltages mean that a power converter with a higher output voltage is required. Since power-converter mass is a function of its output voltage (among other variables), a power converter with a higher output voltage should be heavier [10], [11]. Power converters are discussed in more detail in Section 2.5.

2.3 Ducted EAD thrusters

2.3.1 Overview

A ducted EAD thruster consists of one or more EAD electrode pairs, enclosed in a duct. If more than one stage of electrodes is used, the thruster is called a multistaged ducted (MSD) thruster. The results in Section 2.3.3 show that MSD thrusters are both more powerful and more efficient than their exposed counterparts. This is in part because the duct contributes to thrust, as is the case in ducted fans [23]. Other hypothesized advantages of MSD thrusters include:

- The duct can support the electrodes, so they can be made smaller, reducing drag losses.
 - By using multiple small stages instead of one large thruster, the power-converter output voltage can be lowered; the power-converter mass can therefore be reduced. This is discussed further in Section 4.3.4.
 - The duct can act as a physical barrier between the electrodes and the surroundings. This may result in increased safety, since humans are thus less likely to accidentally receive electrical shocks from the electrodes.
 - The duct can further reduce noise by serving as an acoustic liner^{††}, as with jet engines [60].
-

^{**} The onset of spark breakdown is to first order related to an upper limit on average electric field strength (i.e., to $\frac{V}{d}$), rather than to an upper limit on voltage. Ref. [22] quotes an average electric field strength of 10^6 V/m, above which spark breakdown is encountered. The spark breakdown voltage should therefore increase with gap spacing.

^{††} However, the dominant mechanism by which EAD thrusters produce noise (i.e., the mechanism that must be shielded by an acoustic liner) is not yet known. Potential mechanisms are discussed in Section 6.5.

A full patent application for MSD thrusters has been filed by the author and collaborators [61].

A diagram of an MSD thruster is shown in Figure 8. It consists of an inlet, a duct with constant cross-sectional area that contains multiple stages of EAD electrodes, and a nozzle. A single MSD thruster stage is shown in Figure 9. It consists of an emitter and a collector electrode, separated by a gap spacing, with an applied DC voltage.

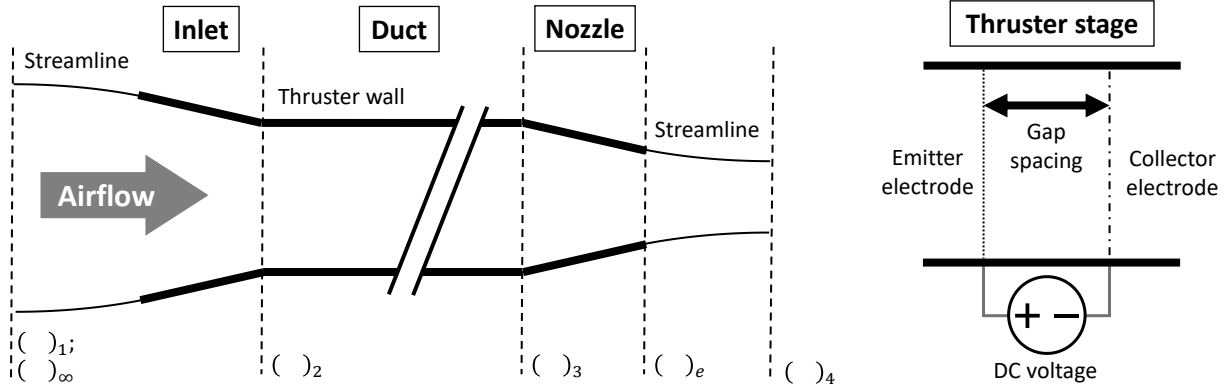


Figure 8: Side-view diagram of an MSD thruster, showing the inlet, duct, and nozzle.

Figure 9: Diagram of one MSD thruster stage.

The vertical dotted lines in Figure 8 are stations that are used by the one-dimensional thruster model in the next section. The stations are denoted as follows:

- $(\)_1, (\)_\infty$: the freestream; i.e., far upstream from the thruster.
- $(\)_2$: the thruster duct entrance.
- $(\)_3$: the thruster duct exit.
- $(\)_e$: the thruster nozzle exit.
- $(\)_4$: far downstream from the thruster.

Figure 9 does not show the thruster electrode geometry, because the modeling approach taken in the next section is agnostic to electrode geometry. Electrode geometry is discussed in more detail in Section 4.3.3.2.

2.3.2 Equations

The MSD thruster designs presented in this thesis (Chapters 4 and 5) are modeled by extending the MSD thruster model from Gomez-Vega et al. [23] to account for drag losses from the inside of the duct walls. The equations used are repeated here for convenience.

Modeling approximations are as follows. The flow is assumed to be steady-state, incompressible, and quasi-one-dimensional (1D). The thruster is decoupled; its ion source produces sufficient ions such that the current is limited by space charge. Geometry and performance of the inlet, as well as interference between electrodes, is neglected. The duct area is constant between stations 2 and 3, and the duct exit pressure is atmospheric. Finally, the stage pressure rise and losses are independent of the number of stages (i.e., identical for each stage).

Under these conditions, simple momentum theory can be used to predict the overall thruster behavior. The equations used are Equations 2–4, 9, and 41 from Ref. [23], repeated here as

$$v_2 = v_3 = \frac{A_e}{A_2} v_4 = \phi v_4 \quad (10)$$

$$v_4 = \sqrt{v_\infty^2 + 2 \frac{\Delta P}{\rho}} \quad (11)$$

$$\frac{T}{A_2} = \rho v_4 (v_4 - v_\infty) \phi - \frac{D_{\text{wall}}}{A_2} \quad (12)$$

$$(\Delta P)_{\text{loss}} = \frac{1}{2} \rho v_2^2 K_L \quad (13)$$

$$\Delta P = n[(\Delta P)_{\text{EAD}} - (\Delta P)_{\text{loss}}] \quad (14)$$

where $v_1 = v_\infty$ is the freestream velocity, $v_2 = v_3$ is the thruster bulk velocity, $v_4 = v_e$ is the exit velocity, $\phi = \frac{A_e}{A_2}$ is the exit area ratio (exit cross-sectional area / duct cross-sectional area), ΔP is the duct pressure rise between stations 2 and 3, ρ is the air density, $\frac{T}{A_2}$ is the thrust density, $(\Delta P)_{\text{loss}}$ is the stage pressure loss, K_L is the stage loss coefficient, n is the number of thruster stages, and $(\Delta P)_{\text{EAD}}$ is the stage pressure rise due to EAD. Equation (12) is an extension of Equation 4 from Ref. [23]: inner wall drag D_{wall} is added, to account for losses due to friction from the inside of the duct walls.

The stage pressure rise due to EAD is obtained using Equations 12, 21, and 22 from Ref. [23], repeated here as

$$\overline{(\Delta P)_{\text{EAD}}} \equiv \frac{\mu(\Delta P)_{\text{EAD}}}{j_{\text{MG}} d} \quad (15)$$

$$\bar{v}_2 \equiv \frac{v_2 d}{\mu V} \quad (16)$$

$$j_{MG} = \frac{9}{8} \epsilon \mu \frac{V^2}{d^3} \quad (17)$$

$$\overline{(\Delta P)_{EAD}} = (1 + \bar{v}_2) \left(1 - \frac{\bar{v}_2}{3} \right) \quad (18)$$

where $\overline{(\Delta P)_{EAD}}$ is the nondimensional stage pressure rise due to EAD, μ is the ion mobility, d is the thruster stage gap spacing (distance between emitter and collector electrodes), \bar{v}_2 is the nondimensional thruster bulk velocity, V is the stage applied DC voltage, j_{MG} is the Mott-Gurney current density, and ϵ is the electric permittivity.

Next, the current density is obtained using Equations 15-16 from Ref. [23], repeated here as

$$\bar{j} \equiv \frac{j}{j_{MG}} \quad (19)$$

$$\bar{j} = (1 + \bar{v}_2)^2 \quad (20)$$

where \bar{j} is the nondimensional current density, and j is the current density.

Duct inner wall losses are estimated using an equivalent skin-friction method, given here as

$$Re_{wall} = \frac{v_2 l_{thruster}}{\nu} \quad (21)$$

$$C_f = \frac{0.074}{Re_{wall}^{0.2}} \quad (22)$$

$$D_{wall} = \frac{1}{2} \rho v_2^2 S_{wall} C_f Q_{wall} \quad (23)$$

where Re_{wall} is the wall Reynolds number, $l_{thruster}$ is the thruster nacelle length, ν is the kinematic viscosity, C_f is the skin-friction coefficient, S_{wall} is the wall inner surface area, and $Q_{wall} > 1$ is an empirical factor that accounts for boundary-layer interference at the duct corners [62]. Equation (22) is the skin-friction coefficient of a turbulent flat plate, as given by Hoburg & Abbeel [63].

Finally, the power density (electrical power from the power converter / duct cross-sectional area) is obtained using

$$\frac{P}{A_2} = \left(\frac{P}{A_2}\right)_{\text{ion}} + \left(\frac{P}{A_2}\right)_{\text{accel}} \quad (24)$$

$$\left(\frac{P}{A_2}\right)_{\text{ion}} = \frac{n j E_{\text{ion}}}{e} \quad (25)$$

$$\left(\frac{P}{A_2}\right)_{\text{accel}} = n j V \quad (26)$$

where $\frac{P}{A_2}$ is the electrical power density, the subscripts $(\)_{\text{ion}}$ and $(\)_{\text{accel}}$ refer to ion generation and ion acceleration respectively, E_{ion} is the amount of energy required to generate one ion, and e is the elementary charge.

The model in this section assumes decoupled thrusters, but it can be adapted to model MSD corona thrusters, as detailed in Ref. [23]. This version of the model was experimentally validated for MSD corona thrusters with up to 10 stages by Nicolas Gomez Vega. Details of the experiments are provided in Chapter 5 of his PhD thesis [64].

2.3.3 Discussion

In this section, a simple model for comparison between exposed and ducted thrusters is derived. In order to do so, an equivalent array of exposed EAD thrusters is defined, and is shown in Figure 10. An MSD thruster with the same electrode array dimensions is shown in Figure 11. These two systems have identical dimensions (except for the duct), so they can be directly compared.

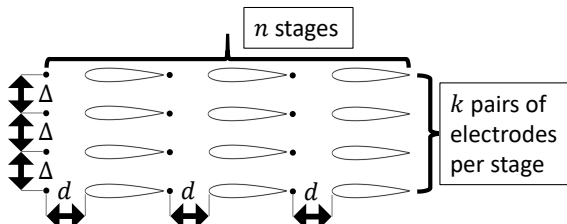


Figure 10: An array of exposed EAD thruster electrode stages.

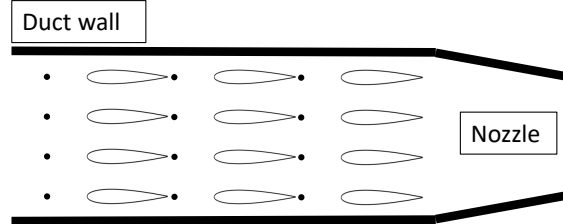


Figure 11: An MSD thruster with identical electrode array dimensions.

The model for exposed EAD thrusters in Section 2.2.2 yields current, thrust, and power estimates per unit thruster span, while the model for ducted EAD thrusters in Section 2.3.2 yields current, thrust, and power estimates per unit thruster cross-sectional area. In order to compare the two, the spacing Δ between electrode pairs in the same thruster stage is defined. For the purpose of this

section, it is assumed that $\Delta = d$ to avoid electrode interference (see the discussion on electrode array size in Section 2.2.3). Both thruster models (exposed and ducted) are further simplified by neglecting ionization power; i.e., $E_{\text{ion}} = 0$.

Further approximations, required to simplify the MSD thruster model, are as follows. Static conditions (zero freestream velocity) are assumed, and the current and duct pressure rise are unaffected by thruster bulk velocity (i.e., $\overline{(\Delta P)_{\text{EAD}}} = \bar{j} = 1$). Electrode and wall drag losses are neglected (i.e., $K_L = D_{\text{wall}} = 0$), and a constant-area nozzle is used (i.e., $\phi = 1$).

Under these circumstances, the exposed- and ducted-thruster current models simplify to

$$j_{\text{unducted}} = \frac{I}{bk\Delta} = \frac{2}{\pi} \varepsilon \mu \frac{V^2}{d^3} \quad (27)$$

$$j_{\text{ducted}} = \frac{9}{8} \varepsilon \mu \frac{V^2}{d^3} \quad (28)$$

Equation (28) is the Mott-Gurney law, and is identical to Equation (17). Thrust and thrust-to-power for both systems then simplify to

$$\left(\frac{T}{A}\right)_{\text{unducted}} = \frac{T}{bk\Delta} = n \frac{2}{\pi} \varepsilon \left(\frac{V}{d}\right)^2 \quad (29)$$

$$\left(\frac{T}{A}\right)_{\text{ducted}} = n \frac{9}{4} \varepsilon \left(\frac{V}{d}\right)^2 \quad (30)$$

$$\left(\frac{T}{P}\right)_{\text{unducted}} = \frac{1}{\mu V} \frac{d}{d} \quad (31)$$

$$\left(\frac{T}{P}\right)_{\text{ducted}} = \frac{2}{\mu V} \frac{d}{d} \quad (32)$$

respectively. Finally, the ducted and unducted results are directly compared at the same gap spacing and voltage to obtain

$$\left(\frac{T}{A}\right)_{\text{ducted}} = \frac{9\pi}{8} \left(\frac{T}{A}\right)_{\text{unducted}} \cong 3.5 \left(\frac{T}{A}\right)_{\text{unducted}} \quad (33)$$

$$\left(\frac{T}{P}\right)_{\text{ducted}} = 2 \left(\frac{T}{P}\right)_{\text{unducted}} \quad (34)$$

Equations (33) and (34) show that for a fixed thruster gap spacing and voltage, a ducted thruster produces approximately 3.5 times as much thrust as an equivalent unducted thruster; the thrust-to-

power is doubled. This is the main advantage of ducting for EAD thrusters: the duct contributes to thrust, resulting in an increase in both thrust and efficiency.

A similar modeling approach can be applied to ducted propellers. Under a similar set of approximations, a ducted propeller produces twice as much thrust at the same power as an equivalent unducted propeller. Therefore, the equivalent of Equations (33) and (34) for ducted propellers would both include a factor of 2. A factor of 3.5 is instead encountered in Equation (33) for the EAD thrust density, because the ducted and unducted systems use different current laws. The unducted system current is modeled via the Geurst law: Equation (2). The equivalent ducted system current is modeled via the Mott-Gurney law: Equation (17).

The simplified comparison in Equations (33) and (34) contains two important limitations:

- **The duct mass and drag is not included.** Historically, this is the main reason why ducted fans are not used by most propeller-driven aircraft: the additional mass and drag of a duct offsets its increased thrust and efficiency [62].
- **Freestream velocity effects are not included.** The thrust and efficiency benefits of a duct decrease with freestream velocity. Ducts are therefore at their most beneficial, relative to unducted systems, at zero forward speed [62]. The effects of forward speed on MSD thruster performance are analyzed in Ref. [23], and are shown in Figure 4 of that reference.

Both of these effects are included in the design optimization of aircraft powered by MSD thrusters, presented in Chapters 4 and 5.

The thrust benefit of an MSD thruster, relative to an exposed thruster, can also be demonstrated experimentally, as follows. Equation (3) predicts thrust as a function of current for an exposed EAD thruster. If MSD thrusters are more powerful, the thrust for a given current should be greater than that predicted by Equation (3). Experimental evidence showing that this is indeed the case is provided in Appendix B of Ref. [5]: measured MSD thrust is greater than that predicted by Equation (3). This is because the duct, and not just the electrodes, contributes to thrust.

2.4 Batteries

The V2, as well as the aircraft designed in this thesis, use batteries to store electrical energy to power the thrusters. Batteries are modeled using two sizing parameters [65]:

- **Specific energy:** stored electrical energy per unit battery mass. This parameter is also known as gravimetric energy density.
- **Specific power:** maximum electrical power draw per unit battery mass. This parameter is also known as gravimetric power density.

A distinction is made between cell-level and pack-level parameter values. Cell-level parameters only account for the mass of the battery cells. Pack-level parameter values are lower, because they include the mass of the battery control electronics, packaging, and thermal protection system (or TPS, the system which protects the battery pack from thermal runaway) [66]. A typical amount by which pack-level specific energy of an electric-aircraft battery is reduced, relative to the cell-level value, is 25% [67].

The onboard battery pack on the V2 consisted of 54 lithium-polymer battery cells [13]. Battery-pack sizing parameter values achieved during the V2 test flights can be estimated using the power draw, endurance, and battery mass values given in Table 1. The resulting pack-level specific energy and power are compared with those of existing prototype lithium-ion batteries, obtained from Ref. [68], in Table 3.

Table 3: Pack-level battery sizing parameters for the V2, compared with existing batteries.

	V2	Prototype lithium-ion
Specific energy	67 Wh/kg	200 Wh/kg
Specific power	2.7 kW/kg	2 kW/kg

Table 3 shows that the V2 specific energy is lower than that of existing batteries. However, the V2 specific power is higher. This apparent mass reduction is achieved because the V2 battery pack did not include a thermal protection system. The resulting safety risk may be acceptable for a non-passenger-carrying UAV, intended as a technology demonstrator.

This thesis is focused on the characteristics of the propulsion system unique to EAD-powered aircraft. Therefore, no improvements to battery technology beyond the current state-of-the art are assumed. The exception is in Chapter 4; the vehicles designed in that chapter require an improved battery specific power (see Section 4.3.5). For similar reasons, other issues specific to battery-pack design, such as state-of-charge margins, cell aging, and reserve requirements, are beyond the scope of this thesis. These issues are discussed further in Refs. [67]–[70].

2.5 Power conversion

As mentioned in Section 1.2, a power converter is required to supply high-voltage power to the EAD thrusters. A schematic of the power-electronics system used by the V2 is shown in Figure 12. Note that the power-converter circuit diagram in Figure 12 is taken from Ref. [13].

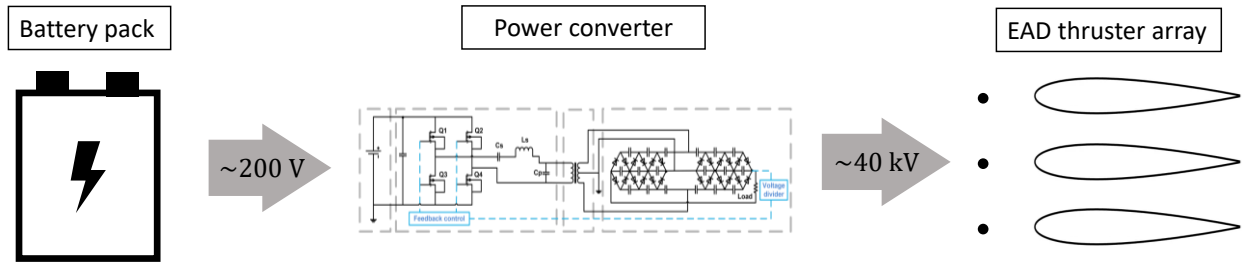


Figure 12: A schematic of the V2 power-conversion system, including the battery, power converter, and EAD thruster array. The power-converter circuit diagram is taken from Ref. [13].

Figure 12 shows that the EAD thruster array on the V2 required an applied voltage of 40 kV. However, the V2 battery pack operated at a nominal voltage of only 200 V, despite the fact that all 54 cells were wired in series [13]. Therefore, a power converter was required, to raise the battery-pack voltage to that required by the thruster array. It consisted of three components:

- **Inverter:** the inverter converts the DC current from the battery to AC current, and applies a voltage gain of approximately 2.5.
- **Transformer:** The transformer isolates the high-voltage portion of the power-electronics system from the low-voltage portion, and increases the voltage by a factor of 15.
- **Rectifier:** the last step is the Cockcroft-Walton rectifier, which converts the AC current back to DC, and includes a voltage gain of 5.6.

Power converters in this thesis are modeled via two sizing parameters: specific power (device output power divided by mass) and efficiency (output power / input power). Parameter values achieved during the V2 test flights can be estimated using the power draw, efficiency, and mass values given in Table 1. Results are given in Table 4. Specific power is estimated using an estimated output power of 527 W, based on the tabulated input power and efficiency.

Table 4: Sizing parameters for the V2 power converter.

Efficiency	85%
Specific power	1.03 kW/kg

The V2 power-converter specific power (1.03 kW/kg) is 5-10 times higher than off-the-shelf solutions that existed at the time it was developed [10], [11]. Despite this, Table 1 shows that it has a mass of 0.51 kg, more than a fifth of the total vehicle mass. Further increases in specific power should benefit the performance of future EAD airplanes.

The functional dependence of power-converter mass can be stated as

$$m_{\text{HVPC}} = f(V_{\text{in}}, V_{\text{out}}, P_{\text{out}}, \dots) \quad (35)$$

i.e., the power-converter mass m_{HVPC} is a function of input voltage V_{in} , output voltage V_{out} , and output power P_{out} , among other variables. Power-converter mass can be reduced by increasing the input voltage, lowering the output voltage, or reducing the output power.

2.6 Chapter conclusions

EAD propulsion systems are characterized in this chapter. Firstly, simplified models for exposed corona and decoupled thrusters are developed in Section 2.2. For a fixed thruster span, greater thruster performance can be obtained at higher gap spacings and voltages; these benefits are predicted theoretically and demonstrated experimentally. However, the achievable benefits are limited by electrode array size, non-ideal effects, and voltage limitations. Next, models for multistaged ducted (MSD) EAD thrusters are developed in Section 2.3. MSD thrusters are more powerful and efficient than exposed thrusters, in part because the duct contributes to thrust. Finally, batteries and power converters are characterized in Sections 2.4 and 2.5 respectively; the battery and power converter on the V2 are compared with the state-of-the-art. This information is used to design EAD-powered airplanes in Chapters 3, 4, and 5.

3 Design of aircraft with exposed EAD thrusters

3.1 Background and overview

This chapter describes the design, construction, and flight testing of a third-generation EAD flight demonstrator aircraft, based on a nominal surveillance mission. This aircraft is hereafter referred to as the Version 3, or V3. The goal is to build and test an aircraft with practical capabilities, defined in Section 1.3 to mean with sufficient payload, range and/or endurance, and flight performance to be of use in some initial application (in this case, for surveillance). If this effort is successful, it would yield an affirmative answer to this thesis' research question: a practical EAD airplane for a surveillance mission can indeed be designed and built.

The V3 was intended to be built and flight tested by a team of engineers, including the author. Therefore, the design philosophy is to use EAD technologies that were available to the team, rather than to assume improvements. For example, the thruster model used to design the V3 (Section 3.2.4) is fully empirical, and is based on thruster experimental data. In addition, the power-converter specific power (Section 3.2.5) is identical to that achieved by the V2. Finally, the battery specific energy (also in Section 3.2.5) is based on cell-level tests conducted by the team, rather than on futuristic battery cells.

The rest of this chapter is structured as follows. Study methods, including mission requirements, architecture enumeration, multidisciplinary design optimization, and thruster, power-electronics, and aircraft models, are given in Section 3.2. Results, including an architecture trade study, an overview of the selected architecture, a description of the construction and flight testing, and a discussion, are given in Section 3.3. Finally, the chapter conclusions are presented in Section 3.4.

The design, construction, and flight testing of the V3 airframe was conducted collaboratively by a team of graduate and undergraduate students. The author was responsible for the conceptual design of the V3, including the multidisciplinary optimization framework described in Section 3.2.3. Much of the description of the signomial programming algorithm in Section 3.2.3 was previously published by the author in Ref. [14]. Design requirements for the V3 were identified by the author, with assistance from Ethan Rolland. Thruster configurations were developed by the author in collaboration with Nicolas Gomez Vega. Nicolas Gomez Vega and Jayaprakash Kambhampaty

conducted the thruster experiments and provided the data used by the author to develop the thruster performance model. Battery specifications are based in part on battery cell tests conducted by Hiromu Rose. The biplane and tandem-wing drag models were developed by the author in collaboration with Umar Padela. The thruster drag model adjustments for wake velocity effects were documented by Gilmore in his PhD thesis [15], and were separately documented in a collaboration between him and the author [14].

The airframe detailed design, construction and flight testing effort was led by Nicholas Perovich, and was previously documented in his Master's thesis [71]. Collaborators included the author, Jamie Abel, Nicolas Gomez Vega, Faith Bulan, Jakob Coray, Sabrina Hare, Jayaprakash Kambhampaty, Jose Lavariega, Alazar Lemma, Gabriella McDonald, Chad Meier, Christopher Vargas, and Sienna Williams. Due to program constraints, a power converter was not available for the V3 flight tests. Instead, the V3 was tested using a substitute (propeller) propulsion system, with the author as the RC pilot. Finally, climb analysis was completed by the author.

3.2 Methods

3.2.1 Mission requirements

The V3 is designed for a surveillance mission, in which the vehicle is required to loiter while gathering information via cameras and other sensors. This class of mission is selected in part because it benefits from low noise: a silent UAV could perform a battlefield surveillance mission without noise giving its position away. A concept of operations is depicted in Figure 13.

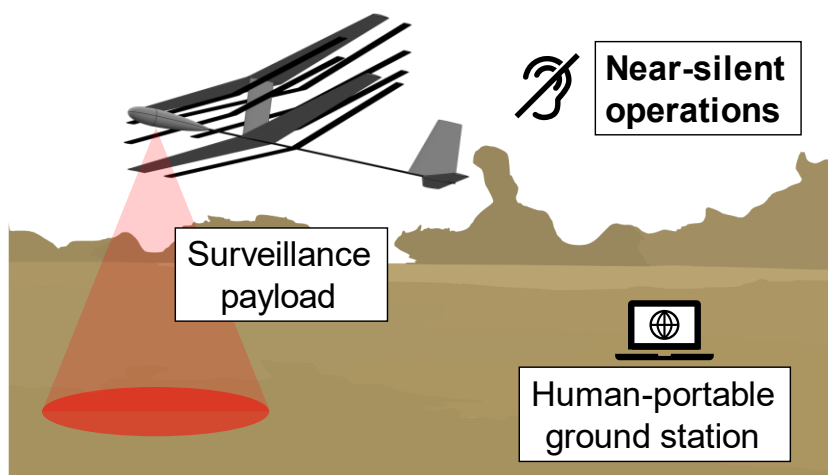


Figure 13: Concept of operations for the V3.

The AeroVironment Raven, a hand-launched propeller-driven electric fixed-wing battery-powered military UAV, serves as an example of a vehicle designed for a surveillance mission [72]. The earlier RQ-11A (introduced in 2006) carries a color or infrared camera. The later RQ-11B (introduced in 2013) carries a more-capable gimbaled payload, including both daylight and thermal cameras in the same unit. The RQ-11B is shown in Figure 14.



Figure 14: An image of the RQ-11B Raven, taken from Ref. [73].

Representative data for the Raven is obtained from Ref. [72], and is provided in Table 5.

Table 5: Specifications for both versions of the Raven.

	RQ-11A	RQ-11B
Service entry year	2006	2013
Vehicle mass	1.9 kg	1.81 kg
Payload mass	200 g	450 g
Wingspan	1.37 m	1.37 m
Endurance	90 min	75 min

Based in part on the data in Table 5, the following requirements are selected for the V3:

- **200 g camera payload.** While not enough to match the RQ-11B, this payload requirement is superior to that of the RQ-11A.

- **30 minutes of endurance.** The Raven is capable of 75-90 minutes of flight, depending on version. However, typical military surveillance missions can be as short as 30 minutes [73].
- **Outdoor flight.** The V2 was designed to fly indoors, but the V3 is designed for outdoor flight. Outdoor flight is implicit in the definition of a practical EAD aircraft, since a surveillance aircraft must fly outdoors to be useful. This imposes additional structural loading requirements. For example, the V2 wing was sized using a limit load factor of 1.05 (greater than 1 to allow for turns [14]). By contrast, Section 3.2.6 shows that the V3 wing is sized using a limit load factor of 2.5, within the range of typical values for general-aviation aircraft [62]. This is more than twice as high as for the V2.
- **Human-portable if possible.** The Raven can be transported in a backpack [72]; a similar capability would be useful for the V3. For this reason, it may be necessary to limit the V3 wingspan, as discussed in Section 3.3.2.

These requirements represent a threshold for practicality, as defined by the research question (Section 1.3). Put differently, if an EAD-powered aircraft can fly outdoors for 30 minutes with a 200 g camera payload, it is of interest for an initial (surveillance) application. It can therefore be considered practical, and would serve as an affirmative answer to the research question.

The mission profile includes four segments: takeoff, cruise, bank, and dash. A runway takeoff is assumed; the rotation speed must be at least 10% greater than the stall speed. All three flight segments (cruise, bank, and dash) must also be flown at a speed at least 10% greater than the stall speed. Requirements specific to each segment are summarized in Table 6.

Table 6: Mission profile, showing the requirements for each mission segment.

Mission segment	Requirements
Takeoff	Ground roll. 80 m runway length.
Cruise	Steady level flight.
Bank	20-degree level bank.
Dash	Steady level flight. Airspeed at least 10% greater than loiter speed.

The takeoff-distance model is taken from Hoburg & Abbeel [63].

3.2.2 Architecture enumeration

Vehicle architecture is defined in this thesis chapter to consist of three components: thruster ion source, surface integration strategy, and aircraft configuration. The V2 prototype utilized a conventional architecture (a monoplane with fully-exposed corona thrusters) to reduce program risk [13], [14]. However, performance gains may be obtained by utilizing an unconventional vehicle architecture.

Surface integration strategies and aircraft configurations are enumerated in this section. The two ion sources considered for the V3 (DC corona and DBD) are described in Section 2.2.1.

3.2.2.1 Surface-integrated thrusters

The V2 thruster array was responsible for approximately 42% of total vehicle drag [14]. 29% of this drag came from the emitter wires; the remaining 71% came from the collector airfoils. In theory, much of this drag can be eliminated by integrating the thrusters into the skin of the aircraft. This technique is hereafter referred to as surface integration.

As a first step towards a fully-integrated thruster, various “semi-integrated” thruster designs (in which only part of the thruster is integrated) are proposed. They are depicted in Figure 15, Figure 16, and Figure 17.

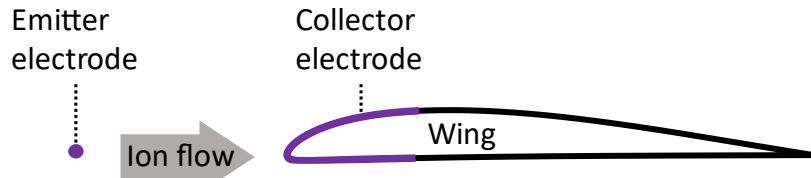


Figure 15: A leading-edge thruster.

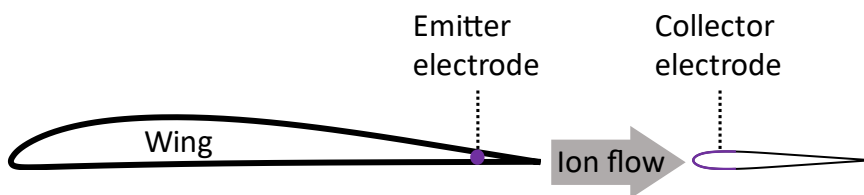


Figure 16: A trailing-edge thruster.

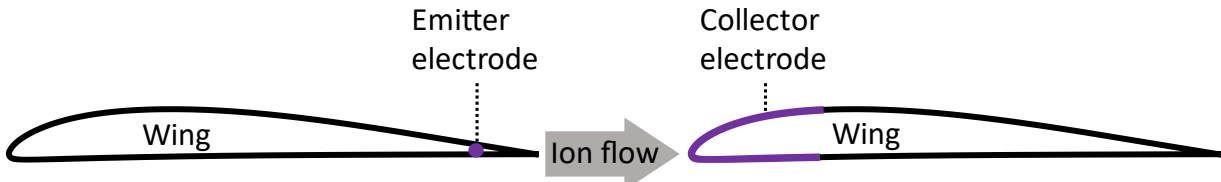


Figure 17: A tandem thruster.

In Figure 15, the thruster is integrated into the leading edge of the wing. Since the wing also provides lift, the drag from a separate collector airfoil is eliminated. However, wake velocity losses (discussed in Appendix E) are more significant for a leading-edge thruster than for a fully-exposed thruster, because the wing is much larger than a separate collector.

The design depicted in Figure 16 gets around this problem by instead integrating the thruster into the wing trailing edge. This type of thruster does not have an exposed emitter wire. The smaller collector reduces wake velocity losses, so this type of thruster may yield improved performance relative to the leading-edge thruster.

A tandem thruster is depicted in Figure 17. The thruster is sandwiched between two wings; the resulting aircraft must have a tandem wing. Both the exposed emitter wire and separate collector airfoil are eliminated. However, as with the leading-edge thruster, collector wake velocity losses are an issue.

All three semi-integrated thrusters pose a control issue. Because they are integrated into the wing, they are located in close proximity to the ailerons. Therefore, they may cause electromagnetic interference (EMI) with the aileron servos. This problem is potentially worse for DBD thrusters relative to DC corona thrusters, because DBD thrusters use AC voltages. The simplest way of mitigating this issue is to eliminate ailerons, and rely on dihedral and yaw-roll coupling for control. The V2 and V3 both use this approach; it is discussed further in Appendix K.

An EAD aircraft can employ several types of thrusters simultaneously. The term *surface integration strategy* refers to the types and placements of the various surface-integrated thrusters on an aircraft.

3.2.2.2 Multistaging

In theory, more than one type of semi-integrated thruster can be used on the same wing; this technique is called multistaging. For example, a wing can have both a leading-edge thruster and a trailing-edge thruster. Additional performance gains can be obtained, because both an exposed collector and an exposed emitter are eliminated. However, a counter-ionic wind can be generated, which reduces performance. This issue is shown in Figure 18.

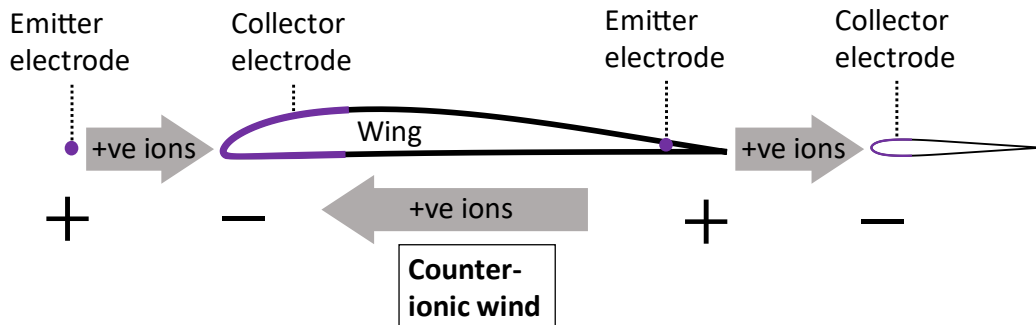


Figure 18: Multistaging, without alternating polarity.

Figure 18 shows a wing with leading-edge and trailing-edge thrusters, both of which generate positively-charged ions. Most of these ions flow from their emitter to their respective collector, creating an ionic wind and generating thrust. However, due to the polarity, some of the positively-charged ions produced at the trailing-edge emitter instead flow backward, to the negatively-charged leading-edge collector. These ions form a counter-ionic wind, reducing thrust.

This problem can be solved by alternating the polarity of successive stages, as shown in Figure 19.

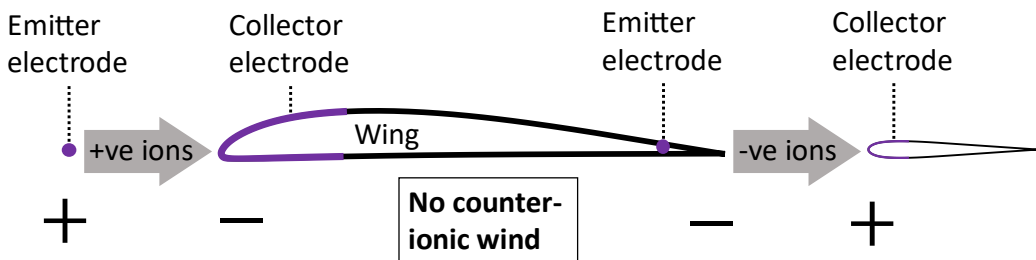


Figure 19: Multistaging, with alternating polarity.

Figure 19 shows that the trailing-edge thruster now has a negatively-charged emitter, which generates negative ions. These ions will not flow backwards to a negatively-charged electrode, and so the counter-ionic wind is eliminated. A similar approach was used by Sato et al. [34] for a flow control application, and for pumping applications by Rickard et al. [74] and by Qiu et al. [75].

A full patent application for surface-integrated EAD thrusters has been filed by the author and collaborators [76].

3.2.2.3 Aircraft configurations

Surface-integrated thrusters add new degrees of freedom to the aircraft design space. Synergies with nonplanar aircraft configurations may also exist. Figure 20, Figure 21, and Figure 22 show some of the configurational options available.

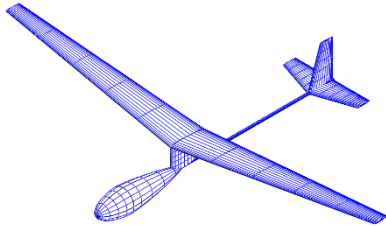


Figure 20: A monoplane configuration.

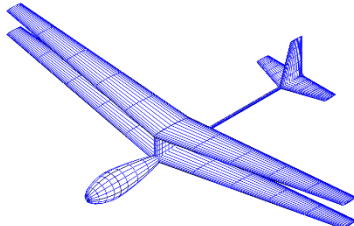


Figure 21: A biplane configuration.

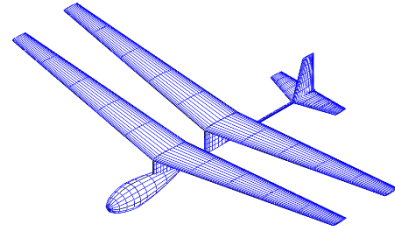


Figure 22: A tandem wing configuration.

The simplest option (Figure 20) is a monoplane. Fully exposed EAD thrusters can be added to this aircraft without any surface integration, as with the V2. Thrusters can also be integrated into the wing leading edge and/or trailing edge, as in Figure 15 and Figure 16 respectively.

Thrusters integrated into the wing leading or trailing edges reduce drag by eliminating exposed collectors or emitters respectively. The greater the wingspan, the greater the benefit. However, wings with greater spans are heavier. For this reason, nonplanar configurations (i.e., with more than one wing) are considered. Examples include the biplane and the tandem wing, shown in Figure 21 and Figure 22 respectively.

The hypothesized benefits of a nonplanar configuration can be summarized as follows. For the same total wing area and lift, a nonplanar configuration has a lower wing root bending moment, relative to a planar configuration. This reduces structural mass [77]. The total wingspan (sum of the span of the two wings) can therefore be made greater than that of an equivalent planar configuration with the same wing mass. In the case of an EAD aircraft, this allows for additional span available for integrated thrusters, yielding further benefits. Also, as discussed in Section 3.2.2.1, tandem wings may further reduce drag if a tandem thruster is installed between the wings.

The primary disadvantage of nonplanar configurations is aerodynamic interference between the two wings, which increases induced drag [77]. Models for this phenomenon for biplanes and tandem wings are given in Appendix B. In addition, nonplanar wings have a smaller chord for the same total wing area. This has two potentially negative consequences. Firstly, the smaller chord means that the local Reynolds number is lower, resulting in greater profile drag at the same flight speed and total lift. The smaller chord also leads to a smaller airfoil leading-edge radius, potentially resulting in reverse emission (see the discussion on non-ideal effects in Section 2.2.3). A trade study between vehicle architectures must take these factors into account.

3.2.2.4 Putting it all together: vehicle architectural options

A vehicle architecture consists of an ion source, a surface integration strategy, and an aircraft configuration. Architecture options are given in Table 7. Any option could use DC corona or DBD ion sources.

Table 7: V3 architectural options.

Architecture	Thruster type(s)
Monoplane (exposed thrusters)	Fully exposed
Monoplane (leading-edge thrusters)	Fully exposed Leading-edge
Monoplane (trailing-edge thrusters)	Fully exposed Trailing-edge
Monoplane (leading- and trailing-edge thrusters)	Fully exposed Leading-edge Trailing-edge
Biplane (leading-edge thrusters)	Fully exposed Leading-edge
Biplane (trailing-edge thrusters)	Fully exposed Trailing-edge
Biplane (leading- and trailing-edge thrusters)	Fully exposed Leading-edge Trailing-edge
Tandem (leading-edge thrusters)	Fully exposed Leading-edge
Tandem (trailing-edge thrusters)	Fully exposed Trailing-edge
Tandem (tandem thrusters)	Fully exposed Leading-edge Tandem Trailing-edge

Note from Table 7 that all architectures with integrated thrusters also have exposed thrusters. Design optimization studies reveal that while semi-integrated thrusters reduce drag, they do not provide enough thrust for flight on their own. Therefore, exposed thrusters are still required.

3.2.3 Multidisciplinary design optimization

The aircraft in this thesis are designed using a multidisciplinary optimization (MDO) framework, developed by the author. The framework uses signomial programming (SP), an efficient optimization algorithm. A signomial program requires that the objective function and constraints be posed in terms of monomial, posynomial, and signomial functions. Any monomial function $m(\mathbf{x})$, any posynomial function $p(\mathbf{x})$, and any signomial function $s(\mathbf{x})$ can be written [78] as

$$m(\mathbf{x}) = c \prod_j x_j^{a_{ij}} \quad (36)$$

$$p(\mathbf{x}) = \sum_i c_i \prod_j x_j^{a_{ij}} \quad (37)$$

$$s(\mathbf{x}) = \sum_i c_i \prod_j x_j^{a_{ij}} \quad (38)$$

where elements x_j of the vector of design variables \mathbf{x} must all be positive, while exponents a_j and a_{ij} can be any real number. Note that both a posynomial and a signomial can be written simply as a sum of monomial terms. Signomials differ from posynomials in that negative leading coefficients c_i are allowed. Monomial and posynomial leading coefficients c and c_i must be positive.

In a signomial program, the objective function must be a ratio of posynomials. Meanwhile, the constraints must be a combination of signomial inequality constraints, posynomial inequality constraints, and/or monomial equality constraints. This form can be summarized as

$$\begin{aligned} & \text{Minimize } \frac{p_0(\mathbf{x})}{q_0(\mathbf{x})} \\ & \text{subject to } s_i(\mathbf{x}) \leq 0, i = 1 \dots n_s \\ & \quad p_i(\mathbf{x}) \leq 1, i = 1 \dots n_p \\ & \quad m_i(\mathbf{x}) = 1, i = 1 \dots n_m \end{aligned} \quad (39)$$

where $p_0(\mathbf{x})$ and $q_0(\mathbf{x})$ are posynomial functions. n_s , n_p , and n_m are the number of signomial, posynomial, and monomial constraints in the optimization problem respectively.

Signomial programs are faster and more robust than general nonlinear optimization algorithms [78]. However, the form of Equation (39) means that black-box models cannot be directly used. Instead, fits to data from black-box models can be used, as long as the fits are written as monomial, posynomial, or signomial functions. For example, airfoil drag can be estimated using a posynomial fit to airfoil data obtained from an external solver, as in Appendix D.

The signomial programs in this thesis are developed using the open-source Python package GPkit [79], with MOSEK as the numerical solver. Posynomial fits are generated using GPfit [80], another open-source Python package. Signomial programming (as well as geometric programming [63], a simplification without signomial constraints) has been applied to the design and optimization of high-altitude communications and surveillance aircraft, urban air taxis, short-takeoff-and-landing (STOL) aircraft, airliners, and electric propulsion systems [81]–[88].

The problem formulation for the signomial programs in this thesis is summarized in Table 8.

Table 8: Problem formulation for a signomial program.

Minimize	Objective function
With respect to	Free variables: <ul style="list-style-type: none"> Traditional optimization variables (wingspan, wing spar dimensions, fuselage length, etc.) Analysis outputs (vehicle mass, thrust, drag, power, etc.)
Subject to	Constraints: <ul style="list-style-type: none"> Model equations Constraint equations Fixed parameters

Most optimization techniques distinguish between two types of equation:

- *Models.* $q = \frac{1}{2} \rho v_\infty^2$ is an example model equation, describing dynamic pressure q in terms of air density ρ and freestream velocity v_∞ . Another model required by most aircraft design optimization problems is a mass summation: $m_{\text{aircraft}} = \sum m_i$, where m_{aircraft} is the total mass of the aircraft and m_i is the mass of the i^{th} aircraft component.
- *Constraints.* A maximum-lift condition $C_L \leq C_{L_{\max}}$ is an example constraint; lift coefficient C_L is a design variable.

This distinction between models and constraints does not exist for a signomial program. Instead, in accordance with the form of a signomial program in Equation (39), all models must be written as constraints. This results in over 2,500 constraints for the V3 optimization problem. Similarly, signomial programs do not distinguish between an *optimization variable* in the traditional sense (such as wingspan or fuselage length) and an *analysis output* (such as vehicle mass, thrust, or drag). Both are treated as variables by the optimizer, resulting in over a thousand free variables. For comparison, most low-cost aircraft design optimization frameworks (without geometric or signomial programming) draw a distinction between models and constraints, as well as between variables and outputs [89]–[91]. The resulting optimization problems may use on the order of a few dozen constraints and about as many variables.

Cruise-segment endurance (maximize) is used as the objective function for the V3. Optimization data, including number of free variables, constraints, and typical optimization solve times, is provided in Table 9 for the selected V3 architecture (described in Section 3.3.3).

Table 9: Number of free variables, number of constraints, and typical solve times on a laptop computer for design optimization of the selected V3 architecture.

Free variables	1306
Constraints	2537
Typical solve time	0.8 s

3.2.4 Thruster models

The model for exposed thrusters in Section 2.2.2 cannot be directly be applied to design optimization, because it cannot account for the non-ideal effects discussed in Section 2.2.3. Instead, an empirical approach, based on experimental thruster data, is applied.

Wire-to-airfoil thrusters are used. Data is gathered for corona and DBD thrusters, with one and with two stages, and with positive and negative polarity. Gap spacing is varied from 90-150 mm; collector chords are varied from 50-330 mm. Applied DC voltage is limited to 60 kV because of sparking concerns and power-converter limitations (see Section 2.2.3). The effect of freestream velocity is not included, as all experimental data is gathered at static conditions. The experimental setup is summarized in Refs. [17]–[19].

Models for the various thrusters are generated, based on posynomial fits [80] to the experimental data. Collector chord and thrust are treated as independent variables; power, voltage, and maximum thrust are the dependent variables. Once the optimizer selects a vehicle design point, gap spacing is inferred by comparing the design point with the experimental data. This approach means that the model consisted entirely of posynomial equations. Had voltage been an independent variable and thrust a dependent variable, the model would have required signomial inequality constraints, which are less numerically efficient [85].

The optimization model for single-stage thrusters is then of the form

$$\frac{P}{b} = f\left(c, \frac{T}{b}\right) \quad (40)$$

$$V = f\left(c, \frac{T}{b}\right) \quad (41)$$

$$T_{\max} = f(c) \quad (42)$$

where c is the collector chord and T_{\max} is the maximum thrust. The equivalent model for two-stage thrusters is of the form

$$\frac{P}{b} = f\left(c_1, c_2, \frac{T}{b}\right) \quad (43)$$

$$V = f\left(c_1, c_2, \frac{T}{b}\right) \quad (44)$$

$$T_{\max} = f(c_1, c_2) \quad (45)$$

where c_1 and c_2 are the chords of the 1st and 2nd collector respectively.

Fits are compared with experimental data in Appendix A. RMS errors at the experimental points used to generate the fits are below 4% for all fits.

3.2.5 Power-electronics models

The power-electronics system consists of the battery and the power converter. Sizing parameters for both components are given in Table 10.

Table 10: Power-electronics sizing parameters.

Parameter		Value
Battery	Specific energy	115 $\frac{\text{Wh}}{\text{kg}}$
	Specific power	2 $\frac{\text{kW}}{\text{kg}}$
	Density	2.4 $\frac{\text{kg}}{\text{L}}$
Power converter	Maximum input power	515 W
	Specific power	1.03 $\frac{\text{kW}}{\text{kg}}$
	Efficiency	85%

The battery is sized using a fixed specific energy, specific power, and density. The specific energy (115 Wh/kg) is obtained from battery cell tests; it is about twice as high as the value achieved on the V2 (Table 3). The specific power (2 kW/kg) is lower than that achieved on the V2. Both values are consistent with pack-level numbers for existing prototype lithium-ion batteries (Table 3).

The power converter is sized using a fixed specific power of 1.03 kW/kg and an efficiency of 85%. Both values are consistent with those of the V2 power converter, given in Table 4. However, its output voltage is 60 kV, higher than the V2 output voltage of 40 kV. This change improves thruster performance (see Section 2.2.3). The power-converter maximum input power (i.e., battery output power) is limited to 515 W, in order to reduce program risk by fixing the power-converter design. A similar constraint was added late in the V2 design process for similar reasons [14].

3.2.6 Aircraft mass, drag, and structural models

This section gives details of the mass, drag, and structural models used to design the V3. Aircraft-level sizing parameters are given in Table 11. An overview of the models for each aircraft component are given in the text; further details are provided in Table 12, Table 13, and Table 14.

Table 11: Aircraft-level sizing parameters for vehicles with exposed thrusters.

Parameter	Value
Aircraft mass margin	10%
Aircraft drag margin	10%
Oswald efficiency	0.85

3.2.6.1 Mass models

As with the V2 [14], the V3 is constructed primarily from carbon fiber, Kevlar, balsa wood, and foam, typical for model aircraft and small ultralight UAVs. Kevlar is chosen instead of carbon fiber for many key components (such as the fuselage pod and tail boom). This is because Kevlar is a more effective insulator than carbon fiber, and is therefore better suited for components near the thrusters, power converter, and wiring that connects them.

The mass model is based on a bottom-up component summation approach. It can be written as

$$m_{\text{total}} = (1 + \text{margin}) \sum_i m_i \quad (46)$$

where m_{total} is the vehicle total mass and m_i is the mass of the i^{th} aircraft component. The aircraft-level mass margin (in addition to component-level mass margins) is 10%, as listed in Table 11.

Mass models for most aircraft components are based on component dimensions, material densities, and component-specific mass margins. For example, the tail boom is a hollow Kevlar cylindrical tube. Its mass is estimated using

$$\text{Vol}_{\text{boom}} = 2\pi r_{\text{boom}} t_{\text{boom}} l_{\text{boom}} \quad (47)$$

$$m_{\text{boom}} = (1 + \text{margin}) \rho_{\text{Kevlar}} \text{Vol}_{\text{boom}} \quad (48)$$

where Vol_{boom} is the tail-boom material volume, r_{boom} is the boom radius, t_{boom} is the boom wall thickness, l_{boom} is the tail-boom length, m_{boom} is the tail-boom mass, ρ_{Kevlar} is the density of Kevlar, and margin is set to 10%. Equation (47) is derived using a thin-wall approximation; i.e., $r_{\text{boom}} \gg t_{\text{boom}}$. A minimum boom wall thickness constraint of 1.5 mm is imposed, to prevent buckling and to ensure that a boom with the optimized dimensions is available commercially.

The remaining components' mass models are mostly developed similarly. Mass model assumptions are documented in Table 12.

Table 12: Mass models for vehicles with exposed thrusters.

Component	Mass model
Fuselage pod	Scaled using the mass, surface area, and volume of the V2 fuselage pod.
Tail boom	Hollow Kevlar cylindrical tube, with a minimum wall thickness of 1.5 mm. 10% mass margin.
Monoplane wing	Spar: carbon-fiber spar caps; end-grain balsa spar core. Minimum cap thickness of 0.01 mm. 20% mass margin. Wing: spar; Foamular 250 (pink foam) leading-edge D-box; carbon-fiber trailing edge; Microlite covering. 25% mass margin.
Wing pylon(s)	High Load 60 (blue foam) core; Kevlar skin (2 plies). 15% thickness-to-chord ratio. No mass margin.
Biplane wing	2 monoplane wings. 20% mass margin.
Tandem wing	2 monoplane wings. 10% mass margin.
Horizontal tail	Foamular 250 (pink foam) airfoil with 12% thickness-to-chord. 10% mass margin.
Vertical tail	Foamular 250 (pink foam) airfoil with 12% thickness-to-chord. 10% mass margin.
DC corona thruster emitter	36 AWG copper wire; diameter of 0.127 mm.
DBD thruster emitter	36 AWG copper wire; diameter of 0.127 mm. Surrounded by a FEP dielectric; diameter of 0.78 mm.
Exposed thruster collector	Foamular 250 (pink foam) airfoil with 50 mm chord; 10% thickness-to-chord. Aluminum-foil electrode covering 30% of the airfoil chord.
Leading-edge thruster collector	Aluminum-foil electrode covering 30% of the airfoil chord.
Trailing-edge thruster collector	Inherited from exposed thruster collector.
Thrusters	Inherited from emitter and collector mass models. 30% mass margin.
Landing gear	1% of aircraft unmargined mass.
Battery	Fixed specific energy, power, and volume (see Section 3.2.5).
Power converter	Fixed specific power (see Section 3.2.5).
Payload	Fixed mass and volume (see Section 3.2.1).
Miscellaneous	100 g. Accounts for the RC receiver and servos.

3.2.6.2 Structural models

The wing and tail boom have structural models. They are sized using engineering beam theory, subject to bending, shear, and tip-deflection constraints and factors of safety.

The monoplane wing spar consists of carbon-fiber spar caps and an end-grain balsa core; it is sized using the model in Appendix C. The biplane and tandem wings inherit from the monoplane model,

with each wing carrying 50% of the lift. The tail boom is also sized using beam theory. Further details of the structural models are provided in Table 13.

Table 13: Structural models for vehicles with exposed thrusters.

Component	Structural model
Tail boom	Cantilever load from a quadratic sum of horizontal- and vertical-tail maximum lift, with a maximum lift coefficient of 0.9. Bending, shear, and tip-deflection (max 5% of boom length) constraints. Factor of safety of 2.
Monoplane wing	Loads from a symmetric pull-up at 10% greater than cruising speed, with a load factor of 2.5. Constant beam curvature [92]. Bending, shear, and tip-deflection (max 5% of wingspan) constraints. Factor of safety of 1.5.
Biplane wing	Inherited from monoplane wing, with the upper and lower wings each carrying 50% of the lift.
Tandem wing	Inherited from monoplane wing, with the front and back wings each carrying 50% of the lift.

3.2.6.3 Drag models

Like the mass model, the drag model is based on a bottom-up component summation. It can be written as

$$C_D = (1 + \text{margin}) \left[C_{D_{\text{induced}}} + \sum_i (C_{D_{\text{profile}}})_i \right] \quad (49)$$

where C_D is the vehicle total drag coefficient, $C_{D_{\text{induced}}}$ is the induced drag coefficient (drag due to lift), and $(C_{D_{\text{profile}}})_i$ is the profile drag of the i^{th} aircraft component. The drag margin is set to 10%, as listed in Table 11.

Profile drag models are defined separately for each aircraft component. The profile drag coefficients of components with airfoil cross-sections (the wing, pylon, tail, and thruster collectors) are estimated as

$$(C_{D_{\text{profile}}})_i = \frac{(C_{d_{\text{airfoil}}})_i (S_{\text{planform}})_i (Q)_i}{S} \quad (50)$$

where $C_{d_{\text{airfoil}}}$ is the 2D airfoil drag coefficient, S_{planform} is the component planform area, Q is an empirical factor that accounts for interference between components, and S is the reference area (wing planform area). The subscript $(\)_i$ refers to the i^{th} component. Airfoil drag coefficients are estimated using fits to profile drag data from Xfoil [93]. The wing airfoil drag model is documented in Appendix D; models for pylon, horizontal tail, vertical tail, and thruster collectors are prepared similarly.

For components other than airfoils (such as the fuselage pod and tail boom), profile drag is estimated using an equivalent flat-plate approach, as described by Raymer [62]. This approach can be summarized as

$$\left(C_{D_{\text{profile}}} \right)_i = \frac{(C_f)_i (\text{FF})_i (\text{SA})_i (Q)_i}{S} \quad (51)$$

where C_f is the equivalent flat-plate skin-friction coefficient, FF is the form factor, and SA is the component wetted surface area. The skin-friction coefficient of components with laminar and/or turbulent flow is estimated using

$$(C_f)_{\text{laminar}} = \frac{1.328}{\sqrt{\text{Re}}} \quad (52)$$

$$(C_f)_{\text{turbulent}} = \frac{0.074}{\text{Re}^{0.2}} \quad (53)$$

respectively, where the Reynolds number Re is estimated using the component length (ex. fuselage-pod length or tail-boom length). Equation (52) is the well-known Blasius solution for a flat plate, while Equation (53) is identical to Equation (22). A weighted average of Equations (52) and (53) is used for components with some laminar flow, but that transition to turbulence.

The thruster emitter wires are cylindrical; their drag is estimated using the cylinder drag model in Appendix F. Thruster drag models (both emitters and collectors) include an adjustment for the local flow velocity increase due to ionic wind, as described in Appendix E.

Induced drag (drag due to lift) is estimated using a span-efficiency model. For monoplanes, induced drag is estimated as

$$(C_D)_{\text{induced}} = \frac{C_L^2}{\pi e_{\text{Oswald}} \text{AR}} \quad (54)$$

where $(C_D)_{\text{induced}}$ is the induced drag coefficient, C_L is the lift coefficient, e_{Oswald} is the Oswald efficiency, and AR is the wing aspect ratio (based on the planar wingspan and total wing area).

Equation (54) is not directly applicable to the biplane and tandem wing configurations, because of interference between the two wings (see Section 3.2.2.3). Aerodynamic interference effects are included via the model in Appendix B.

Further details of the profile drag models are provided in Table 14.

Table 14: Profile drag models for vehicles with exposed thrusters.

Component	Profile drag model
Fuselage pod	Equivalent turbulent flat-plate drag with a form-factor adjustment [62]. 20% interference factor.
Tail boom	Equivalent turbulent flat-plate drag. No interference factor.
Monoplane wing	Fit to NACA 44XX airfoil data: $C_d = f\left(\frac{t}{c}, \text{Re}, C_L\right)$. Fit RMS error: 1.0%. 20% interference factor.
Wing pylon(s)	Fit to NACA 00XX airfoil data: $C_d = f\left(\frac{t}{c}, \text{Re}\right)$. Fit RMS error: 5.0%. 20% interference factor.
Biplane wing	Inherited from monoplane wing. 20% interference factor.
Tandem wing	Inherited from monoplane wing. 20% interference factor.
Horizontal tail	Fit to HT14 airfoil data: $C_d = f\left(\frac{t}{c}, \text{Re}\right)$. Fit RMS error: 2.3%. 10% interference factor.
Vertical tail	Fit to HT14 airfoil data: $C_d = f\left(\frac{t}{c}, \text{Re}\right)$. Fit RMS error: 2.3%. 10% interference factor.
DC corona thruster emitter	Cylinder drag model (Appendix F). Only included if emitter is exposed.
DBD thruster emitter	Cylinder drag model (see Appendix F), using the dielectric wire diameter. Only included if emitter is exposed.
Exposed thruster collector	Fit to HT14 airfoil data: $C_d = f\left(\frac{t}{c}, \text{Re}\right)$. Fit RMS error: 1.2%.
Trailing-edge thruster collector	Inherited from exposed thruster collector.
Thrusters	Inherited from emitter and collector drag models. Wake velocity effects included (Appendix E). 20% interference factor.
Landing gear	10% of aircraft unmargined profile drag.

3.2.7 Dimensional models

3.2.7.1 Fuselage pod

The purpose of the fuselage pod is to hold the battery, payload, and power converter. The fuselage pod is shaped like an ellipsoid. The usable fuselage-pod volume is estimated using

$$\text{Vol}_{\text{pod}} = \frac{4}{3}\pi l_{\text{pod}} w_{\text{pod}} h_{\text{pod}} \quad (55)$$

$$(\text{Vol}_{\text{pod}})_{\text{usable}} = 0.5 \text{ Vol}_{\text{pod}} \quad (56)$$

where l , w , and h refer to length, width, and height respectively, while Vol is volume. The subscripts $(\)_{\text{pod}}$ and $(\)_{\text{usable}}$ refers to the fuselage pod and usable volume respectively; the factor of 0.5 is a margin.

The payload and battery have volume models. The payload is sized using an estimated volume of 2000 cm^3 ; the battery volume is modeled via its density (see Table 10). The constraint

$$(\text{Vol}_{\text{pod}})_{\text{usable}} \geq \text{Vol}_{\text{payload}} + \text{Vol}_{\text{battery}} \quad (57)$$

is then used to ensure that both components fit in the fuselage. Finally, the power-converter lacks a volume model. The factor of 0.5 in Equation (56) serves as a margin, to ensure that the power converter fits in the fuselage pod as well.

3.2.7.2 Tail boom

A side view of the biplane, showing the tail-boom dimensions, is shown in Figure 23.

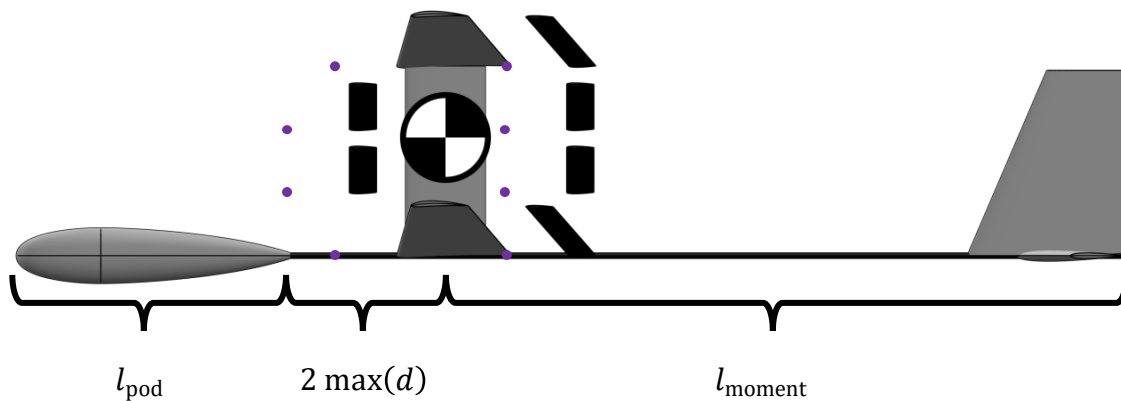


Figure 23: Side view of the V3 biplane, showing the tail-boom dimensions.

Figure 23 shows that the tail boom is equal to the sum of three lengths:

- **Fuselage-pod length** l_{pod} . The tail boom extends all the way through the fuselage pod.
- **An offset of twice the thruster gap spacing** $2 \max(d)$. This offset is intended to keep the fuselage pod away from the thrusters, whose high voltages could otherwise cause electromagnetic interference with the electronics in the pod.
- **Tail moment length** l_{moment} . This is the length between the center of gravity (CG) and the tail, and is used for tail sizing (see Section 3.2.7.6). The CG is located in the middle of the pylon; this assumption is verified in Appendix K.

Figure 23 applies to the biplane, but the monoplane and tandem wing are designed similarly.

3.2.7.3 Wing

The wing taper ratio is set to 0.5. A value of 0.45 gives a near-elliptical lift distribution [62]; a slightly higher taper ratio is used for the V3 to help mitigate tip stall. In addition, wing twist is not required, simplifying construction. A lower limit on wing thickness-to-chord ratio of 9% is imposed, as maximum-lift performance tends to degrade for lower thickness-to-chord ratios.

The wing sizing parameters are given in Table 15.

Table 15: Wing sizing parameters for vehicles with exposed thrusters.

Parameter	Value
Wing taper ratio	0.5
Wing minimum thickness-to-chord ratio	9%
Wing maximum lift coefficient	1.15

3.2.7.4 Thrusters

As with the V2, the V3 thrusters have limited structural reinforcement, and are connected to the wings via struts (see Ref. [71] for details). Strut mass and drag is included via the thruster- and aircraft-level margins, but their presence means that limitations on thruster length, relative to planar wingspan (equal to the span of one wing for the nonplanar configurations), are required. Therefore, exposed thrusters have their span limited to 90% of the planar wingspan. If the thruster is integrated into the leading or trailing edge of a wing, its span is limited to 98% of the wingspan. Tandem thrusters are also limited to 98% of the span.

The number of thruster stages n is set to 2 (one positive and one negative stage), while the number of electrode pairs per stage k is a design variable. These parameters are defined in Figure 6. Signomial programs do not directly allow for integer design variables, so the nearest integer to the optimized solution is selected during post-processing. The optimization is then repeated with the integer value to obtain the selected architecture specifications in Section 3.3.3.

The height of any pair of thruster electrodes is estimated using

$$h_{\text{thruster}} = 1.5d \quad (58)$$

i.e., 1.5 times the thruster gap spacing. This height is required to estimate the pylon height.

3.2.7.5 Pylon

The pylon minimum height is set by one of three constraints:

- The pylon must be at least as tall as the fuselage-pod radius.
- The pylon must be tall enough for the exposed thruster array to fit between the wing (or the upper wing, if the vehicle is a biplane) and the tail boom.
- If the aircraft is a biplane, the pylon height is equal to the spacing between the two wings.

These constraints can be stated mathematically as

$$h_{\text{pylon}} \geq r_{\text{pod}} \quad (59)$$

$$h_{\text{pylon}} \geq \overline{h}_{\text{pylon}}(k - 1)h_{\text{thruster}} \quad (60)$$

$$h_{\text{pylon}} = (h_{\text{wings}})_{\text{biplane}} \quad (61)$$

respectively, where h is height, r is radius, and k is the number of electrode pairs stacked vertically per stage of exposed thrusters (defined in Figure 6). $\overline{h}_{\text{pylon}} = 1.1$ is a margin, while the subscripts $()_{\text{thruster}}$ and $()_{\text{wings}}$ refer to the exposed thrusters and biplane wings respectively. The factor of $k - 1$ in Equation (59) is included to allow for 1 row of exposed-thruster electrode pairs to be placed above the wing, reducing the required pylon height.

The pylon chord is set to 70% of the wing root chord.

3.2.7.6 Tail

Minimum tail sizes for static stability are defined using tail volume coefficients [62] as

$$C_{HT} \leq \frac{l_{HT}S_{HT}}{b_W S_W} \quad (62)$$

$$C_{VT} \leq \frac{l_{VT}S_{VT}}{\bar{c}S_W} \quad (63)$$

where C is the tail volume coefficient, l is the tail moment arm, S is the planform area, b_W is the wingspan, and \bar{c} is the wing mean aerodynamic chord. The subscripts $(\)_W$, $(\)_{HT}$, and $(\)_{VT}$ refer to the wing, horizontal tail, and vertical tail respectively.

Tail volume coefficients are provided in Table 16. They are consistent with RC aircraft design guidelines, as given by Drela [94]. The tail surfaces lack structural models, so their aspect ratios are fixed. Aspect ratios are also provided in Table 16.

Table 16: Tail volume coefficients and aspect ratios for vehicles with exposed thrusters.

Component	Volume coefficient	Aspect ratio
Horizontal tail	0.5	3.0
Vertical tail	0.025	1.5

When Equations (62)-(63) are applied to the biplane, b_W refers to the planar wingspan (span of 1 wing), \bar{c} refers to the mean aerodynamic chord of one wing (not both), and S_W refers to the total wing area (sum for both wings). A similar convention is used for the tandem wing, except that \bar{c} refers to the sum of the mean aerodynamic chords of both wings (i.e., twice the usual definition).

3.3 Results

3.3.1 Design optimization results

A summary of the optimization results is provided in Table 17. LE, TE, and LE/TE refer to aircraft with wing leading-edge thrusters, trailing-edge thrusters, and leading- and trailing-edge thrusters respectively, as defined in Table 7. Drag coefficients are given in counts: drag coefficient multiplied by 10^4 ; i.e., 1019 counts implies a drag coefficient of 0.1019. Overall efficiency is defined as the product of thrust and flight speed, divided by battery power draw.

Table 17: Summary of the design optimization results for aircraft with exposed thrusters.

	Monoplane; LE corona	Monoplane; LE/TE corona	Monoplane; LE/TE DBD	Biplane; LE/TE corona	Tandem; LE/TE corona	Units
Length	3.40	3.35	2.91	2.68	3.08	m
Planar wingspan	9.56	9.16	7.00	5.56	6.42	m
Planar aspect ratio	35.4	33.5	26.8	31.8	37.3	-
Planar wing area	2.578	2.503	1.826	0.972	1.103	m^2
Total wing area	2.578	2.503	1.826	1.943	2.207	m^2
Exposed thruster stages	2.0	2.0	2.0	2.0	2.0	-
Electrode pairs / stage	1.2	1.0	1.0	1.4	1.0	-
Takeoff mass	6.32	6.37	3.76	4.17	4.51	kg
Payload mass	0.20	0.20	0.20	0.20	0.20	kg
Battery mass	2.26	2.35	0.92	1.20	1.33	kg
HVPC mass	0.42	0.42	0.42	0.42	0.42	kg
Empty mass fraction	0.54	0.53	0.59	0.56	0.57	-
Loiter speed	6.43	6.55	5.89	6.01	5.87	m/s
Loiter lift coefficient	0.95	0.95	0.95	0.95	0.95	-
Loiter drag coefficient	558.7	595.8	763.8	981.3	924.3	counts
Loiter lift-to-drag	17.0	16.0	12.4	9.7	10.3	-
Loiter thrust	3.65	3.92	2.96	4.22	4.31	N
Loiter power draw	413.2	424.3	464.7	481.9	481.5	W
Loiter overall efficiency	5.7%	6.0%	3.8%	5.3%	5.3%	-
Endurance	37.4	37.9	13.4	17.0	18.8	minutes
Max thrust	4.09	4.36	3.13	4.37	4.47	N
Max power draw	515.0	515.0	515.0	515.0	515.0	W

Table 17 lists only five architectures, out of the ten architectures listed in Table 7. These are the only architectures for which converged solutions are obtained; the other architectures did not converge. The tandem wing with tandem thrusters is not investigated, because experimental data for three-stage thrusters was not available at the time of the study.

Recall from Section 3.2.5 that the battery output power is limited to below 515 W, in order to freeze the power-converter design. Table 17 shows that all five converged architectures have a maximum electrical power equal to this limit. Therefore, vehicle endurance cannot be increased simply by increasing battery mass: doing so would add vehicle mass, which would in turn increase drag, thus requiring more electrical power than is available.

Out of the five converged architectures in Table 17, only one (a monoplane with leading- and trailing-edge thrusters) is powered by DBD thrusters. This architecture has the lowest endurance (13.4 minutes), because the DBD thrusters tested are less powerful and less efficient than the corona thrusters (Appendix A). This architecture is therefore eliminated from consideration. The two remaining monoplanes (both powered by corona thrusters) have endurances of 37-38 minutes. The only biplane and tandem wing to converge (also both powered by corona thrusters) can loiter for 17 and 19 minutes respectively.

A mass breakdown is shown in Figure 24.

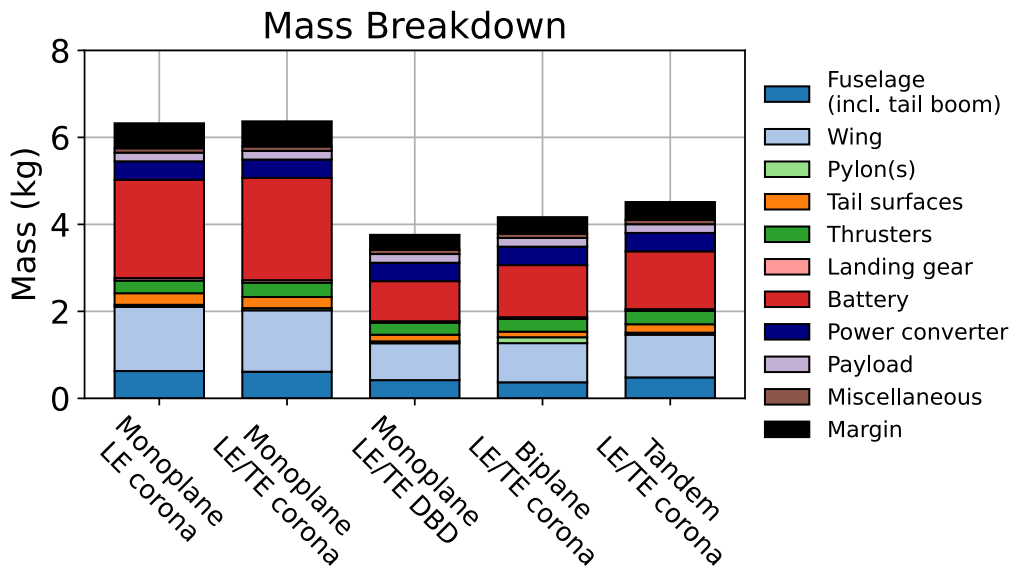


Figure 24: Mass breakdown for aircraft with exposed thrusters.

Figure 24 shows that the battery constitutes the largest share of the mass. For example, the battery accounts for 37% of the total mass of the monoplane with leading- and trailing-edge thrusters. The fuselage, wing, and power converter also account for large portions of the mass of all five vehicles.

A drag breakdown is shown in Figure 25.

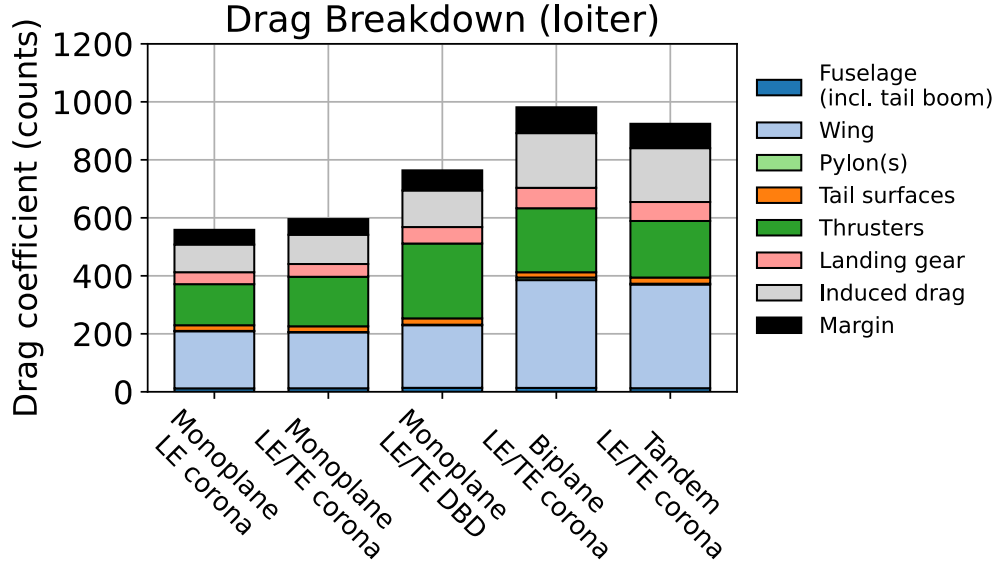


Figure 25: Drag breakdown for aircraft with exposed thrusters.

Figure 25 shows that most of the drag is profile drag from the wing and thrusters, as well as induced drag. However, the drag contribution from the thrusters as a portion of the total has been reduced (relative to the V2), due to surface integration. Recall from Section 3.2.2.1 that the V2 thruster array was responsible for approximately 42% of total vehicle drag. By contrast, the thrusters on the monoplane with leading- and trailing-edge corona thrusters contribute only 29% of the overall vehicle drag. This is also reflected in the lift-to-drag ratio: Table 17 shows that the same monoplane has a loiter lift-to-drag of 16.0, about twice the value achieved by the V2 [14].

3.3.2 Architecture selection

It would seem as if the monoplane with leading- and trailing-edge corona thrusters is the best architectural option, since it has the highest endurance (37.9 minutes). However, Table 17 also shows that this architecture has a wingspan of 9.2 m, a large value that would make it difficult to build and transport. Recall from Section 3.2.1 that portability is listed as one of the V3 requirements. It is therefore desirable to investigate architectures with reduced wingspans.

The sensitivity of loiter endurance to an upper limit on planar wingspan is computed using the optimizer, and is shown in Figure 26. As before, the upper limit on battery output power (515 W) is still imposed.

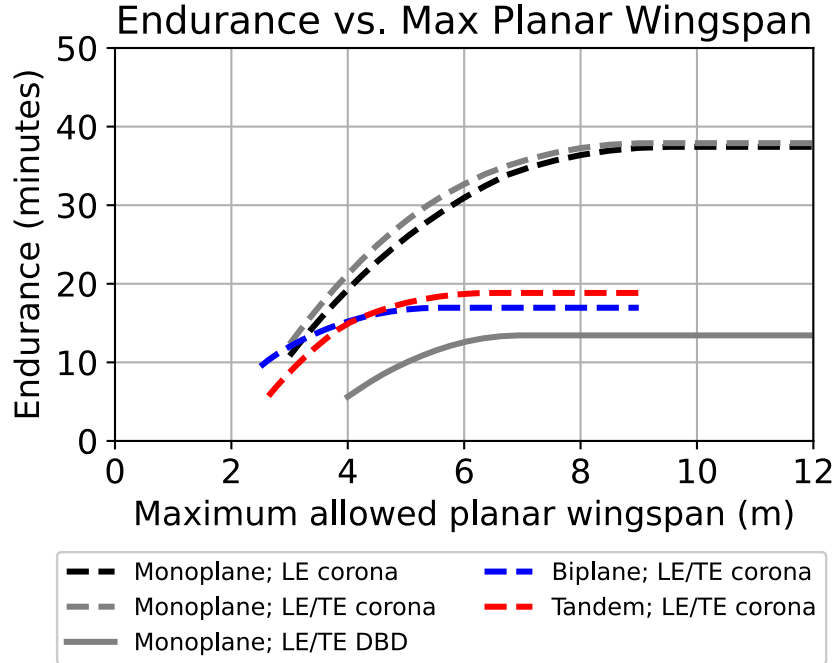


Figure 26: Loiter endurance vs. maximum planar wingspan, for vehicles with exposed thrusters.

The lower extent of the data in Figure 26 is set by optimizer convergence. For example, the monoplane with leading- and trailing-edge DBD thrusters does not converge for planar wingspans below approximately 4 m, indicating that a feasible solution below this wingspan does not exist.

Figure 26 shows that the monoplanes are more sensitive to planar wingspan than the nonplanar vehicles. For example, both monoplanes with corona thrusters have their endurance reduced from almost 40 minutes to below 15 minutes if the wingspan is reduced to 3 m; neither architecture converges at all for lower wingspans. By contrast, the biplane without a wingspan constraint has an endurance of 17 minutes (less than half that of the monoplanes), but an endurance of just under 15 minutes (comparable to the monoplanes) if the wingspan is restricted. Nonplanar architectures can therefore be seen to suffer smaller performance declines, relative to those of monoplane architectures, if the planar wingspan is restricted.

3.3.3 Selected architecture overview

After some iteration, the following design decisions are made for the V3:

- **The wingspan is limited to 3.5 m.** While the exact value is somewhat arbitrary, this limit is intended in part to ensure that the V3 is portable. For comparison, the Raven has a wingspan of 1.37 m (Table 5). The 3.5 m limit is close to the 3 m limit on thruster electrode length imposed during the V2 design process, to make both fabrication and transport easier [14]. Figure 26 shows that due to this limit, the 30-minute endurance requirement in Section 3.2.1 can no longer be met.
- **A biplane architecture with leading- and trailing-edge corona thrusters is selected.** Its endurance is comparable to that of the monoplanes with the above wingspan limit. It has the additional advantage that over-the-wing thrusters are not required. Instead, the exposed-thruster array fits between the two wings, making for an electrically simple design.

As mentioned in Section 3.2.7.4, k (the number of vertically-stacked exposed electrode pairs per stage) is approximated as a continuous design variable. However, an integer value is required to build the V3. Therefore, k is set to 2, the nearest integer value to that produced by the optimizer without such a constraint. The optimization is then repeated to produce the design in this section.

A side view of the V3, showing the resulting thruster array design, is shown in Figure 27. Additional sketches of the V3 are provided in Appendix G.

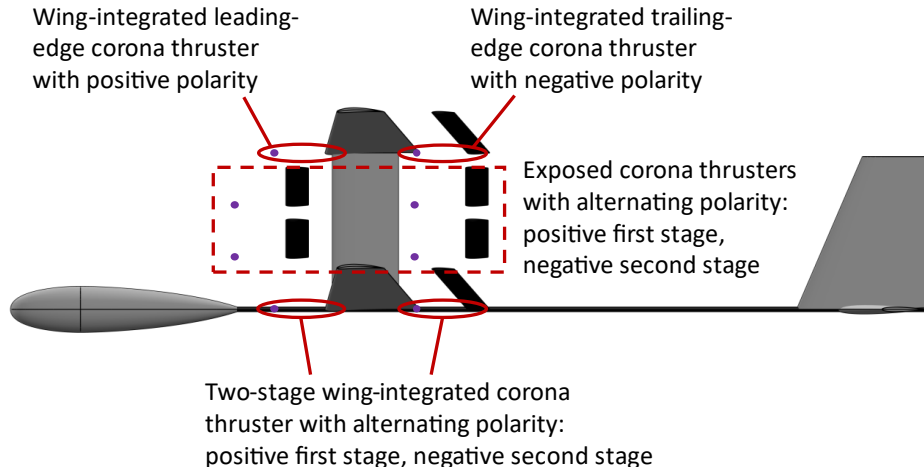


Figure 27: Side view of the V3, showing the thruster array design.

A summary of design optimization data for the V3 is given in Table 18. Data from the V2, obtained from Refs. [13], [14], is also shown for comparison. Detailed dimensional data, a mass breakdown, and detailed performance data are given in Appendix H, Appendix I, and Appendix J respectively.

Table 18: An overview of design optimization data from the V3, compared with the V2.

	V2	V3
Length	2.0 m	2.0 m
Wingspan	5.1 m	3.5 m
Thruster gap spacing	50 mm	106 - 117 mm
Takeoff mass	2.45 kg	3.04 kg
Payload mass	-	0.20 kg
Battery mass	0.23 kg	0.96 kg
HVPC mass	0.51 kg	0.42 kg
Flight speed	4.8 m/s	6.8 - 7.5 m/s
Lift-to-drag ratio	8.0	8.2
Thrust	3.2 N	3.6 - 3.8 N
Thruster max voltage	40.3 kV	60 kV
Electrical power draw	620 W	477 - 515 W
Overall efficiency	2.5%	5.0 - 5.5%
Endurance	90 s	13.8 min

Table 18 shows a range for V3 thruster gap spacing, because different thrusters on the aircraft have different gap spacings. Gap spacings for the V3 thrusters are summarized in Table 19. A range is also provided in Table 18 for thrust and electrical power, because these values vary depending on the mission segment. This can also be seen from the performance data in Appendix J.

Table 19: V3 thruster gap spacings.

Thruster	Gap spacing
Single-stage fully-exposed thruster	105.6 mm
First stage of the two-stage semi-integrated thruster	105.6 mm
Second stage of the two-stage semi-integrated thruster	116.7 mm

Table 18 shows that the V3 is predicted to fly for almost ten times longer than the V2: 13.8 minutes vs. 90 s. This order-of-magnitude improvement can be attributed to the following design differences:

- **Batteries with greater specific energy.** As discussed in Section 3.2.5, the battery specific energy used to design the V3 (115 Wh/kg) is about twice as high as that of the V2 batteries (67 Wh/kg).
- **Increased thruster gap spacing and voltage.** The V2 thrusters' gap spacing was 50 mm; they operated at a voltage of just over 40 kV. The corresponding values for the V3 are larger: its thrusters have gap spacings from 106-117 mm, operating at 60 kV. Since larger gap spacings and voltages translate to improved performance (see Section 2.2.3), this accounts for some of the endurance increase.
- **Surface-integrated thrusters.** The V3 has thrusters integrated into the leading and trailing edges of the wings, reducing drag by eliminating exposed components. Partially as a result, the thrusters contribute about 25% of the total V3 drag (0.92 N out of a total of 3.62 N of drag). The equivalent percentage for the V2 is 42%, 17 percentage points higher. Despite this, the lift-to-drag ratios of the V2 and V3 are similar: 8.0 vs. 8.2. This is partly caused by interference drag between the biplane wings, and also because of the wingspan restriction (Section 3.3.2).
- **Additional thruster experimentation.** As mentioned in Section 2.2.3, using larger thruster gap spacings and voltages can worsen two non-ideal effects: leakage current and voltage and reverse emission. Substantial research into the characterization and mitigation of both effects has been completed since the V2 test flights [18], [21], improving thruster performance. Much of this information is incorporated into the thruster experiments that produced the design data for the V3 (Appendix A).

Additional aerodynamic analysis and design, beyond that performed by the optimizer, is required before the V3 airframe could be built and flight tested. Specifically, airfoils for the wing and thrusters are designed, collector incidence angles are selected, and the aircraft is analyzed for static stability and controllability. These analyses are discussed in Appendix K.

3.3.4 Prototyping and flight testing

The V3 prototyping and flight testing efforts are discussed in more detail by Perovich [71]; a summary is provided in this section.

The V3 airframe was built by a team of undergraduate and graduate students, including the author, during Fall 2021 and Spring / Summer 2022. Team members are listed in Section 3.1. Powered and unpowered flight tests were initially conducted indoors, in the Johnson athletic track at MIT. The built prototype is shown in Figure 28.



Figure 28: The as-built V3 prototype, shown in the MIT Johnson track just before indoor flight testing. Left to right: Nicolas Gomez Vega, James (Jamie) Abel, the author, and Nicholas Perovich.

Due to program constraints, a power converter was not available for the V3 flights, so the EAD propulsion system could not be used. Instead, a substitute propulsion system (a propeller) is used

for propulsion^{††}. This propeller is mounted on a pylon above the fuselage pod; it is visible in Figure 28. Thrust calibration testing (conducted under static conditions) reveals that the propeller can supply as much thrust as the EAD system at a throttle setting of 52%.

Later flight tests were conducted outdoors, on MIT's Briggs athletic field. The field did not have a surface suitable for a runway takeoff. Instead, the aircraft is launched using a catapult, with launch energy stored in bungee cables. It is controlled using a radio controller, with the author as the pilot. The launch setup is shown in Figure 29.



Figure 29: The V3 on its launcher, in preparation for a flight test on MIT's Briggs field. Left to right: Christopher Vargas (holding the left wing), the author, and Alazar Lemma (holding the right wing).

Several outdoor flights were made, the longest of which was conducted on June 30, 2022. Data is obtained from video recordings of the flight, as well as from an onboard data acquisition system (documented in more detail in Ref. [71]). This flight lasted approximately 3.5 minutes, covered approximately 1.6 km, and included several circuits around Briggs Field [71]. The author verified

^{††} However, the EAD propulsion system on the V3 was tested under static conditions, using benchtop power supplies.

qualitatively that the V3 is both stable and controllable, indicating that the aerodynamic design (yaw-roll coupling in particular) documented in Appendix K is successful.

However, this flight was conducted without the exposed emitters or collectors. Despite the resulting drag savings, 100% throttle was required for most of the flight. Furthermore, the average measured airspeed during the flight was 10.45 m/s, well above the design maximum of 7.5 m/s. Therefore, the airframe did not perform as efficiently as designed. Three reasons for this are proposed: mass modeling, drag modeling, and climb thrust requirements. The issues with the mass and drag model relate mostly to modeling and documentation, which should be addressable in a redesign; they are discussed in Appendix L. The third issue (climb thrust requirements) is addressed in the next section.

3.3.5 Discussion: climb requirements

Even if the mass and drag models has been accurate, the V3 airframe with an EAD propulsion system likely would not have performed well during flight testing. This is because it lacks sufficient thrust for climb^{§§}, even though it has (from the optimization results) enough thrust for loiter. Climb thrust requirements, and their application to the V3, are discussed in this section.

Three potential climb rate requirements are identified:

- **Downdraft strength:** the V3 must have a climb rate at least as large as atmospheric downdrafts (columns of descending air) encountered during flight, so that a downdraft will not force the aircraft to descend. Two downdraft strengths are identified: calm day (in which the wind is relatively weak, but atmospheric thermals and downdrafts have formed) and calm dawn (around sunrise, when thermals and downdrafts have not yet formed). These requirements may apply to flight testing, when flights in bad weather can be avoided. The Snowbird human-powered ornithopter was only flown near dawn, in part for this reason [95]. However, a more demanding climb requirement must be met for the V3 to be capable of flying in a broader range of conditions, as is necessary for a practical EAD aircraft.

^{§§} A climb segment is not included in the mission profile (Table 6).

- **Service ceiling:** the FAA defines an aircraft's service ceiling as “[the] maximum...altitude where the best rate-of-climb airspeed will produce a 100 feet-per-minute climb at maximum weight while in a clean configuration with maximum continuous power” [96].
- **Part 23 certification:** The FAA used to impose a minimum sea-level climb requirement of 300 feet per minute for airplanes certified under 14 CFR Part 23 [62]. Current certification requirements specify a climb gradient, rather than a climb rate [97]; the old climb rate requirement is used here to allow for easier comparison with the other potential requirements. Note that Part 23 is not directly applicable to the V3, because the V3 is uncrewed and Part 23 only applies to crewed aircraft.

Climb rates for all four potential requirements are given in Table 20. The downdraft strength estimates are obtained via email correspondence [98], while the service-ceiling climb rate (0.51 m/s) and the old Part 23 certification climb rate (1.52 m/s) are converted to metric units.

Table 20: Potential climb-rate requirements.

Requirement	Climb rate
Calm-day downdraft	0.1 m/s
Calm-dawn downdraft	0.3 m/s
Service ceiling	0.51 m/s
Part 23 certification (old)	1.52 m/s

The V3 airframe is then analyzed to determine whether any of these requirements could be met. The equations describing an aircraft in a steady level climb are given as

$$v_v = v_\infty \sin(\gamma) \quad (64)$$

$$T = D + W \sin(\gamma) \quad (65)$$

$$L = W \cos(\gamma) \quad (66)$$

where v_v and v_∞ are the climb rate and freestream velocity respectively, γ is the climb angle, T is thrust, D is drag, W is vehicle weight, and L is lift.

Equations (64)-(66) are used to predict the required climb thrust of the V3 airframe in loiter. For small climb angles (i.e., $\gamma \lesssim 10^\circ$), the $\cos(\gamma)$ term in Equation (66) is approximately unity, so the lift (and, by extension, the induced drag) is the same as in loiter. Required thrust and thrust-to-

weight for the V3 at loiter speed are thus given in Figure 30 and Figure 31 respectively. Loiter and maximum available thrust and thrust-to-weight are also shown.

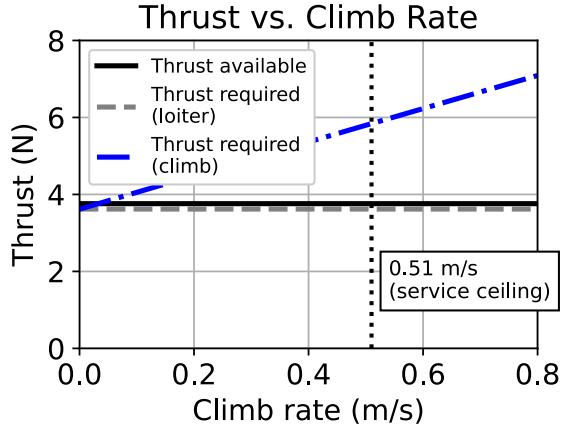


Figure 30: Thrust vs. climb rate for the V3 at loiter speed.

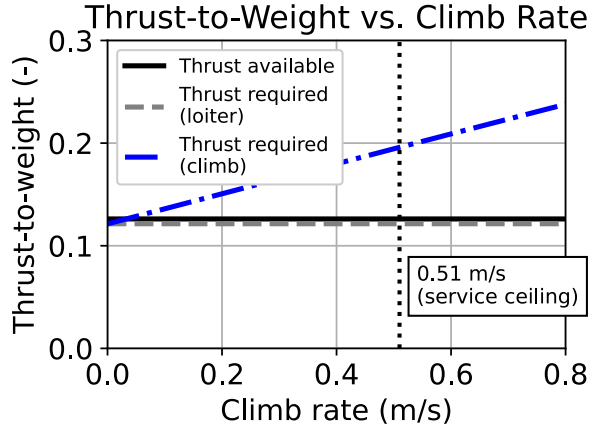


Figure 31: Thrust-to-weight ratio vs. climb rate for the V3 at loiter speed.

Figure 30 and Figure 31 show that thrust increases rapidly with climb rate. Furthermore, the V3 airframe as designed is incapable of meeting the 0.51 m/s service-ceiling requirement. This is because the mission profile (Table 6) does not include a climb segment. Instead, the maximum available thrust (3.76 N) is used during the takeoff ground roll. This is only 4% higher than loiter thrust (3.62 N), and well short of the nearly 6 N required for a service-ceiling climb rate shown in Figure 30. Similarly, the V3 loiter and max thrust-to-weight ratios are 12% and 13% respectively, short of the 20% value required for a service-ceiling climb rate shown in Figure 31. The V3 airframe, as designed, therefore lacks sufficient thrust for climb.

Recall from Table 6 that a climb segment is not included in the V3 mission profile for design optimization. Therefore, in order to assess whether the V3 can be redesigned to meet a climb-rate requirement, a climb segment is added to the mission profile. A sensitivity analysis is then conducted by treating required climb rate as an input parameter, and climb thrust as a constraint. Design optimization results for thrust-to-weight ratio and endurance are shown in Figure 32 and Figure 33 respectively.

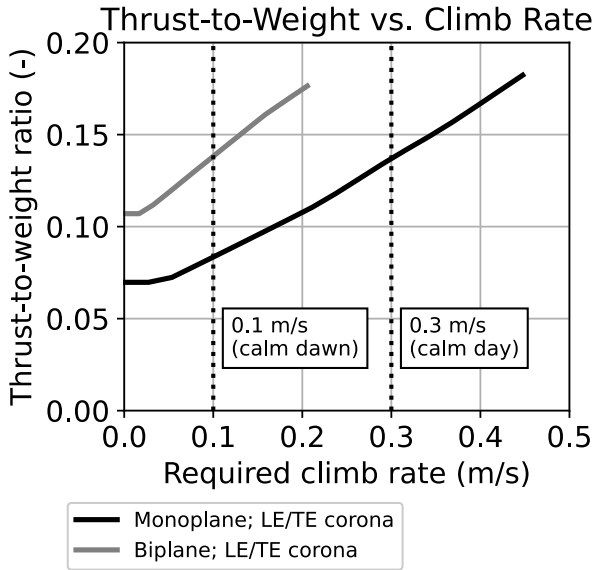


Figure 32: Thrust-to-weight vs. climb rate.

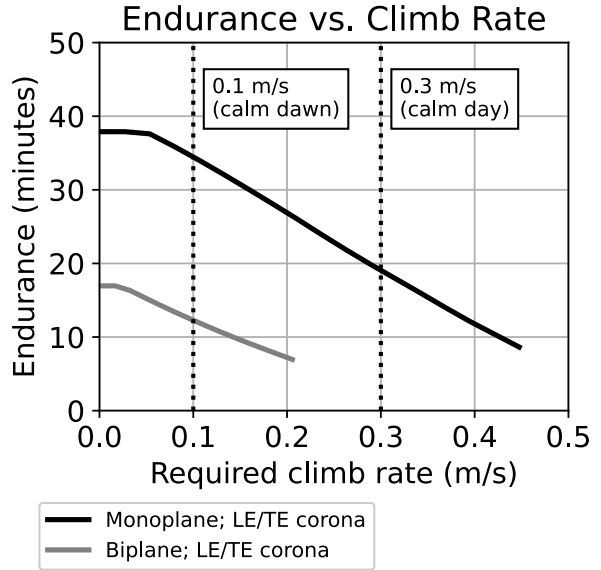


Figure 33: Endurance vs. climb rate.

Figure 32 shows that maximum thrust-to-weight ratio increases with climb rate, while Figure 33 shows that vehicle endurance decreases with climb rate. Beyond a certain climb rate (0.45 m/s and 0.2 m/s for the monoplane and biplane respectively), no further results are obtained. This is because the optimizer does not converge for higher climb rates. Therefore, the monoplane and biplane architectures are not feasible for climb rates above 0.45 m/s and 0.2 m/s respectively. The biplane can meet the calm-dawn requirement and the monoplane can meet the calm-day requirement, but neither architecture is capable of meeting the 0.51 m/s service-ceiling requirement.

The climb rate may be increased by relaxing the 515 W upper limit on battery power draw (Section 3.2.5), but this option is not evaluated here. In addition, two potential means of increasing the climb rate by changing the vehicle architecture are proposed. The first is to add a third row of exposed thrusters, as shown in Figure 34. This may improve climb performance by adding two additional emitter/collector pairs, increasing thrust.

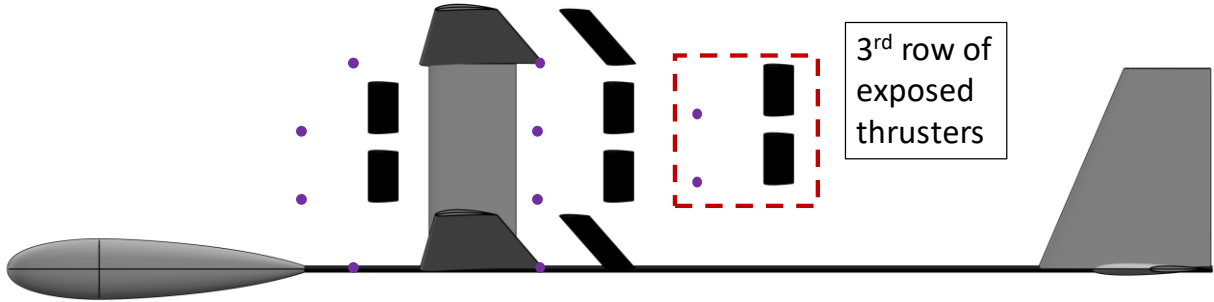


Figure 34: A potential alternate architecture for the V3, with an additional row of exposed thrusters.

The second proposed architecture change is to add a pair of tandem wings, as shown in Figure 35. As in Figure 34, two additional emitter/collector pairs are added. However, the emitters in this case are buried in the wing trailing edge, while the additional collectors double as wings. This may reduce drag relative to the architecture in Figure 34.

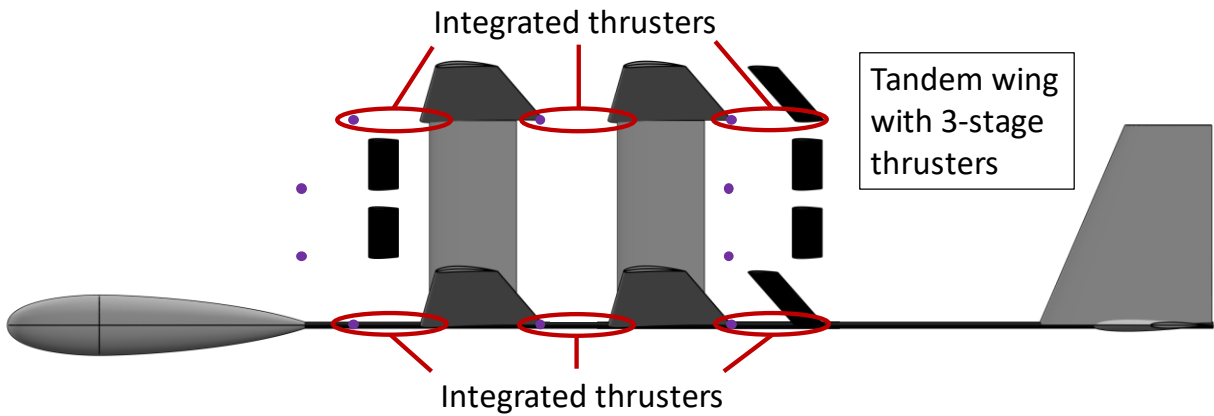


Figure 35: A potential alternate architecture for the V3, including a tandem wing with 3-stage integrated thrusters.

These alternate architectures are not assessed quantitatively in this thesis.

3.4 Chapter conclusions

The key conclusion of this chapter is that excess thrust for climb is the driving requirement for EAD fixed-wing flight: a practical EAD aircraft requires more thrust than a feasible one, in order to climb. This was not discovered until detailed design and flight testing of the V3 were well underway. Therefore, the V3 airframe would not have worked as designed.

Returning to the research question (Section 1.3), this chapter's results show that the definition of flight performance sufficient for some initial application must include a climb requirement. The V3 airframe lacks such a requirement. Furthermore, sensitivity analysis (Section 3.3.5) shows that the vehicle architectures investigated are only capable of meeting calm-day and calm-dawn climb requirements, sufficient only for flight testing under selective weather conditions. They are not capable of meeting a service-ceiling climb requirement. Therefore, with regards to answering the research question (can a practical EAD aircraft be designed and built), the results in this chapter are inconclusive.

However, a great deal is learned as regards how to design and build a practical EAD aircraft, including: requirements for a surveillance mission, thruster models, design optimization, component models, fabrication techniques, etc. These lessons are incorporated into the proceeding studies in Chapters 4 and 5.

4 Design of aircraft with ducted EAD thrusters for package delivery

4.1 Background and overview

In this thesis chapter, a family of uncrewed aircraft, powered by MSD EAD thrusters, are designed for a last-mile package delivery mission. The aircraft are capable of vertical takeoff and landing (VTOL). Unlike propeller drones, the aircraft may be nearly silent, potentially enabling package delivery missions in noise-sensitive areas (e.g., suburbs) without community noise opposition. As in Chapter 3, the goal is to design aircraft with practical capabilities, defined in Section 1.3 to mean with sufficient payload, range and/or endurance, and flight performance to be of use in some initial application (in this case, for package delivery). This would serve to answer the research question.

A concept of operations is depicted in Figure 36.

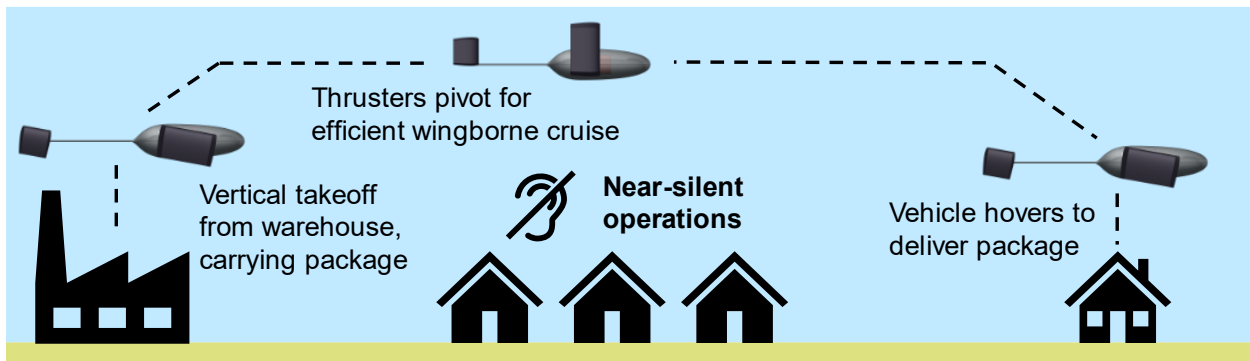


Figure 36: Concept of operations for the MSD VTOL package-delivery aircraft.

Proposed last-mile package delivery services use small UAVs to deliver packages directly to customers. Wing (a subsidiary of Alphabet), and Amazon Prime Air are among the companies experimenting with UAVs for this application [99], [100]. Hypothesized benefits of such a service, relative to existing ground transportation options such as delivery vans, include [101], [102]:

- **Greater speed:** UAVs can take direct (as the crow flies) routes and fly over traffic, reducing delivery time.
- **Lower cost:** UAVs can be both autonomous and fully electric, reducing driver and fuel costs respectively.
- **Lower environmental impact:** UAVs can be fully electric, and therefore (unlike delivery vehicles with internal-combustion engines) do not directly emit greenhouse gases that

contribute to climate change. UAVs can even in some cases produce fewer life-cycle greenhouse gases per trip than electric delivery vans [103].

As mentioned in Section 1.1, vehicle noise is a significant obstacle to the widespread adoption of AAM vehicles in general, and to urban package delivery drones in particular [1]–[4]. For example, Wing’s drone delivery trials in Canberra, Australia exceeded local noise restrictions, leading to opposition from the local community [104]. A recent drone delivery trial by a different company in Glendale, Arizona encountered community opposition for similar reasons [105]. Similar issues are expected to be encountered by other types of drone operations in urban areas.

The mission profile depicted in Figure 36 requires VTOL. However, neither the V2 nor the V3 is capable of VTOL. Therefore, the vehicles in this chapter require significant improvements in EAD thruster performance, relative to that demonstrated for the V2 and predicted for the V3. This chapter assumes the following improvements:

- **More-efficient ion generation.** The V2 and V3 are both powered by DC corona thrusters, in which the ion generation and acceleration processes are coupled (Section 2.2.2). By contrast, the vehicles designed in this thesis chapter are powered by decoupled thrusters; advanced ion sources are used to lower the energy required to generate ions. Ionization energy is discussed further in Section 4.3.2.
- **Lower-drag thruster electrodes.** The V2 and V3 are both powered by unducted EAD thrusters with wire-to-airfoil electrodes. The electrodes contribute significant portions of vehicle drag: 42% and 25% of the total drag of the V2 and V3 respectively*** (Section 3.3.3). The vehicles in this chapter use miniaturized thruster electrodes to further reduce electrode drag losses. The electrodes are contained in a duct, which contributes additional thrust (Section 2.3.3). Electrode losses are discussed further in Section 4.3.3.
- **Reduced power-converter mass.** Recall from Section 2.5 that the specific power (output power divided by mass) of the V2 power converter was 1.03 kW/kg. The same value is

*** The percentage for the V3 is lower in part due to surface integration.

used to size the V3 power converter. However, the vehicles in this study are designed using a specific power value that is ten times higher: 10.3 kW/kg. The reasons for this improvement are discussed in Section 4.3.4.

The study in this chapter is a conceptual design study. The goal is to motivate which (if any) technological advances are necessary to enable the vision in Figure 36, rather than to be restricted by the technological limits of today. This necessitates a different design philosophy from Chapter 3, in which the V3 airframe is intended to be built and flight tested by the author and collaborators. For example, the thruster model used in this chapter is physics-based rather than empirical; it uses the same equations as are developed for MSD thrusters in Section 2.3.2. The model uses decoupled thrusters, with low-power ion sources and low-drag electrodes (discussed further in Section 4.2.4). Similarly, the specific power of both the power converter and battery (Section 4.2.5) are higher than today's state-of-the-art systems.

The rest of this chapter is structured as follows. The study methods, including mission requirements, aircraft concepts, multidisciplinary design optimization, and thruster, power-electronics, and aircraft models, are given in Section 4.2. Results, sensitivity analyses, and discussions are given in Section 4.3, before the chapter conclusions in Section 4.4.

Most of the work in this chapter was previously documented in a final report for Phase I of the NASA Innovative Advanced Concepts (NIAC) program [5]. The author led the project, and developed the vehicle concepts and most of the design optimization models. The exception is the thruster model, the equations for which were developed by Nicolas Gomez Vega with some assistance from the author (see Section 2.1). The author reformulated the thruster model equations to be compatible with the signomial-programming-based optimization framework. The author generated the project results, and wrote most of the discussions in this thesis and in Ref. [5]. The exceptions are the discussions on alternative ion sources and on electrode microfabrication; these sections of Ref. [5] were written by Nicolas Gomez Vega, with some assistance from the author. The thruster experiments described in Appendix B of Ref. [5] were also conducted by Nicolas Gomez Vega.

4.2 Methods

4.2.1 Mission requirements

As mentioned in Section 4.1, Wing and Prime Air are experimenting with using uncrewed aircraft to deliver packages. Characteristics of their aircraft concepts, taken from [99], [106] and other sources, are given in Table 21.

Table 21: Characteristics of package delivery aircraft in development.

		Wing	Prime Air
Vehicle	Configuration	Lift + cruise	Tail sitter
	Mass	6.4 kg	40.4 kg
Payload	Dimensions	22.9 cm × 17.8 cm × 15.2 cm	45.7 cm × 35.6 cm × 20.3 cm
	Mass	1.2 kg	2.8 kg
	Carriage	External cardboard fairing	Internally carried box
	Delivery	Lowered via winch	Dropped at low altitude
Mission	Radius	10 km	24 km
	Speed	29 m/s	20+ m/s

Based on Table 21, the following requirements are selected for the aircraft in this study:

- **Payload mass of 1.2 kg.** This is the same as for Wing.
- **Payload dimensions of 22.9 cm × 17.8 cm × 15.2 cm** (length × width × height). Wing’s vehicle is often depicted carrying food as its payload [99]. These dimensions are sufficient to carry either two 20 fl. oz. (591 mL) coffee cups end-to-end [107], or any of the standard sizes of folded cardboard take-out food boxes [108].
- **Payload carried internally**, as with Amazon Prime Air. This is mainly done to reduce drag; it may also prevent the thrusters from causing surface charging of the payload.
- **Mission radius of 10 km.** The vehicle must fly 10 km out to a customer, drop the payload, then fly 10 km back. This is the same mission radius as for Wing.

The optimization is agnostic to payload delivery mechanism (lowered via winch vs. dropped at low altitude). Instead, the payload mount weighs a fixed fraction of the payload mass (see Section 4.2.1). No constraints on flight speed are imposed. Finally, a minimum climb rate of 1.52 m/s is imposed, consistent with the old FAA Part 23 certification requirement (see Section 3.3.5).

The mission profile is summarized in Table 22.

Table 22: Mission profile, showing the requirements for each mission segment.

Mission segment	Requirements
Takeoff	5 s in hover.
Climb	Minimum climb rate of 1.52 m/s.
Cruise out	10 km in wingborne flight.
Payload drop	20 s in hover.
Turn around	180° turn in wingborne flight, flown at a 30° bank angle.
Cruise in	10 km in wingborne flight.
Landing	5 s in hover.

Table 22 shows two types of mission segment: hover segments (takeoff, payload drop, and landing), and wingborne segments (climb, cruise out, turn, and cruise in). All hover segments require the thrust to be at least 10% greater than the vehicles' mass, accounting for both control margins and suckdown effects [62]. Meanwhile, all wingborne flight segments must be flown at an airspeed at least 20% greater than the stall speed.

As in Section 3.2.1, the requirements in this section represent a threshold for practicality, as defined by the research question (Section 1.3). Put differently, if an EAD-powered aircraft can fly the mission in Table 22 with the payload mass and dimensions listed above, it is of interest for an initial (package delivery) application. It would therefore constitute an affirmative answer to the question of whether EAD-powered aircraft can be practical.

4.2.2 Architecture enumeration

After a qualitative evaluation of architectures, a monoplane and a box wing are identified as the most promising options. To-scale sketches of both concepts are generated using Open Vehicle Sketch Pad (OpenVSP) [109]. Isometric views of the monoplane in wingborne flight and in hover are provided in Figure 37 and Figure 38 respectively; additional views are in Appendix M.

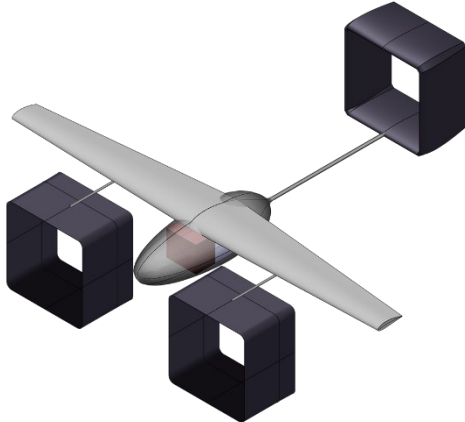


Figure 37: Isometric view of the monoplane in wingborne flight.

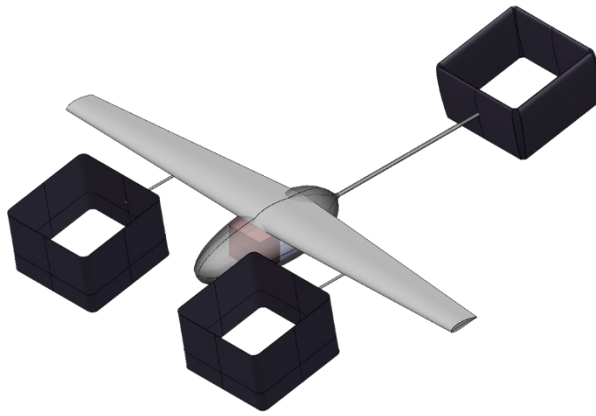


Figure 38: Isometric view of the monoplane in hover.

The monoplane consists of a fuselage pod, wing, and tail boom. It also has three MSD thrusters, depicted in black. In Figure 37, the thrusters are level, providing thrust in wingborne flight. In Figure 38, the thrusters tilt, providing lift in hover.

The first thruster is at the rear of the airplane. It also serves as the tail; i.e., it provides stability, and has an elevator and rudder for control. A similar idea underlies the design of the TailFan, a concept aircraft discussed by Hahn [110]; this aircraft is powered by a ducted propeller that also serves as part of the tail group. The two remaining EAD thrusters (hereafter called the forward thrusters) are located under each wing, and are offset forward of the wing by forward booms. This offset serves to position them forwards of the aircraft center of gravity (CG), so that the aircraft thrust balances in hover.

Isometric views of the box wing in wingborne flight and in hover are provided in Figure 39 and Figure 40 respectively; additional views are in Appendix M.

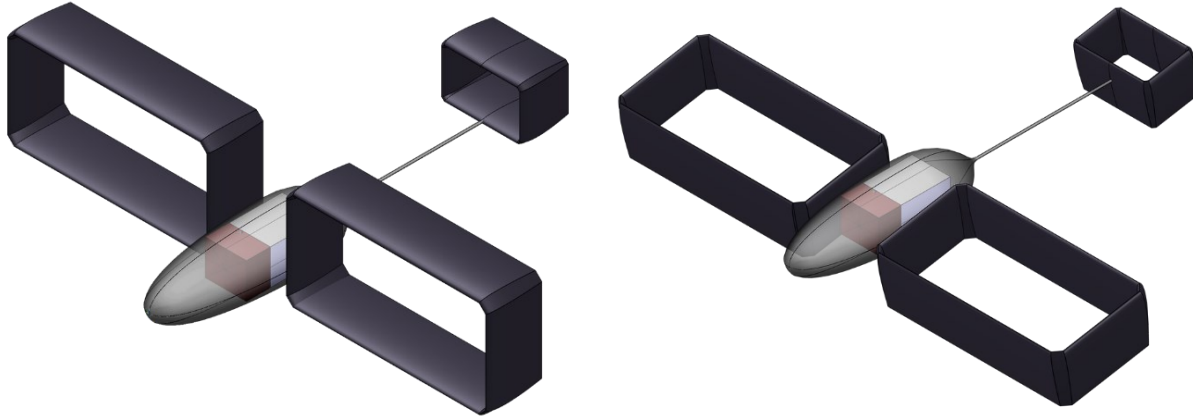


Figure 39: Isometric view of the box wing in wingborne flight.

Figure 40: Isometric view of the box wing in hover.

Like the monoplane, the box wing consists of a fuselage pod, tail boom, and box-tail thruster. However, instead of a conventional wing and two forward thrusters, the box wing doubles as a thruster. The box wing tilts forwards in hover, so that its thrust vector is forwards of the CG, ensuring the aircraft balances.

For the purpose of design optimization, the box wing upper and lower sections are assumed to carry 50% of the lift each, independent of thrust. This approximation is discussed further in Appendix O. Hover balance modeling for both vehicles is discussed in Appendix P.

4.2.3 Multidisciplinary design optimization

The aircraft in this chapter are designed using a custom SP-based optimization framework, as in Chapter 3. The generic problem formulation in Table 8 applies, with the specifics adapted to last-mile package delivery. The requirements in Table 22, such as the minimum climb-rate requirement of 1.52 m/s, are imposed as optimization constraints.

Takeoff mass (minimize) is used as the objective function. Optimization data, including number of free variables, constraints, and typical optimization solve times, is provided in Table 23.

Table 23: Number of free variables, number of constraints, and typical solve times on a laptop computer for design optimization of the package-delivery aircraft.

	Monoplane	Box wing
Free variables	1663	1525
Constraints	3339	3063
Typical solve time	1.0 s	2.9 s

4.2.4 Thruster models

Thruster performance is computed using the one-dimensional model in Section 2.3.2, which includes the effect of freestream velocity. However, two changes are required. Firstly, Equations (11), (12), (14), (18), (20), and (24) are not solved in their respective forms. Instead, they are rearranged. This is discussed further in Appendix N. Secondly, signomial programs do not directly allow for integer design variables. Therefore, number of thruster stages is approximated as a continuous variable, rather than as an integer.

Unless otherwise specified, the MSD thrusters in this study are modeled using the parameters in Table 24. Standard sea-level values for air density and kinematic viscosity are used, while electric permittivity assumes that the values for air and for a vacuum are the same [111]. Ion mobility is obtained from Ref. [25], and is consistent with EAD thruster experiments conducted by Nicolas Gomez Vega [19]. Ionization energy and stage loss coefficient are discussed further in Sections 4.3.2 and 4.3.3 respectively. Finally, Table 24 includes upper limits on voltage and exit area ratio. The former limit is included to prevent the thrusters from sparking (arcing), while the latter limit prevents flow separation in the nozzle.

Table 24: Thruster model parameter values.

Parameter	Symbol	Value
Electric permittivity	ϵ	$8.85 \times 10^{-12} \frac{\text{F}}{\text{m}}$
Ion mobility	μ	$2.0 \times 10^{-4} \frac{\text{m}^2}{\text{s V}}$
Elementary charge	e	$1.6 \times 10^{-19} \text{ C}$
Gap spacing	d	10 mm
Ionization energy	E_{ion}	66 eV
Stage loss coefficient	K_L	2.0×10^{-3}
Duct wall friction interference factor	Q_{wall}	1.1
Maximum applied voltage	V_{\max}	10 kV
Maximum exit area ratio	ϕ_{\max}	1.0

4.2.5 Power-electronics models

As in Chapter 3, the power-electronics system consists of the battery and the power converter. Sizing parameters for both components are given in Table 25.

Table 25: Power-electronics sizing parameters.

Parameter		Value
Battery	Specific energy	$200 \frac{\text{Wh}}{\text{kg}}$
	Specific power	$4 \frac{\text{kW}}{\text{kg}}$
	Density	$2.4 \frac{\text{kg}}{\text{L}}$
Power converter	Specific power	$10.3 \frac{\text{kW}}{\text{kg}}$
	Efficiency	85%

The battery is sized using a fixed specific energy, specific power, and density. The specific energy (200 Wh/kg) is consistent with existing prototype lithium-ion batteries (Table 3). However, the specific power (4 kW/kg) is about twice that of existing batteries. This choice is discussed further in Section 4.3.5.

The power converter is sized using a fixed specific power and efficiency. The efficiency (85%) is consistent with that of the V2 (Table 4); however, the specific power (10.3 kW/kg) is approximately ten times higher. This choice is discussed further in Section 4.3.4. Unlike in Chapter 3, no upper limit on battery power draw is imposed.

4.2.6 Aircraft mass, drag, and structural models

The mass, drag, and structural models in this chapter are developed using a similar approach to those of the V3 (Section 3.2.6). However, some of the specifics differ. They are discussed further in this section.

The vehicles in this study are primarily constructed from carbon fiber, Kevlar, and foam. As with the V3, Kevlar is chosen over carbon fiber for many key components, due to its electrically insulative properties. However, unlike with the V3, balsa wood is not used.

Mass models generally use a component build-up approach, using component dimensions, material densities, and component-specific mass margins. If a component is made of composites (either

carbon fiber or Kevlar), its material density is doubled. This rule of thumb accounts for resin mass, and is a key lesson from the V3 build and flight test campaign (see Appendix L).

Components with structural models are sized using engineering beam theory. For example, the wing structural model is similar to that documented in Appendix C for the V3. The main difference is that the spars in this chapter have a foam core and a carbon-fiber shear web, instead of a balsa core and no web as for the V3. Therefore, shear loads are taken by the web, instead of the core.

The monoplane and box wing thrusters both require tilting mechanisms, to change the thrusters' orientation while transitioning between hover and wingborne flight (Section 4.2.2). Each tilting mechanism is assumed to weigh 25% of the sum of the mass of its respective thruster and nacelle.

Drag models are also developed using a component build-up approach. Profile drag of airfoil components is estimated using a fit to Xfoil airfoil data, as is documented for the V3 wing in Appendix D. Profile drag of other components is estimated using equivalent flat-plate models.

Aircraft-level sizing parameters are summarized in Table 26. The monoplane wing taper ratio is set to 0.5, for similar reasons to that of the V3 (Section 3.2.7.3). However, the box-wing taper ratio is set to 1.0. This way, its chord is constant; it can therefore more easily serve as a thruster nacelle. Induced drag is estimated using a constant Oswald efficiency; the box wing includes an adjustment for interference between wings (see Appendix O). 10% margins on mass and drag at the aircraft level (in addition to component margins) are maintained.

Table 26: Aircraft-level sizing parameters for vehicles with ducted thrusters.

Parameter	Value
Aircraft mass margin	10%
Aircraft drag margin	10%
Monoplane wing taper ratio	0.5
Box wing taper ratio	1.0
Wing Oswald efficiency	0.8
Wing maximum lift coefficient	1.5

Nacelle components with thrusters inside have drag losses divided into two components. Drag from the outside of the component (facing the freestream) is modeled as profile drag, and is

described in this section. Drag from the inside of the component (facing the thruster electrodes) is modeled as a thrust loss, and is described in Section 2.3.

Details of the mass, profile drag, and structural models are summarized in Table 27. Further modeling details specific to the box wing are discussed in Appendix O.

Table 27: Mass, profile drag, and structural models for vehicles with ducted thrusters.

Component	Mass model	Profile drag model	Structural model
Fuselage pod	Kevlar skin (2 plies). 50% mass margin for internal structure.	Equivalent turbulent flat-plate drag with a form-factor adjustment [62]. 20% interference factor.	n/a
Tail boom	Hollow Kevlar cylindrical tube. 10% mass margin.	Equivalent turbulent flat-plate drag. No interference factor.	Cantilever load from tail-thruster thrust in hover. Bending, shear, and tip-deflection (max 5% of boom length) constraints. Factor of safety of 3.
Monoplane wing	Spar: carbon-fiber spar caps and shear web; foam spar core. 20% mass margin. Wing: spar, plus Kevlar skin (1 ply). 30% mass margin.	Fit to NACA 44XX airfoil data: $C_d = f\left(\frac{t}{c}, \text{Re}, C_L\right)$. Fit RMS error: 1.8%. 20% interference factor.	Loads from a symmetric pull-up at cruising speed, with a load factor of 2.5. Constant beam curvature [92]. Bending, shear, and tip-deflection (max 5% of wingspan) constraints. Factor of safety of 1.5.
Box-wing horizontal section	Same as monoplane wing.	Fit to NACA 44XX airfoil data: $C_d = f\left(\frac{t}{c}, \text{Re}, C_L\right)$. Fit RMS error: 4.3%. 20% interference factor.	Same as monoplane wing, with the upper and lower sections each carrying 50% of the lift.
Box-wing vertical section	Kevlar skin (1 ply); High Load 60 (blue foam) spar (10% of section chord). 20% mass margin.	Fit to NACA 00XX airfoil data: $C_d = f\left(\frac{t}{c}, \text{Re}\right)$. Fit RMS error: 1.6%. 20% interference factor.	n/a
Box wing	2 horizontal sections + 4 vertical sections. 30% mass margin.	Inherited from monoplane wing and vertical sections. 20% interference factor.	Inherited from monoplane wing.

Box tail	Kevlar skin (1 ply); High Load 60 (blue foam) core. 20% mass margin.	Fit to NACA 00XX airfoil data: $C_d = f\left(\frac{t}{c}, \text{Re}\right)$. Fit RMS error: 2.3%. 10% interference factor.	n/a
Forward thruster nacelles (monoplane only)	Kevlar skin (2 plies). 50% mass margin for structure.	Equivalent flat-plate drag, assuming the flow trips (becomes turbulent) at the nozzle. 20% interference factor.	n/a
Forward thruster booms (monoplane only)	Hollow Kevlar cylindrical tubes. 10% mass margin.	Equivalent turbulent flat-plate drag. No interference factor.	Cantilever load from forward-thrusters thrust in hover. Bending, shear, and tip-deflection (max 5% of boom length) constraints. Factor of safety of 3.
Landing gear	4% of aircraft unmargined mass.	5% of aircraft unmargined profile drag.	n/a
Payload mount	25% of payload mass.	n/a	n/a
Battery	Fixed specific energy, power, and volume (see Section 4.2.5).	n/a	n/a
Thrusters	Grid of tungsten wires (see Section 4.2.7.2).	Modeled as a thrust loss rather than as drag, via the loss coefficient (Section 2.3).	n/a
Thruster tilting mechanisms	25% of respective thruster + nacelle mass.	n/a	n/a
Avionics	2% of aircraft unmargined mass.	n/a	n/a

4.2.7 Dimensional models

4.2.7.1 Fuselage pod

The purpose of the fuselage pod is to hold the battery, payload, power converter, and avionics. A cutaway of the monoplane fuselage pod is shown in Figure 41. The box wing uses a similar design.

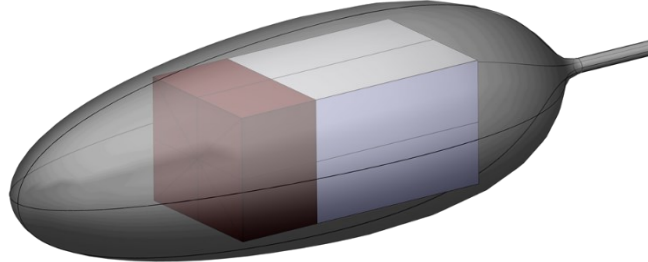


Figure 41: A cutaway of the monoplane fuselage pod.

The fuselage pod is shaped like an ellipsoid. Figure 41 shows the battery (red) and the payload (blue). Both of these components are shaped like rectangular prisms. The battery length, width, and height are optimization variables; its volume is modeled via its density (Table 25). Payload dimensions are discussed in Section 4.2.1.

In order to ensure that the battery and payload fit inside the fuselage pod, a “usable volume” is defined. The usable volume is shaped like a rectangular prism; the battery and payload must fit inside it. The usable volume is modeled by enforcing the constraint

$$1 \geq \left(\frac{l_{\text{usable}}}{0.95 l_{\text{pod}}} \right)^2 + \left(\frac{w_{\text{usable}}}{0.95 w_{\text{pod}}} \right)^2 + \left(\frac{h_{\text{usable}}}{0.95 h_{\text{pod}}} \right)^2 \quad (67)$$

where l , w , and h refer to length, width, and height respectively. The subscripts $(\)_{\text{pod}}$ and $(\)_{\text{usable}}$ refers to the fuselage pod and usable volume respectively; the factor of 0.95 is a margin.

Since the payload and battery are aligned lengthwise, the sum of their lengths must not exceed the usable fuselage-pod length. This is enforced via the constraint

$$l_{\text{usable}} \geq l_{\text{battery}} + l_{\text{payload}} \quad (68)$$

Finally, battery and payload width and height constraints are defined as

$$w_{\text{usable}} \geq w_{\text{battery}} \quad (69)$$

$$w_{\text{usable}} \geq w_{\text{payload}} \quad (70)$$

$$h_{\text{usable}} \geq h_{\text{battery}} \quad (71)$$

$$h_{\text{usable}} \geq h_{\text{payload}} \quad (72)$$

The avionics system and power converter lack volume models, and are therefore not shown in Figure 41. However, Figure 41 shows that there is additional room in the fuselage. Therefore, the avionics system is located in the nose (in front of the battery), while the power converter is located behind the payload. These assumptions are used for center-of-gravity analysis (Appendix P).

4.2.7.2 Thrusters and nacelles

The thruster electrodes are modeled as a grid of cylindrical wires, as shown in Figure 42.

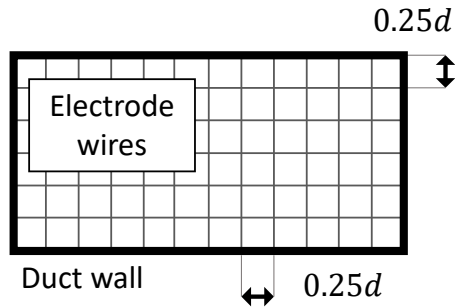


Figure 42: Front view of an MSD thruster duct, showing the electrode geometry.

The grid wires are made of tungsten, and are 56 microns in diameter. Wires with these properties have been used as emitter electrodes in MSD thruster experiments [64]. The spacing between wires, as shown in Figure 42, is defined as 25% of the gap spacing (i.e., 2.5 mm in this example). Two grids are required per stage: one grid for the emitters, and one for the collectors. Whether this geometry would work in practice is uncertain.

The thruster stage length is then defined as 20% greater than the stage gap spacing, a margin added to avoid counter-ionic wind [23]. The duct length is the sum of the lengths of the individual stages. Finally, the nozzle length is defined as 20% of the duct length.

The box tail and monoplane forward-thruster nacelles lack structural models (see Table 27). Instead, an upper limit on nacelle aspect ratio is imposed.

Sizing parameters for the thrusters and nacelles are summarized in Table 28.

Table 28: Thruster and nacelle model parameter values.

Parameter	Value
Electrode wire spacing	25% of stage gap spacing
Electrode wire diameter	56 microns
Thruster stage length	20% greater than gap spacing
Thruster nozzle length	20% of duct length
Nacelle maximum aspect ratio	1.5

4.2.7.3 Box tail

Both the monoplane and box wing include a box tail, which serves two purposes. Firstly, the box tail provides static stability and control (via control surfaces) in wingborne flight. Secondly, it houses a thruster that provides thrust in both hover and wingborne flight.

Minimum tail sizes for static stability are modeled using tail volume coefficients; i.e., using Equations (62)-(63). These equations can be directly applied to the box wing, with appropriate definitions for planform area^{†††}. However, the monoplane's forward thrusters have a destabilizing influence, since they are located forwards of the aircraft center of gravity (see Appendix P). This is accounted for by extending Equations (62)-(63) to obtain

$$C_{HT} + \frac{2l_{FT}(S_H)_{FT}}{bS_W} \leq \frac{l_{HT}S_{HT}}{bS_W} \quad (73)$$

$$C_{VT} + \frac{2l_{FT}(S_V)_{FT}}{bS_W} \leq \frac{l_{VT}S_{VT}}{\bar{c}S_W} \quad (74)$$

where the subscript $(\)_{FT}$ refers to the forward thrusters, and $(S_H)_{FT}$ and $(S_V)_{FT}$ are the total forward-thruster horizontal and vertical planform areas respectively. A factor of 2 is included, because the monoplane has two forward thrusters.

^{†††} The box wing planform area S_W is the sum of the planform areas of the upper and lower surfaces. The horizontal-tail planform area S_{HT} is the sum of the planform areas of the upper and lower box-tail surfaces. Finally, the vertical-tail planform area S_{VT} is the sum of the planform areas of the left and right box-tail surfaces.

The box tail lacks a structural model (see Table 27). However, it is also a thruster nacelle, and so it is subject to the same constraint on maximum aspect ratio as for the monoplane forward-thruster nacelles (see Section 4.2.7.2).

Tail volume coefficients are provided in Table 29. They are identical to those used by Burton & Hoburg [81], and are also consistent with RC aircraft design guidelines [94].

Table 29: Tail volume coefficients for vehicles with ducted thrusters.

Component	Volume coefficient
Horizontal tail	0.45
Vertical tail	0.04

4.3 Results

4.3.1 Design optimization results

A summary of the optimization results is provided in Table 30. Isometric views of both vehicles are provided in Section 4.2.2; additional views are provided in Appendix M. Detailed dimensional data, mass breakdowns, and detailed performance data for both vehicles are provided in Appendix Q, Appendix R, and Appendix S respectively.

Table 30: Summary of the design optimization results for the MSD package-delivery aircraft.

	Monoplane	Box wing
Length	1.62 m	1.51 m
Wingspan	2.21 m	1.60 m
Wing area	0.492 m ²	0.772 m ²
Takeoff (total) mass	20.8 kg	18.6 kg
Payload mass	1.2 kg	1.2 kg
Battery mass	7.5 kg	6.7 kg
HVPC mass	2.5 kg	2.2 kg
Empty mass fraction	0.46	0.46
Cruising speed	25.5 m/s	25.2 m/s
Cruise lift coefficient	1.04	0.60
Cruise drag coefficient	1019 counts	607 counts
Cruise lift-to-drag	10.2	10.0
Cruise thrust	19.9 N	18.3 N
Cruise electrical power	5.6 kW	5.0 kW
Cruise overall efficiency	9.1%	9.3%
Hover thrust	224.0 N	200.4 N
Hover electrical power	29.9 kW	26.8 kW

Mass and cruise drag breakdowns are provided in Figure 43 and Figure 44 respectively. Note that only the monoplane has forward nacelles and booms; the box wing lacks these components.

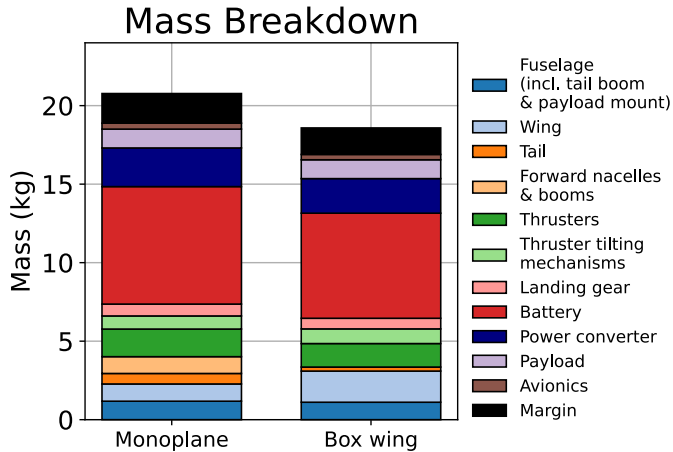


Figure 43: Mass breakdown for the MSD VTOL package-delivery aircraft.

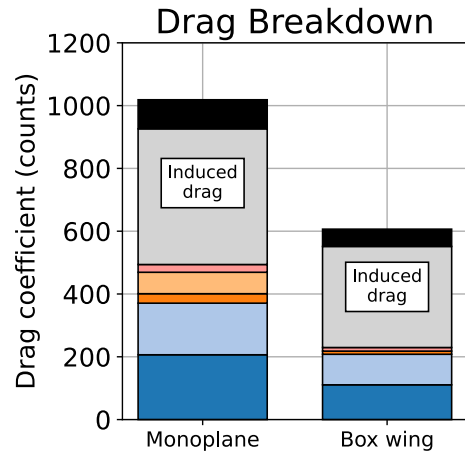


Figure 44: Cruise drag breakdown for the MSD VTOL package-delivery aircraft.

Figure 43 shows that the battery accounts for the single largest fraction of the mass: 36% for both vehicles. The second-heaviest component is the power converter, which accounts for a further 12% of the mass. Tabulated mass breakdowns for both vehicles are given in Appendix R.

Figure 44 shows that the largest drag component is induced drag (drag due to lift): 43% and 53% of the total for the monoplane and box wing respectively. In addition, the monoplane cruise drag coefficient (1019 counts^{†††}) is almost twice that of the box wing (607 counts). This is not because the monoplane generates substantially more drag: monoplane cruise drag is 19.9 N, vs. 18.3 N for the box wing (Appendix S). Drag area (drag divided by dynamic pressure) in cruise is also not substantially different: 0.050 m² for the monoplane, vs. 0.047 m² for the box wing. Instead, the disparity in drag coefficient exists because the box-wing planform area (0.772 m²) includes the planform area of both the upper and lower wings; it is therefore almost twice as large as the monoplane wing (0.492 m²). Since the drag coefficient is referenced to the planform area, a higher planform area results in a lower drag coefficient.

While drag from the thruster nacelles is shown in Figure 44, drag from the thrusters is not. This is because thruster aerodynamic losses (from the electrodes and the inside of the duct walls) are

^{†††} Recall from Section 3.3.1 that counts reference the drag coefficient, multiplied by 10⁴.

modeled as a decrease in thrust, rather than as a contribution to drag. This is discussed further in Sections 2.3 and 4.2.6.

The optimizer generates converged solutions for both the monoplane and box wing, indicating that vehicles with the required capabilities can be designed and built. However, this result is contingent on the values of four key input parameters, which require further discussion:

- **Ionization energy E_{ion} :** the amount of electrical energy required to generate one ion.
- **Stage loss coefficient K_L :** pressure losses due to drag from one stage of thruster electrodes.
- **HVPC specific power p_{HVPC} :** power-converter output electrical power per unit mass.
- **Battery specific power p_{battery} :** output electrical power per unit mass of the battery.

Each of these parameters is discussed in detail in the following four sections.

4.3.2 Ionization energy

4.3.2.1 Sensitivity

As shown by Equation (24), the thruster electrical power draw is split into two components: ionization power and acceleration power. Ionization power is modeled via Equation (25); it is linearly related to E_{ion} , the amount of electrical energy required to generate one ion.

A sensitivity analysis with respect to ionization energy is shown in Figure 45. Each point represents an optimized vehicle design; ionization energy is the only input parameter that is varied.

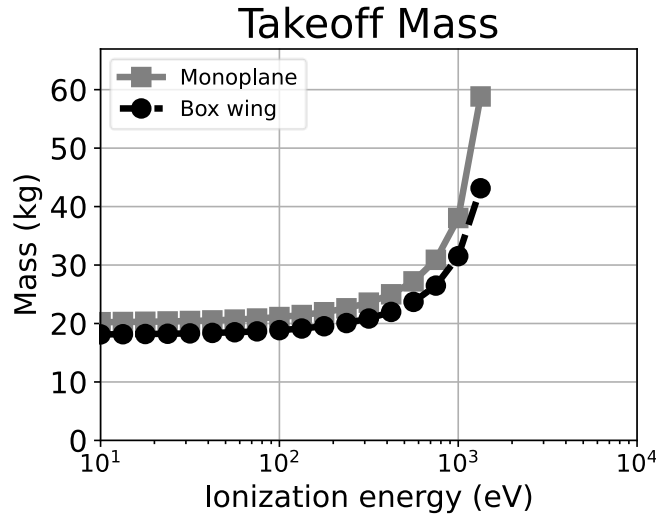


Figure 45: Vehicle takeoff mass vs. ionization energy.

4.3.2.2 Discussion

Figure 45 only shows data for $E_{\text{ion}} \lesssim 1,000$ eV. This is because the optimizer does not converge for ionization energies higher than this. Therefore, E_{ion} must be less than approximately 1,000 eV in order for the vehicles in this study to be feasible.

The default value of E_{ion} used in this study is 66 eV (see Table 24). This corresponds to the optimum energy required to generate an ion via electron impact in an electric field, and is known as Stoletov's constant [112]. This constant is discussed further in Section 4.1.6 of Ref. [113]. By contrast, experiments with EAD thrusters that use a dielectric barrier discharge (DBD) ion source [17] yielded an ionization energy of approximately 10,000 eV per ion, an order of magnitude greater than required here. These experiments are discussed further in Section 5.2.4 of Ref. [114].

As mentioned in Section 2.2.1, decoupled thrusters may use ion sources other than DBDs. Ionization energies for alternative ion sources, taken from Ref. [5], are given in Table 31.

Table 31: Ionization energies for alternative ion sources.

Ion source	Ionization energy
Nanosecond repetitively pulsed (NRP) discharge	350 eV
Electron impact (optimum)	66 eV
Photoelectric effect	4.2 eV
Photoionization	15.6 eV
Radioactive decay	0 eV

All of the ion sources listed in Table 31 have ionization energies below the required 1,000 eV, indicating that the vehicles in this study may be feasible if they are used in the vehicles' MSD thrusters. However, while these ion sources have been demonstrated experimentally, none have (to the author's knowledge) been applied to EAD propulsion. Discussions for each ion source are provided in Ref. [5].

Radioactive decay has the lowest ionization energy of the candidate ion sources listed in Table 31. Such a system would consist of an unstable atomic isotope that undergoes alpha or beta decay; the resulting helium nuclei (alpha particles) or high-energy electrons (beta particles) would then

produce ions by colliding with neutral molecules [5]. This process is passive, requiring no electrical energy from the battery; as a result, $E_{\text{ion}} = 0$.

A similar system is used in household smoke detectors. These devices incorporate the isotope Americium-241, which undergoes alpha decay. The alpha particles are released into an ionization chamber; they then interact with air molecules to produce ions and electrons. A voltage is then applied across the chamber, producing a current. The current is affected by the presence of smoke in the ionization chamber, so smoke can be detected by measuring the current [115].

Corona ion sources are not included in Table 31. This is because the ion generation and acceleration mechanisms of a corona thruster are coupled, so ionization power (and, by extension, ionization energy) cannot easily be obtained separately from acceleration power. This is discussed further in Section 2.2.2.

4.3.2.3 Summary

It can be concluded from this section that the value of ionization energy required by the vehicles in this study (at most 1,000 eV) is an order of magnitude lower than values achieved experimentally to date for EAD thrusters (10,000 eV). However, alternative methods of ion generation with ionization energies well below the required value exist. Therefore, it may be possible to design an ion generation system incorporating one or more of these mechanisms into an EAD thruster. Further research into the design and fabrication of such a system is recommended as part of future work.

4.3.3 Stage loss coefficient

4.3.3.1 Sensitivity

As shown by Equation (13), the stage loss coefficient K_L represents pressure losses per thruster stage due to drag from the electrodes. K_L is the internal-flow system equivalent to the drag coefficient (C_D) of an external-flow system.

A sensitivity analysis is conducted with respect to stage loss coefficient. Results are in Figure 46. As with Figure 45, each point on the plot represents an optimized vehicle design; loss coefficient is the only input parameter that is varied.

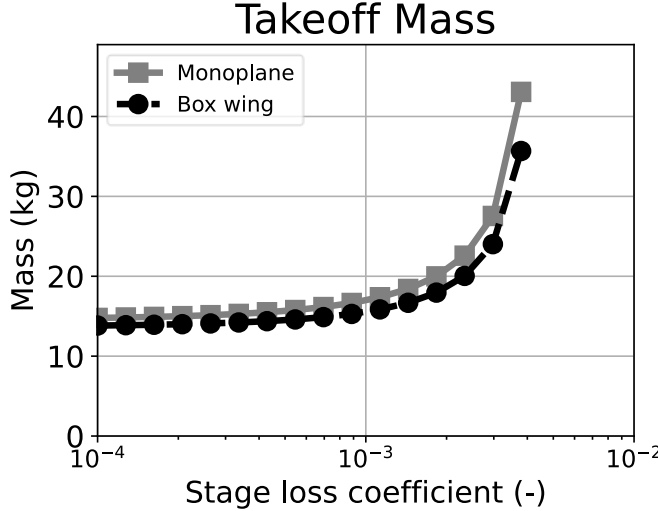


Figure 46: Vehicle takeoff mass vs. stage loss coefficient.

4.3.3.2 Discussion

Figure 46 only shows data for $K_L \lesssim 4.0 \times 10^{-3}$, because the optimizer does not converge for higher values. Therefore, K_L must be less than approximately 4.0×10^{-3} in order for the vehicles in this study to be feasible.

Recall from Section 4.2.7.2 that the thruster electrodes consist of a grid of cylindrical wires. Table 5 shows that this geometry is directly used to compute the grid mass (by knowing the wire spacing, diameter, and material density). However, thruster losses are modeled via K_L , which is an input parameter independent of geometry.

The loss coefficient can also be estimated based on the grid geometry output from the optimizer. Modeling approximations are as follows:

- Each stage has 2 grids: the emitter grid and the collector grid.
- The wires are cylindrical, so their drag can be estimated using cylinder drag coefficients.
- The local flow velocity is equal to the thruster bulk velocity v_2 .

Under these conditions, the stage loss coefficient can be estimated using

$$(K_L)_{\text{wire}} = \frac{D_{\text{wire}}}{\frac{1}{2} \rho v_2^2 A_2} \quad (75)$$

where $(K_L)_{\text{wire}}$ is the wire loss coefficient due to wire drag. D_{wire} is obtained from the cylinder drag model in Appendix F, with l_{wire} equal to the emitter + collector wire length (estimated using the grid geometry discussed in Section 4.2.7.2).

Equation (75) is applied to the thrusters on both aircraft, across all four mission segments with distinct thruster data (hover, cruise, climb, and bank). Results are in Table 32.

Table 32: Stage loss coefficients, estimated using Equation (75).

		Stage loss coefficient			
Aircraft	Thruster	Hover	Cruise	Climb	Bank
Monoplane	Box-tail thruster	0.15	0.14	0.14	0.14
	Forward thrusters	0.15	0.14	0.14	0.14
Box wing	Box-tail thruster	0.15	0.14	0.14	0.15
	Box-wing thruster	0.15	0.14	0.14	0.15

Table 32 shows that the stage loss coefficients range from 0.14-0.15, about 70-75 times higher than the loss-coefficient value of 2.0×10^{-3} used by default by the optimizer (Table 24). Moreover, Figure 46 shows that the optimizer does not converge with loss coefficients this high. A reduction is needed for the vehicles in this study to be feasible.

The following geometric means of reducing the loss coefficient are investigated:

- **Using vertical wires only**, eliminating the horizontal wires. The wire length (and by extension, the loss coefficient) is thus reduced by a factor of 2. The resulting electric field is still approximately one-dimensional, consistent with the thruster modeling approximations in Section 2.3.2.
- **Increasing the wire spacing** from 25% to 100% of the gap spacing. This reduces the loss coefficient (again via wire length) by a factor of 4. This wire spacing has been used in MSD thruster experiments [64].
- **Reducing the wire diameter** to 7.6 microns. The default value of 56 microns is based on MSD thruster experiments [64], but tungsten wires as small as 7.6 microns in diameter can be obtained commercially [116].

- **Using streamlined electrode units**, combining the emitter, collector, and ion source. This technique reduces drag by eliminating exposed components, in a similar manner to semi-integrated thrusters (Section 3.2.2.1). A proposed implementation is shown in Figure 47.

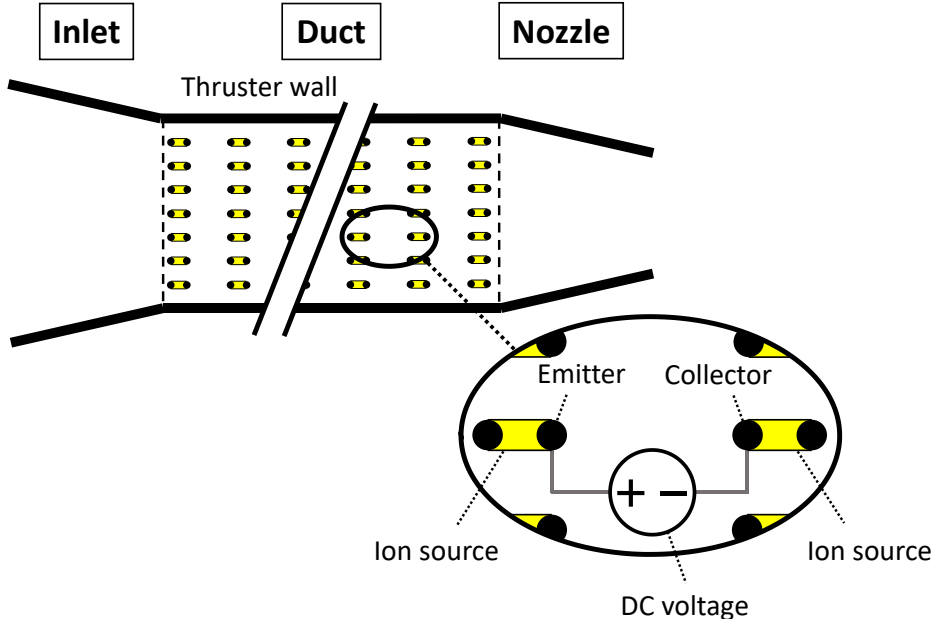


Figure 47: Side view of a proposed geometry for a streamlined electrode unit. Each unit consists of an emitter, a collector (black cylinders), and an ion source (yellow).

Microfabrication techniques may be used to manufacture the streamlined electrode units in Figure 47. Potentially applicable microfabrication techniques are discussed in Ref. [5].

The first three listed means of reducing the loss coefficient are modeled via Equation (75), simply by changing the wire length and diameter used to estimate wire drag. However, Figure 47 shows that the streamlined electrode units are roughly ellipsoidal in shape. Estimates for ellipsoid drag at such low Reynolds numbers (about 8-14; see Table 40) could not be obtained. Instead, the drag of a streamlined electrode unit is approximated as that of a cylinder, with the same diameter as the collector wires. This eliminates the emitter drag, reducing the loss coefficient by a factor of 2.

The listed geometric loss-coefficient reduction techniques are applied successively to each thruster. Results are in Figure 48 and Figure 49 for the monoplane and box wing respectively. Note that the plot y-axes are logarithmic.

Monoplane

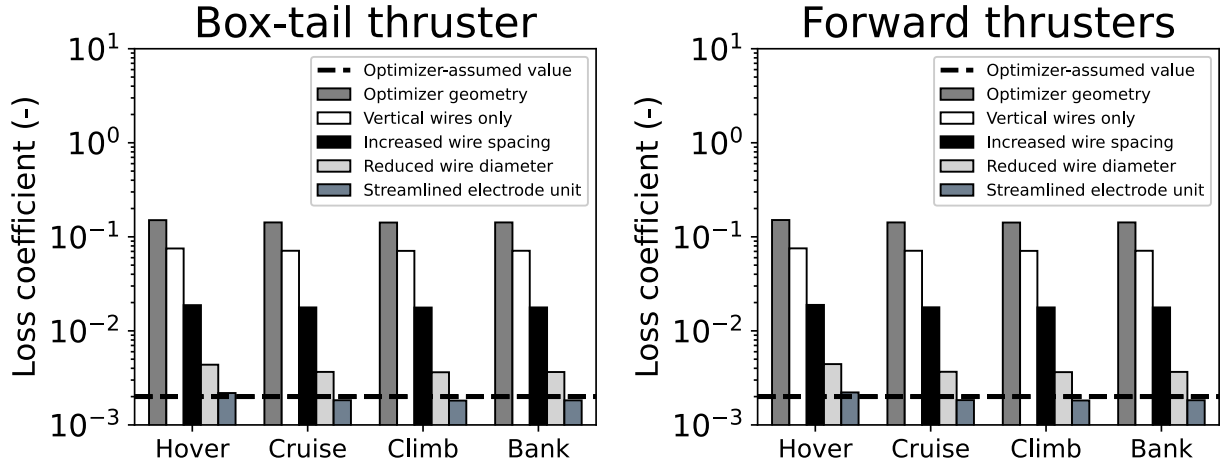


Figure 48: Thruster stage loss coefficient as a function of grid geometry model for the monoplane.

Box wing

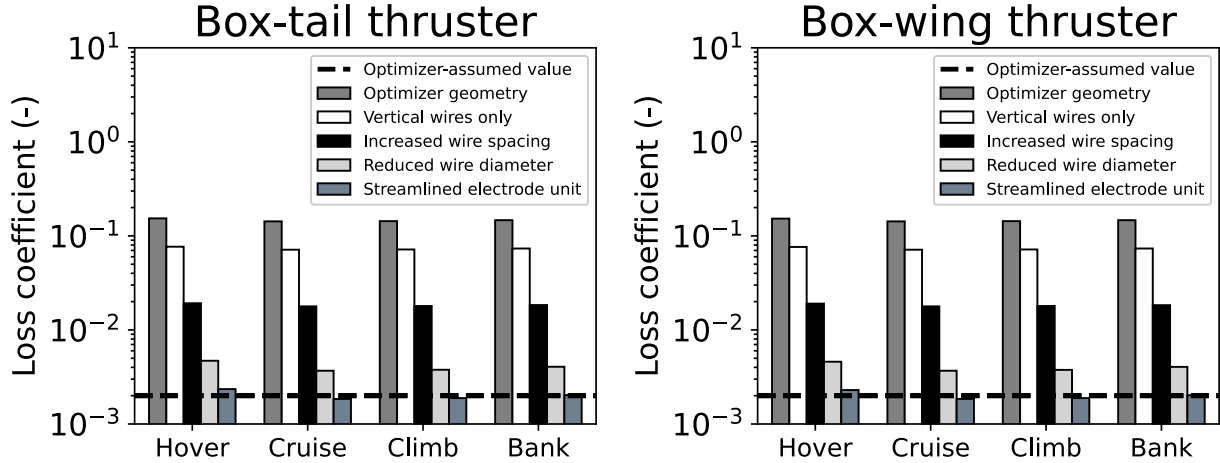


Figure 49: Thruster stage loss coefficient as a function of grid geometry model for the box wing.

Figure 48 and Figure 49 show that the loss coefficient decreases as each successive geometry modification is applied. If all four changes are applied at once (the “streamlined electrode unit” bars), the loss coefficient is approximately equal to the optimizer default value of 2.0×10^{-3} (the black dotted lines). Therefore, it may be possible to obtain a stage loss coefficient low enough to enable the vehicles in this study. However, these grid geometries have yet to be demonstrated experimentally.

4.3.3.3 Summary

It can be concluded from this section that the default thruster electrode geometry (Section 4.2.7.2) results in stage loss coefficients too high for the vehicles in this study to be feasible. However, reductions in loss coefficient sufficient to render the vehicles feasible can be obtained by modifying the geometry, and micromanufacturing techniques may be used to build the resulting advanced electrode geometries. Further research into the design and fabrication of suitable electrodes is recommended as part of future work.

4.3.4 Power-converter specific power

4.3.4.1 Sensitivity

As discussed in Section 4.2.5, the power-converter specific power p_{HVPC} is equal to the maximum available output power of the power converter, divided by its mass.

A sensitivity analysis with respect to power-converter specific power is shown in Figure 50. As in the preceding sensitivity analyses, each point on the plot represents an optimized vehicle design.

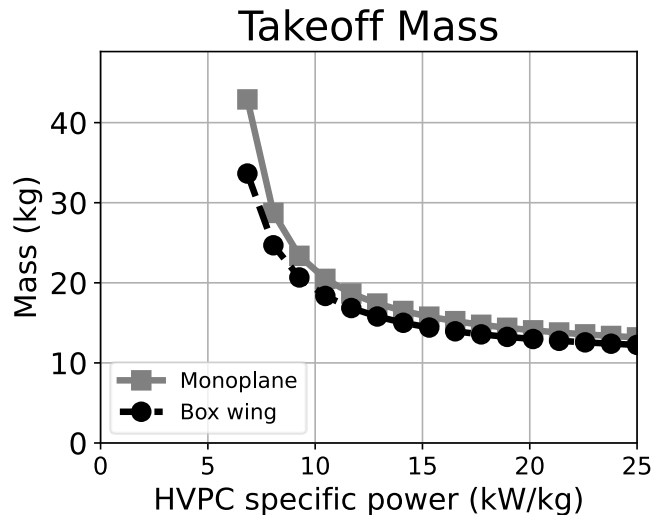


Figure 50: Vehicle takeoff mass vs. power-converter specific power.

4.3.4.2 Discussion

Figure 50 only shows data for $p_{\text{HVPC}} \gtrsim 7 \text{ kW/kg}$. This is because the optimizer does not converge for specific power values lower than this. Therefore, p_{HVPC} must be less than approximately 7 kW/kg in order for the vehicles in this study to be feasible. By contrast, the V2 power converter

had a specific power of approximately 1.03 kW/kg (Table 4). The default specific power in this study (10.3 kW/kg) is ten times higher.

Recall from Section 2.5 that power-converter mass can be reduced by increasing the input voltage, lowering the output voltage, or reducing the output power. Each of these parameters can therefore help explain why a significant increase in p_{HVPC} (relative to the V2) may be achievable for the vehicles in this study. Details are as follows:

- **Higher input voltage**, due to a larger battery. The V2 battery had a mass of 0.23 kg (Table 1), while the vehicles in this study have battery masses of 6-8 kg (Table 30), more than 25 times greater. Since battery pack voltage can be increased by wiring cells together in series, the pack voltages (V_{in}) of the vehicles in this study can be higher than the V2 pack voltage, reducing HVPC mass.
- **Lower output voltage**, due to multistaging. This is one of the advantages of MSD thrusters, relative to their exposed counterparts: multiple miniaturized thruster stages allow for a lower power-converter output voltage. The V2 thrusters required a voltage of 40 kV (Table 1), while the thrusters in this study use a maximum voltage of only 10 kV (Table 24). This should lead to additional mass reductions.
- **Higher output power**. Power-converter specific power roughly scales with $P_{\text{out}}^{0.25}$ [10]. The V2 power-converter maximum output power was approximately 527 W (Section 2.5), while those of the monoplane and box wing are more than 40 times greater: 25.4 kW and 22.8 kW respectively (Table 55 and Table 56). This effect alone should increase specific power of both vehicles by a factor of approximately 2.6.

Further specific-power improvements should also be possible due to the difference between continuous and burst power, as follows. Many power-electronic devices have burst power limits that are higher than their continuous-power limits; i.e., they can be operated above their continuous-power limit for short periods of time. For example, Teplechuk et al. [117] designed and built an amplifier (which serves a similar purpose to a power converter) with a burst output power more than twice its continuous output power. Meanwhile, the aforementioned maximum power estimates for the monoplane and box wing only apply in hover, which lasts 20 seconds or less (see Table 22). By contrast, Table 55 and Table 56 show that the power-converter output

power in cruise is 4.75 kW for the monoplane (5.3 times lower than in hover) and 4.23 kW (5.4 times lower than in hover) for the box wing. Therefore, it may be possible to size the power-converter to the continuous (cruise) power requirement, rather than the peak (hover) power requirement. This should allow for further mass reductions.

It can be concluded from this section that a substantial increase in p_{HVPC} , relative to that of the V2 aircraft, is required in order for the vehicles in this study to be feasible. Significant improvements should be possible: given the above arguments, an order-of-magnitude improvement may be attainable. However, detailed power-converter design and experimental validation is required for confirmation. This is recommended as part of future work.

4.3.5 Battery specific power

4.3.5.1 Sensitivity

As discussed in Section 4.2.5, the battery specific power p_{battery} is equal to the maximum available output power of the battery, divided by its mass. A sensitivity analysis with respect to battery specific power is shown in Figure 51.

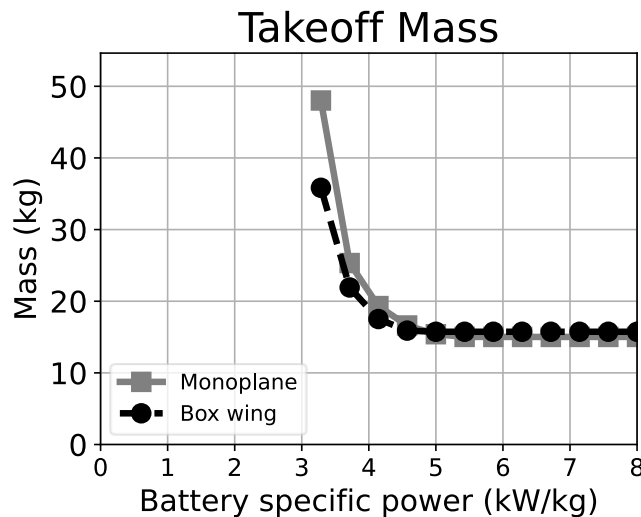


Figure 51: Vehicle takeoff mass vs. battery specific power.

4.3.5.2 Discussion

Figure 51 only shows data for $p_{\text{battery}} \gtrsim 3 \text{ kW/kg}$, because the optimizer does not converge for lower specific power values. Therefore, a battery specific power above approximately 3 kW/kg is required for the vehicles in this study to be feasible.

Recall from Section 4.2.5 that the battery is sized by three parameters: specific energy, specific power, and density. Figure 51 shows that vehicle mass is independent of battery specific power above 5 kW/kg. Therefore, the specific power constraint becomes inactive above this point; the battery is only sized by specific energy and density.

The default value of battery specific power in this study is 4 kW/kg (Table 25), about twice that of existing prototype lithium-ion batteries [68]. However, the specific power of lithium-polymer batteries in the literature can be as high as 3 kW/kg [118]. In addition, batteries can have burst (pulse) current limits that are higher than their continuous-current limits. The upper current limit is typically dependent on the battery module geometry. For example, a commercially available battery module [119] has a maximum pulse discharge current more than twice as high as its continuous discharge current. Furthermore, as discussed in Section 4.3.4.2, the continuous (cruise) power requirements for the aircraft in this study are more than five times lower than the peak (hover) requirements. Therefore, it may be possible to design a battery pack with the required specific power using existing technology.

4.4 Chapter conclusions

In this chapter, two uncrewed MSD-powered aircraft (a monoplane and a box wing) are designed and optimized for a nominal last-mile package delivery mission. These aircraft incorporate decoupled thrusters, with low-power ion sources and low-drag electrodes. Furthermore, the specific power of both the power converter and battery are higher than today's state-of-the-art systems. Both aircraft are capable of flying the nominal mission. However, this is contingent on advances in four key technologies, relative to today's state of the art. The technologies and their associated parameters are as follows:

- **More-efficient ion generation methods** with reduced power draw, quantified via the ionization energy E_{ion} .
- **Miniaturized thruster electrodes** with lower duct pressure losses, quantified via the stage loss coefficient K_L .
- **Lighter power converters** with greater output power, quantified via the power-converter specific power p_{HVPC} .
- **Lighter batteries** with greater output power, quantified via the battery specific power p_{battery} .

EAD aircraft for last-mile package delivery can be practical if the requisite improvements in thruster ion generation, electrode drag losses, and power-converter and battery specific power can be obtained. Put differently, an answer to the research question in Section 1.3, as can be determined from the vehicles designed in this chapter, is contingent upon the assumptions made for the four listed technologies. The identification of these technologies, as well as the associated parameter by which improvement can be quantified, is a key contribution of this chapter.

5 Design of aircraft with ducted EAD thrusters for surveillance

5.1 Background and overview

In this chapter, an MSD-powered aircraft is designed and optimized for a surveillance mission, in order to obtain a more complete answer to the research question posed in this thesis. Recall (Section 1.3) that this thesis' goal is to determine whether EAD propulsion for fixed-wing, heavier-than-air aircraft can be practical. This requires initial applications to be identified, from which mission parameters and design requirements can be obtained. Two candidate missions have thus far been identified: surveillance (Chapter 3) and package delivery (Chapter 4). The results in Chapter 4 show that the feasibility of EAD propulsion for package-delivery aircraft is contingent on improvements in four technological areas. However, the V3 from Chapter 3 would not have worked as designed due to lack of climb performance, so the results from the V3 flight test campaign are inconclusive. Therefore, whether EAD propulsion for a surveillance mission can be practical has not yet been determined.

This thesis chapter seeks to provide such a determination, by designing an MSD-powered aircraft for a surveillance mission. The design models and input parameters are mostly similar to those from the MSD package-delivery aircraft designed in Chapter 4. However, the mission requirements are based on a nominal surveillance mission, similar to that in Chapter 3. A climb requirement is added, based on the discussion of climb thrust requirements in Section 3.3.5.

The rest of this thesis chapter is structured as follows. The study methods, with a particular focus on differences with the methods used in Chapter 4, are presented in Section 5.2. Design results and sensitivity analyses are provided in Section 5.3, before the conclusions in Section 5.4.

The content in this chapter was prepared entirely by the author. However, design requirements and models borrow heavily from Chapters 3 and 4; collaborations and assistance in developing them are documented in Sections 3.1 and 4.1 respectively.

5.2 Methods

5.2.1 Mission requirements

Since the aircraft in this study is designed for a surveillance mission, requirements can largely be borrowed from those selected for the V3 (Section 3.2.1). They are as follows:

- **200 g camera payload.** This is the same as for the V3.
- **Payload dimensions of 20 cm × 10 cm × 10 cm** (length × width × height). This requirement ensures that surveillance payloads (regardless of size) can be carried internally in the fuselage pod. However, the exact values are somewhat arbitrary.
- **30 minutes of endurance.** This is a typical duration for a military drone reconnaissance mission (see Section 3.2.1).
- **Minimum climb rate of 0.51 m/s**, or 100 feet per minute. As discussed in Section 3.3.5, this is consistent with the FAA definition of service ceiling.

As in Sections 3.2.1 and 4.2.1, these requirements represent a threshold for practicality: if an EAD-powered aircraft can meet them, it is considered practical for the purpose of this thesis.

The mission profile includes three segments: climb, loiter, and bank. All three segments must be flown at a speed at least 20% greater than the stall speed. Requirements specific to each segment are summarized in Table 33.

Table 33: Mission profile for the MSD surveillance aircraft, showing the requirements for each mission segment.

Mission segment	Requirements
Climb	Minimum climb rate of 0.51 m/s.
Loiter	Steady level flight for 30 minutes.
Bank	180° turn; 30° bank angle.

Unlike the V3, a takeoff mission segment is not included. The results in Section 5.3.1 will show that the vehicle designed in this chapter has almost twice as much thrust available as is required for loiter. Therefore, the design is left agnostic to takeoff means: runway takeoff, catapult launch (as with the V3), and hand launch (as with the Raven) are all plausible options.

5.2.2 Vehicle architecture

One vehicle concept is developed in this chapter: a monoplane with a box-tail thruster. This design concept is hereafter referred to as the MSD surveillance monoplane, to distinguish it from the package-delivery monoplane developed in Chapter 4.

As with the package-delivery monoplane, the surveillance monoplane consists of a fuselage pod, monoplane wing, tail boom, and box tail, the latter of which doubles as an MSD thruster. To-scale sketches are generated using OpenVSP. An isometric view is shown in Figure 52; additional views are in Appendix T.

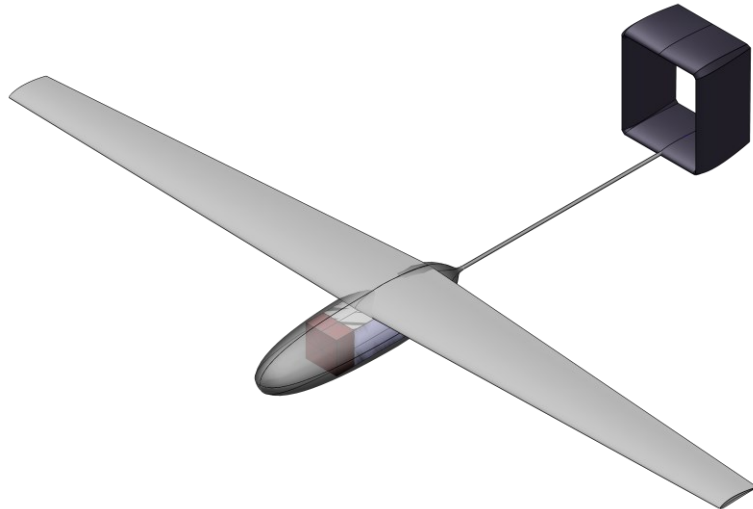


Figure 52: Isometric view of the surveillance monoplane.

The package-delivery vehicle concepts developed in Chapter 4 are not included in this study, because the surveillance mission in Section 5.2.1 does not include a hover segment. Therefore, the package-delivery monoplane's forward thrusters (whose purpose is to supply thrust forward of the CG to balance the aircraft in hover) would only add undesired mass and drag. The box wing aircraft is not included either, for similar reasons.

5.2.3 Multidisciplinary design optimization

As in Chapters 3 and 4, the design optimization framework used to generate the results in this chapter uses signomial programming. Takeoff mass (minimize) is the objective function. Optimization data, including number of free variables, constraints, and typical optimization solve times, is provided in Table 34.

Table 34: Number of free variables, number of constraints, and typical solve times on a laptop computer for design optimization of the MSD surveillance monoplane.

Free variables	864
Constraints	1762
Typical solve time	0.5 s

5.2.4 Thruster and power-electronics models

This study uses the same one-dimensional MSD thruster model described in Section 2.3.2 and used in Chapter 4. As in Chapter 4 (Section 4.2.5), the battery is sized using a fixed specific energy, specific power, and density, while the power converter is sized using a fixed specific power and efficiency. No upper limit on battery power draw is imposed. However, some of the input parameters used in this study are different from those in Chapter 4.

Input parameters are summarized in Table 35. Thruster parameters not included in Table 35 are identical to those in Chapter 4, and are given in Table 24.

Table 35: Thruster and power-electronics sizing parameters for the surveillance monoplane.

Parameter		Value
Thrusters	Ionization energy	66 eV
	Stage loss coefficient	1.0×10^{-2}
Battery	Specific energy	$200 \frac{\text{Wh}}{\text{kg}}$
	Specific power	$1 \frac{\text{kW}}{\text{kg}}$
	Density	$2.4 \frac{\text{kg}}{\text{L}}$
Power converter	Specific power	$2.06 \frac{\text{kW}}{\text{kg}}$
	Efficiency	85%

Table 35 shows that the thruster, battery, and power-converter models all assume fewer technological improvements, relative to those assumed by the MSD package-delivery aircraft study. For example, while the thruster ionization energy (66 eV) is identical to the default value used in Chapter 4, the stage loss coefficient (1.0×10^{-2}) is five times larger. Thrusters with this loss coefficient will therefore require fewer of the geometric design improvements discussed in Section 4.3.3.2. Similarly, the battery specific energy is unchanged from Chapter 4, but the specific power (1 kW/kg) is four times lower. These battery specifications are consistent with existing prototype lithium-ion batteries (Table 3). Finally, the power-converter efficiency (85%)

is unchanged from Chapter 4, but the specific power (2.06 kW/kg) is five times lower. This value is also twice as high as that of the V2 power converter (Table 4).

5.2.5 Aircraft mass, drag, and structural models

The aircraft mass, drag, and structural models, as well as input parameters, are generally identical to those used in Chapter 4. Key differences are as follows:

- **No thruster tilting mechanisms.** The MSD surveillance monoplane does not require VTOL, and so thruster tilting mechanisms are not required.
- **Limited wing airfoil thickness.** As with the V3 and unlike with the MSD package-delivery aircraft, a lower limit on wing thickness-to-chord ratio is included to avoid compromising wing maximum-lift performance. The limit used in this study is 10%.
- **Different airfoil drag fits.** As in Chapter 4, the profile drag of the wing and box tail (both airfoils) is modeled using a GP-compatible fit to airfoil data from Xfoil. However, the MSD surveillance monoplane has lower flight speeds, and correspondingly lower Reynolds numbers, relative to the MSD package-delivery aircraft. A different set of airfoil drag fits is used for this reason; RMS errors are therefore different.
- **Tail boom sizing loads.** The tail booms on the package-delivery aircraft in Chapter 4 are sized by a cantilever end load from tail thrust in hover. This sizing condition does not exist for the surveillance mission. Instead, the end loads in this chapter are computed as the quadratic sum of horizontal- and vertical-tail maximum lift, as in Chapter 3.

The exceptions above notwithstanding, aircraft-level sizing parameters are identical to those already summarized in Table 26, while component mass and structural models are identical to those summarized in Table 27. Details of the profile drag models for the wing and box tail (as discussed above) are provided in Table 36.

Table 36: Profile drag models specific to the MSD surveillance monoplane.

Component	Profile drag model
Monoplane wing	Fit to NACA 44XX airfoil data: $C_d = f\left(\frac{t}{c}, \text{Re}, C_L\right)$. Fit RMS error: 3.0%. 20% interference factor.
Box tail	Fit to NACA 00XX airfoil data: $C_d = f\left(\frac{t}{c}, \text{Re}\right)$. Fit RMS error: 3.2%. 10% interference factor.

5.3 Results

5.3.1 Design optimization results

A summary of the optimization results is provided in Table 37. An isometric view of the surveillance monoplane is provided in Section 5.2.2; additional views are provided in Appendix T. Detailed dimensional data, a mass breakdown, and detailed performance data are provided in Appendix U, Appendix V, and Appendix W respectively.

Table 37: Summary of the design optimization results for the MSD surveillance monoplane.

Length	1.38 m
Wingspan	3.03 m
Wing area	0.547 m ²
Takeoff (total) mass	4.18 kg
Payload mass	0.20 kg
Battery mass	1.35 kg
HVPC mass	0.43 kg
Empty mass fraction	0.53
Loiter speed	10.8 m/s
Loiter lift coefficient	1.04
Loiter drag coefficient	609.5 counts ^{\$\$\$}
Loiter lift-to-drag	17.1
Loiter thrust	2.40 N
Loiter battery power	0.54 kW
Loiter overall efficiency	4.9%
Endurance	30 minutes
Climb speed	10.8 m/s
Climb thrust	4.33 N
Climb battery power	1.05 kW

^{\$\$\$} Recall from Section 3.3.1 that counts reference the drag coefficient, multiplied by 10^4 .

Table 37 shows that the surveillance monoplane is smaller than the V3 biplane: its fuselage is shorter (1.38 m vs. 2.04 m) and its wingspan is smaller (3.03 m vs. 3.50 m). This is despite the fact that a wingspan constraint was added late in the V3 design process, to improve portability (Section 3.3.3). The surveillance monoplane lacks such a constraint. It may therefore be better able to meet the human-portability requirements useful for a surveillance mission, as discussed in Section 3.2.1.

Table 28 also shows that the thrust required to climb (4.33 N) is almost twice as high as the thrust required in loiter (2.40 N). This shows the importance of the climb requirement: excess thrust required to climb is significantly greater than that required in steady level flight, and must be taken into account during design.

Mass and loiter drag breakdowns are given in Figure 53 and Figure 54 respectively.

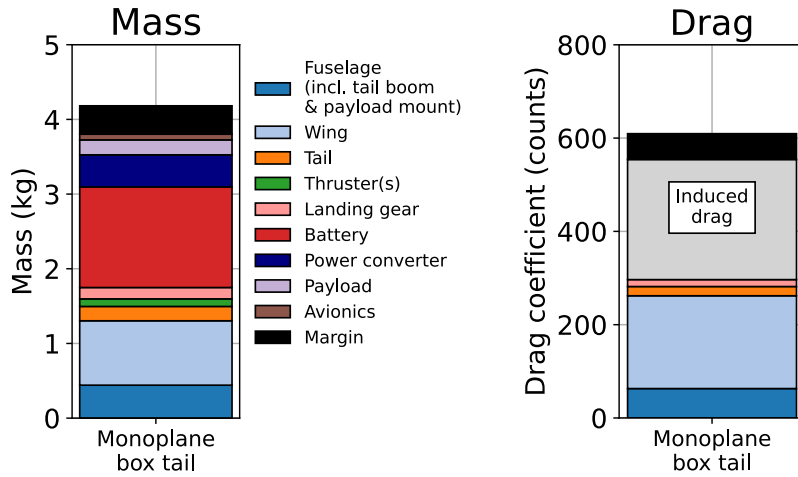


Figure 53: Mass breakdown for the MSD surveillance monoplane.

Figure 54: Loiter drag breakdown for the MSD surveillance monoplane.

Figure 53 shows that the battery accounts for the single largest fraction (32%) of the total mass; the wing (21%) and power converter (10%) also make significant contributions. Figure 54 shows that the single largest fraction (42%) of drag is induced drag. Profile drag from the wing (33%) and fuselage pod (10%) are also significant.

The optimizer generates a converged solution for the MSD surveillance monoplane, indicating that it can fly the nominal 30-minute loiter mission including a climb requirement. This result is compared with those for the V3 surveillance biplane and for the MSD package-delivery vehicles

in Sections 5.3.2 and 5.3.3 respectively. Convergence is sensitive to the choice of climb requirement, as well as to three of the four technological parameters identified in Chapter 4: ionization energy, stage loss coefficient, and power-converter specific power. All four parameters are discussed in detail in Sections 5.3.4 – 5.3.7.

5.3.2 Comparison with the V3 biplane

Table 37 shows that the surveillance monoplane endurance (30 minutes) is more than twice as high as the V3 design endurance (13.8 minutes). The reasons for this can be understood by applying the Breguet range equation to the endurance of an EAD-powered aircraft with a fixed thruster thrust-to-power. The result is

$$\text{Endurance} = \frac{\eta_{\text{hvpc}}}{g} e_{\text{battery}} f_{\text{battery}} \left(\frac{L}{D} \right) \left(\frac{T}{P} \right)_{\text{EAD}} \quad (76)$$

where η_{hvpc} is the power-converter efficiency, g is gravitational acceleration (9.81 m/s^2), e_{battery} is the battery specific energy, f_{battery} is the battery mass fraction (battery mass / vehicle mass), $\frac{L}{D}$ is the lift-to-drag ratio, and $\left(\frac{T}{P} \right)_{\text{EAD}}$ is the thruster thrust-to-power ratio (thrust / electrical power drawn by the EAD thrusters).

Equation (76) assumes that all of the battery energy is consumed in loiter. This is a reasonable approximation, since the surveillance vehicles in this thesis are not designed with reserve requirements. Instead, they spend virtually all of their time in loiter.

Design parameters in Equation (76) are provided for the V3 biplane and the MSD surveillance monoplane in Table 38.

Table 38: Design parameters in the Breguet range equation for the V3 biplane and the MSD surveillance monoplane.

	V3 biplane	MSD monoplane
Power-converter efficiency	85%	85%
Battery specific energy	115 Wh/kg	200 Wh/kg
Battery mass fraction	0.32	0.32
Loiter lift-to-drag	8.2	17.1
Loiter EAD thrust-to-power	8.9 N/kW	5.3 N/kW

Table 38 shows that a power-converter efficiency of 85% is used to design both the V3 and the MSD surveillance monoplane. By coincidence, the battery mass fractions are also identical at 32%. Therefore, the increased endurance of the MSD surveillance monoplane can be explained via the other three parameters, as follows.

The first parameter of interest is battery specific energy. The V3 specific energy is based on battery cell tests by the EAD team (Section 3.2.5). The MSD monoplane specific energy is almost twice as high, while still consistent with existing prototype lithium-ion batteries (Section 5.2.4). This factor explains much of the difference in endurance.

The second parameter of interest is lift-to-drag ratio: Table 38 shows that the MSD monoplane lift-to-drag ratio is more than twice as high as that of the V3. However, the resulting expected increase in endurance is mitigated by two factors:

- **Drag accounting.** Drag of the V3 exposed thrusters is included in drag, and therefore reduces its lift-to-drag ratio. However, the drag of the MSD thruster electrodes is modeled as a thrust loss instead of as a drag increase, and therefore reduces its thrust-to-power ratio rather than its lift-to-drag ratio.
- **Design constraints.** The V3 lift-to-drag ratio is penalized because of its biplane configuration, and because of the wingspan constraint^{****} of 3.5 m. For comparison, Table 17 shows that the monoplane with leading- and trailing-edge corona thrusters without a wingspan constraint has a lift-to-drag ratio of 16.0. This is almost twice as high as the V3, and almost as high as the MSD surveillance monoplane. This monoplane also has a predicted endurance of 38 minutes (greater than that of the MSD surveillance monoplane), although it does not meet the service-ceiling climb requirement.

The final parameter of interest is thrust-to-power ratio. The thrust-to-power ratio for the MSD surveillance monoplane is actually lower than that of the V3. This is in spite of the MSD thruster duct, which increases thrust-to-power relative to an equivalent unducted system (Section 2.3.3).

^{****} This optimization constraint was added late in the V3 design process for portability reasons (Section 3.3.2).

However, a comparison of the thrust-to-power ratio of these two vehicles is complicated by the following factors:

- **Different thruster models.** Recall from Section 3.2.4 that the V3 thruster model is fully empirical, and the effect of freestream velocity is not included. By contrast, the MSD thruster model includes Equations (10)-(12), which model velocity effects on overall MSD thruster performance via simple momentum theory. In addition, velocity effects on EAD pressure rise and current are included in the MSD thruster model via Equations (18) and (20) respectively. Since EAD thrust-to-power is known to decrease with increasing freestream velocity [22], [23], this effect complicates a direct comparison.
- **Different design points.** The MSD surveillance monoplane has a higher design loiter speed than the V3: 10.8 m/s vs. 6.8 m/s. The resulting higher dynamic pressure should decrease thrust-to-power due to increased electrode drag.

A comparison of thrust-to-power ratio between aircraft must account for these factors.

The MSD surveillance monoplane thrusters use a gap spacings of 10 mm (Table 24), while the V3 thrusters have gap spacings ranging from 105-117 mm (Table 19), an order of magnitude larger. The results in Section 2.2.3 show that greater gap spacings result in improved thruster performance, but this result only holds for a fixed thruster span. If thrust per unit cross-sectional area is used as a metric, the V3 aircraft is penalized by the effects of electrode array size also discussed in Section 2.2.3: a larger gap spacing means a larger thruster. By contrast, MSD thrusters can take advantage of miniaturized low-loss electrodes, made possible by structural support from the thruster duct (Section 2.3.1). Furthermore, a smaller gap spacing allows for a lower power-converter output voltage, as discussed in Section 4.3.4.2.

5.3.3 Comparison with the MSD package-delivery aircraft

Although the design models are similar, the MSD surveillance monoplane is designed to a different set of mission requirements than the MSD package-delivery aircraft. Input sizing parameters are also different. Requirements and parameters that differ between the two studies are summarized in Table 39.

Table 39: Summary of mission requirements and input parameters that differ between the MSD surveillance and MSD package-delivery vehicles.

	MSD surveillance	MSD package delivery
Payload mass	200 g	1.2 kg
Minimum climb rate	0.51 m/s	1.52 m/s
VTOL requirement?	No	Yes
Ionization energy	66 eV	66 eV
Stage loss coefficient	1.0×10^{-2}	2.0×10^{-3}
HVPC specific power	2.06 kW/kg	10.3 kW/kg
Battery specific power	1 kW/kg	4 kW/kg

Table 39 shows that the MSD surveillance mission is not as demanding as the MSD package delivery mission: the payload mass is lower (200 g vs. 1.2 kg), the required climb rate is lower (0.51 m/s vs. 1.52 m/s), and vertical takeoff and landing is not required. For this reason, the MSD surveillance monoplane optimization problem converges with fewer technological improvements, relative to those required for the MSD package-delivery vehicles.

For example, while ionization energy is identical between the two studies, the stage loss coefficient used to design the MSD surveillance monoplane (1.0×10^{-2}) is five times higher than that used to design the MSD package delivery vehicles. It should be possible to design thrusters with this loss coefficient without as many of the geometric improvements discussed in Section 4.3.3.2. A similar argument can be made for the MSD surveillance monoplane power converter: its specific power is five times lower than the specific power used to design the MSD package delivery vehicles. The required improvement in specific power, relative to the V2 power converter, is therefore only a factor of 2, rather than a factor of 10. Finally, the MSD surveillance monoplane's battery specific power of 1 kW/kg is consistent with existing battery technology (Table 3). By contrast, the MSD package-delivery vehicles' battery specific power is four times higher, and may require sizing to battery burst (pulse) current limits rather than to continuous-current limits (Section 4.3.5.2).

5.3.4 Climb requirements

The results in Section 3.3.5 show that the driving requirement for EAD fixed-wing flight is climb rate. Therefore, a sensitivity analysis with respect to required climb rate (the independent variable)

is conducted. Results are shown in Figure 55; the service-ceiling climb requirement is shown for comparison.

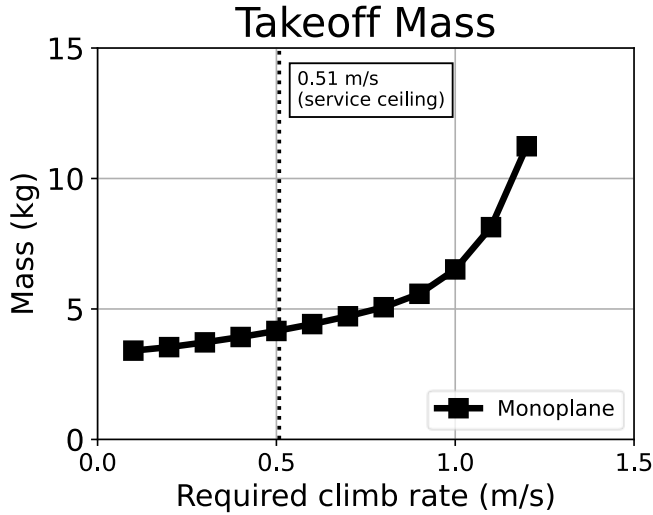


Figure 55: Takeoff mass vs. required climb rate for the MSD surveillance monoplane.

Figure 55 shows that takeoff mass increases with required climb rate. Furthermore, Figure 55 only shows data for $v_v \lesssim 1.2$ m/s. This is because the optimizer does not converge for higher climb rates. Therefore, the MSD surveillance monoplane is capable of meeting the calm-dawn and calm-day certification requirements (0.1 m/s and 0.3 m/s respectively). It can also meet the service-ceiling climb requirement (0.51 m/s, the default value used in this chapter). However, the old Part 23 certification requirement (1.52 m/s) cannot be met under the current study assumptions. In order to meet this requirement, some combination of improvements in stage loss coefficient and power-converter specific power may be needed.

For comparison, the MSD package-delivery vehicles are designed to the old Part 23 certification climb requirement. They can meet it in part because their design incorporates more technological improvements (Section 5.3.3). In addition, the thrust required for VTOL is greater than the vehicles' weight; this thrust is more than sufficient to meet a climb requirement.

5.3.5 Ionization energy

A sensitivity analysis is conducted with respect to ionization energy. Results are in Figure 56.

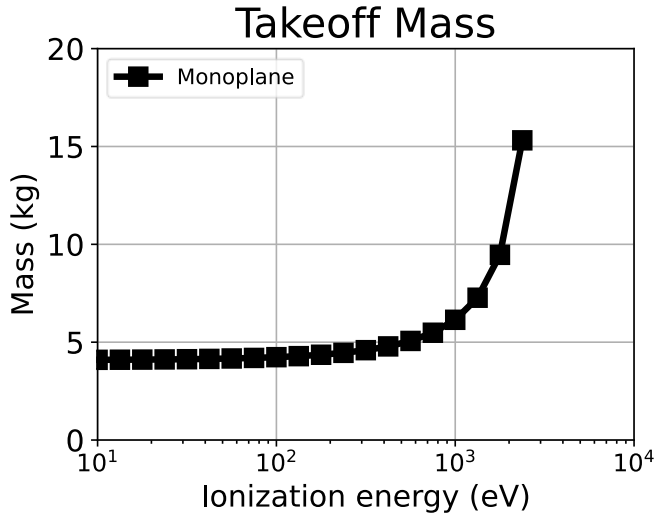


Figure 56: Takeoff mass vs. ionization energy for the MSD surveillance monoplane.

Figure 56 only shows data for $E_{\text{ion}} \lesssim 2,000$ eV, because the optimizer does not converge for higher ionization energies. For comparison, the MSD package-delivery vehicles require a thruster ionization energy below approximately 1,000 eV.

5.3.6 Stage loss coefficient

A sensitivity analysis is conducted with respect to stage loss coefficient. Results are in Figure 57.

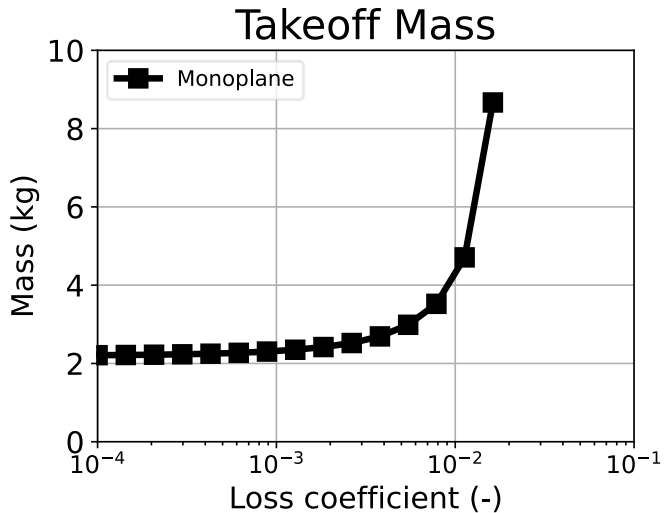


Figure 57: Takeoff mass vs. stage loss coefficient for the MSD surveillance monoplane.

Figure 57 only shows data for $K_L \lesssim 2 \times 10^{-2}$. This is because the optimizer does not converge for loss coefficients higher than this. Therefore, K_L must be less than approximately 2×10^{-2} in order

for the vehicles in this study to be feasible. For comparison, the MSD package-delivery vehicles require a stage loss coefficient below approximately 4×10^{-3} , i.e., five times lower.

5.3.7 Power-converter specific power

A sensitivity analysis with respect to power-converter specific power is shown in Figure 58. Each point on the plot represents an optimized vehicle design; power-converter specific power is the only input parameter that is varied.

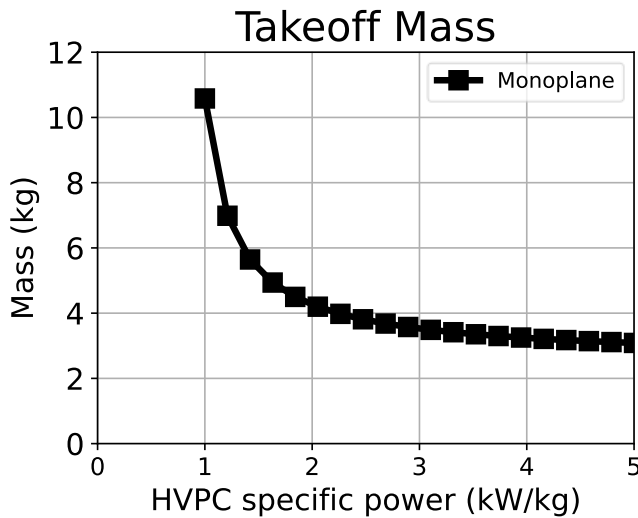


Figure 58: Takeoff mass vs. power-converter specific power for the MSD surveillance monoplane.

Figure 58 only shows data for $p_{\text{HVPC}} \gtrsim 1 \text{ kW/kg}$. Therefore, a power-converter specific power above approximately 1 kW/kg is required for the vehicles in this study to be feasible. This specific power is almost identical to that achieved by the V2 power converter: 1.03 kW/kg (Table 4). For comparison, the MSD package-delivery vehicles require a power-converter specific power above approximately 7 kW/kg, about seven times higher. In comparing these vehicles' power converters, the input parameters discussed in Section 4.3.4.2 (input & output voltage, output power, and burst power) must be carefully considered.

5.3.8 Battery specific power

A sensitivity analysis with respect to battery specific power is shown in Figure 59.

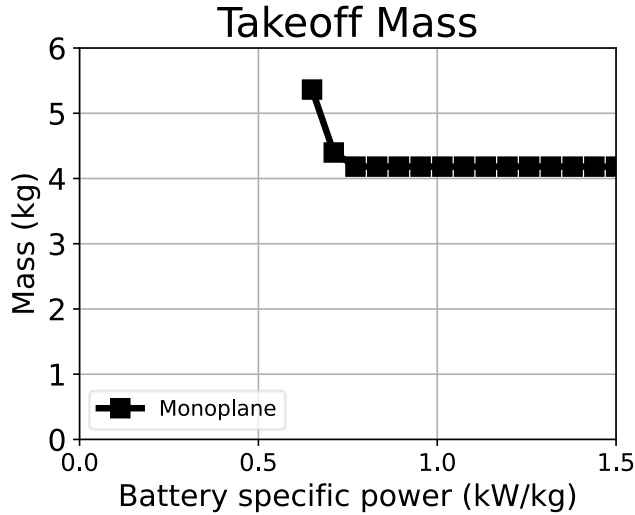


Figure 59: Takeoff mass vs. battery specific power for the MSD surveillance monoplane.

Figure 59 only shows data for $p_{\text{battery}} \gtrsim 0.7 \text{ kW/kg}$, so a battery specific power greater than approximately 0.7 kW/kg is required for the vehicles in this study to be feasible. Figure 59 also shows that vehicle mass is independent of battery specific power above 0.8 kW/kg. The specific power optimization constraint is inactive above this value; the battery is only sized by specific energy and density.

The default value of battery specific power in this study is 1 kW/kg, consistent with existing batteries (Table 3). For comparison, the MSD package-delivery vehicles require a battery specific power above approximately 4 kW/kg, about four times higher. This may require an advanced battery-pack design (Section 4.3.5.2).

5.4 Chapter conclusions

In this chapter, an uncrewed MSD-powered aircraft (a monoplane) is designed and optimized for a nominal surveillance mission. A service-ceiling climb rate requirement of 0.51 m/s is imposed. Design optimization results are compared with those of the V3 and the MSD package-delivery aircraft. Sensitivities to the four technological parameters identified in Chapter 4, as well as to the climb-rate requirement, are estimated.

This chapter shows that the requirements for a nominal surveillance mission are less demanding than those for a package delivery mission. However, as in Chapter 4, whether MSD-powered surveillance aircraft can be practical depends upon the technological assumptions: they can be practical if the requisite improvements in thruster ion generation, electrode drag losses, and power-converter specific power are obtained. Fewer improvements are required, relative to those required to fly the package delivery mission. In particular, the surveillance mission can be completed by an MSD-powered aircraft with an electrode stage loss coefficient five times higher, with a power-converter specific power five times lower, and with a battery specific power four times lower, relative to what is required to complete the package-delivery mission. The battery specific power required for surveillance is consistent with existing technology, but the battery specific power required for package delivery is not. These technologies and parameters are previously identified in Chapter 4, but the extent to which improvements are required to fly a surveillance mission is a key contribution of this chapter.

6 Future work

6.1 Additional mission requirements

The discussion of mission requirements in this thesis can be extended in at least three ways. Firstly, surveillance mission requirements are based on a military surveillance UAV (the Raven). Another class of surveillance mission should be considered: wildlife surveillance [120], [121]. In this application, the goal is to observe animals without making noise that would disrupt the animals' natural behavior. Requirements for this mission, with a particular emphasis on how they differ from those for military surveillance, should be considered.

Secondly, it is assumed in Chapter 5 that a service-ceiling climb rate of 0.51 m/s is sufficient to be considered practical. This assumption may be problematic, because a certification basis for UAVs has not yet been defined by the FAA. In the absence of such a certification basis, it may be advisable to impose a climb requirement based on physics or operational data. For example, a climb rate requirement may be obtained by analyzing atmospheric data to determine downdraft strengths. The climb rate requirement must then be greater than the strongest downdraft encountered, so that a downdraft will not force the aircraft to descend (Section 3.3.5). An analogous situation was encountered by Burton & Hoburg [81] when designing a solar-electric aircraft. Their aircraft must fly at least as fast as the wind, in order to loiter over a fixed location. Therefore, their minimum loiter speed requirements were based on wind speeds obtained from atmospheric data.

Finally, vehicle reserve requirements are not considered in this thesis, because a reserve requirement for UAVs has not yet been defined by the FAA. However, reserve requirements are included in the certification basis for crewed aircraft, and should be considered for operational reasons. It may be worth obtaining candidate reserve requirements, then analyzing the sensitivity by designing a vehicle to each requirement. A similar analysis was conducted by the author for urban air taxis, for which the certification basis was also unclear at the time of the study [82].

6.2 MSD thruster development

The results in Chapters 4 and 5 show that improvements in both thruster ionization energy and stage loss coefficient (relative to the current state of the art) are required by these chapters' vehicles. However, the estimates for attainable improvements in both parameters are subject to uncertainty. For example, none of the alternate ion sources listed in Table 31 and discussed in Section 4.3.2.2 have been demonstrated experimentally for EAD propulsion (although they have been demonstrated in other applications). Similarly, the advanced electrode geometry depicted in Figure 47 and discussed in Section 4.3.4.2 has not been built or demonstrated experimentally.

MSD thrusters that incorporate decoupled ion sources and low-loss electrodes should therefore be designed, manufactured, and experimentally demonstrated. In addition, the one-dimensional thruster model developed in Section 2.3.2 have been validated for corona thrusters with up to 10 stages [64], but the vehicles in this thesis use decoupled thrusters with more than 20 stages. Model validation should therefore be extended to decoupled thrusters and higher stage counts.

6.3 Power electronics modeling and development

The power converters in this thesis are sized using a fixed specific power and efficiency. The results in Chapters 4 and 5 show that improvements in specific power are necessary, relative to the current state of the art. However, in the absence of experimental demonstration, uncertainty in the achievable improvements remains.

A power-converter design model with a higher level of fidelity should also be developed. Such a model would reduce the uncertainty in achievable specific power; it would also reveal additional issues and offer benefits. An example issue is power-converter efficiency, which is fixed at 85% in this thesis. However, power-converter efficiency is in general a function of power draw. Bench testing revealed that the V2 power converter was 85% efficient at a power draw of 600 W [10], close to the 620 W achieved in flight (Table 1). However, its efficiency dropped to 81% when the output power was reduced by half, to 300 W. This may be an issue for the MSD-powered vehicles in this thesis, since these vehicles' cruise power draw is substantially lower than peak power draw (Table 30 and Table 37). Power-converter efficiency may therefore also be lower.

A power-converter model with higher fidelity may also reveal design benefits. For example, it is argued in Section 4.3.4 that a power converter with greater specific power (relative to the V2) should be possible for the MSD aircraft designed in that chapter. This is due to higher input voltage, lower output voltage, and higher output power draw, as shown by the mass dependencies in Equation (35). A power-converter model that incorporates component models for the inverter, transformer and rectifier, as well as a parameterization that includes input and output voltage, should allow for this benefit to be quantified.

A battery model with higher fidelity may also be useful. For example, by explicitly modeling number of cells and cell voltage, and linking the resulting battery output voltage to the power-converter model, a better estimate for mass savings due to an increased power-converter input voltage (Section 4.3.4) can be obtained. In addition, a battery model that includes packaging and thermal protection system mass, as well as state-of-charge margins, should be considered.

Two additional issues specific to the power-electronics system are apparent: throttle control and thermal management. The MSD vehicles designed in this thesis vary their thrust in different mission segments by controlling the stage DC voltage. This was not required on the V2, since its thrusters operated at a fixed voltage. A power-electronics system that can be throttled in flight may increase mass and design complexity, and has yet to be designed. In addition, larger batteries and power converters (relative to the V2) will generate excess heat, due to the power-converter efficiency of less than unity. The resulting thermal management problem is more significant for larger EAD aircraft than smaller ones, due to the square-cube law: as vehicle size increases, its internal volume (and with it, electrical power and waste heat) increases more quickly than the surface area available for cooling. Thermal management is also expected to be more of an issue in hovering flight than in wingborne flight, for two reasons: power draw is greater, and convective cooling is less effective due to the lack of a freestream velocity component. For similar reasons, thermal management is an emerging issue for electric aircraft [65].

6.4 Airframe prototyping and flight testing

Several design assumptions made in Chapters 4 and 5 can only be validated via airframe prototyping, experimental testing, and flight testing. A few examples are provided here. Firstly, the vehicles designed in these chapters are built largely of Kevlar, due to its electrical insulation

properties. Whether this design decision provides sufficient insulation for the EAD systems on a practical EAD aircraft must be demonstrated in practice. Secondly, electromagnetic interference between the EAD thrusters and the rest of the onboard electronics (especially the radio) is a concern; mitigation strategies must be demonstrated. Thirdly, it is assumed in this thesis that lift and induced drag of the box wing and box tails are both independent of thrust (Appendix O); electroaerodynamic interference between thrusters and lifting surfaces is neglected. However, research into the blown lift of electric aircraft with wing leading-edge propellers reveals the complexity of such coupled systems [84], [122]–[126]. A more sophisticated model for electroaerodynamic interference may be developed via wind-tunnel experimental testing.

Three additional potential issues are specific to the VTOL aircraft in Chapter 4. The first is the hover thrust-to-weight ratio. A value of 1.1 is assumed in this thesis, to account for control margins and suckdown effects. These effects, as well as recirculation (not considered here, but discussed further in Ref. [62]) should be assessed via computations and/or experiments. Control laws for hover and transition (between hover and wingborne flight) must also be developed. Finally, the mass of the thruster tilting mechanisms (estimated as 25% of the thruster + nacelle mass) is subject to uncertainty; a better estimate should be obtained via detailed design and prototyping. For example, it may be more appropriate to size the tilting mechanisms relative to thrust (since their loads should scale with thrust), rather than relative to thruster mass. Electrical power draw of the tilting mechanisms during transition is not included in Chapter 4, and should also be considered.

6.5 Acoustic characterization

As mentioned in Section 1.1, the main hypothesized advantage of EAD propulsion for aircraft (relative to propellers) is reduced noise, due to the lack of moving parts. However, aside from limited acoustic experiments documented in Ref. [5], the acoustic signature of an EAD aircraft has not been characterized in detail.

The noise signature of an EAD aircraft may consist primarily of one of four components: airframe noise, thruster noise, cylinder noise, and ionization noise. Airframe noise is caused by turbulence over the airframe; it is approximately proportional of aircraft flight velocity to the sixth power [127]. Semi-empirical methods for airframe noise prediction are developed in Refs. [128]–[130]. Thruster noise refers to the noise generated via turbulent mixing of the EAD thruster jet with the

surrounding air, analogous to jet noise from an engine. Jet noise at low Mach numbers scales with the eighth power of jet velocity [127]. Cylinder noise is produced in the Karman vortex street behind cylindrical emitter wires. This form of noise is known as an Aeolian tone; it can be characterized using the methods in Ref. [131].

The final listed source of noise may be encountered as a byproduct of some types of ion generation. For example, a high-pitched noise can sometimes be heard during experiments with DBDs. Existing literature on the acoustic properties of DBD actuators for flow control [132] suggests that the sound is generated as a by-product of the actuator transferring momentum into the air. This is as opposed to the sound being mechanical in origin (ex. from vibration of the DBD wires). Furthermore, the sound occurs at the same AC frequency as the DBD power supply. This noise source has yet to be characterized in detail. However, ionization noise may not necessarily be encountered for ion sources other than DBDs. Reverse emission may also generate noise [21].

Future work should characterize the acoustic signature of an EAD aircraft. Research should include determining which noise sources (airframe, thruster jet, cylinder, and ionization) dominate the signature. Noise models should be developed and validated with experiments, and an assessment of the implications for EAD aircraft design should be provided.

6.6 Environmental effects

The performance of EAD aircraft may be affected by environmental conditions. For example, as mentioned in Section 1.4, EAD thruster performance is sensitive to air pressure and humidity. This dependence can be modeled via the thruster ion mobility [53], [54]. Standard atmospheric properties are assumed throughout this thesis, and air pressure and humidity effects are not included. In addition, thruster performance may be sensitive to the presence of dust, rain, or snow. These issues are beyond the scope of the thesis, but they should be considered in future work.

EAD-powered aircraft may also impact the environment in potentially harmful ways. For example, DC corona discharges produce ozone gas as a by-product [49]; dielectric barrier discharges also generate ozone [133]. Ozone is considered a pollutant at ground level, due to its harmful effects on the human respiratory and cardiovascular systems [134]. These effects must be quantified and mitigated in order to responsibly deploy EAD-powered aircraft.

6.7 Unsteady effects

Unsteady effects are not included in this thesis, but three effects may be relevant. Firstly, the MSD package-delivery vehicles must transition between hover and wingborne flight. The flow around an aircraft in transition may be both separated and unsteady, complicating control-law development (mentioned in Section 6.4). Secondly, DBD ion sources require AC power supplies, which typically operate at frequencies from 5-20 kHz [19]: by definition, these sources are unsteady. Since DBD ion sources are also used for flow control [34]–[36], unsteady effects on the flow may be encountered. The same may be true for nanosecond repetitively pulsed (NRP) ion sources, although a steady-state approximation may be more appropriate for NRPs due to the higher frequencies at which they operate (relative to DBDs). Unsteady effects from ion sources may be of particular concern for electrode designs in which the ion source is integrated with the emitter and/or collector, as in Figure 47.

The third unsteady effect concerns the flow behind the emitter wires. Emitter wire drag in this thesis is estimated using cylinder drag data from Schlichting & Gersten [135], as documented in Appendix F. This data assumes steady-state flow. However, for cylinders above a critical Reynolds number, the flow behind a circular cylinder becomes periodic (i.e., unsteady), a phenomenon known as a Karman vortex street [135]. In an unducted EAD thruster, vortex streets generated by emitter wires may impinge on and interfere with the collectors downstream. Similarly, vortex streets behind MSD thruster emitters may impinge on the downstream emitters and collectors, increasing stage losses.

The onset of a Karman vortex street can be predicted as a function of the local cylinder Reynolds number $Re_{cylinder}$. Three regimes are identified, based on the data in Table 1.1 of Ref. [135]:

- If $Re_{cylinder} \lesssim 30\text{-}40$, the flow is steady. A Karman vortex street is not encountered.
- If $30\text{-}40 \lesssim Re_{cylinder} \lesssim 80\text{-}90$, the flow behind the cylinder is unstable. The onset of a Karman vortex street occurs at these Reynolds numbers.
- If $80\text{-}90 \lesssim Re_{cylinder} \lesssim 150\text{-}300$, the flow behind the cylinder forms a pure vortex street.

Emitter wire Reynolds numbers are provided in Table 40 for the vehicles designed in this thesis. Flow regimes (i.e., whether a vortex street occurs) are also identified. Data is provided as a function

of flight condition, thruster (since most vehicles have more than one type of thruster), and emitter wire diameter (since reduced wire diameters are investigated for the package-delivery vehicles in Section 4.3.3.2). The Reynolds number is computed using Equation (94), which includes the local flow velocity v . v for the V3 includes ionic-wind effects, as described in Appendix E. v for the MSD vehicles is equal to the thruster bulk velocity v_2 , as in Section 4.3.3.2.

Table 40: Emitter wire local Reynolds numbers and associated flow regimes.

Vehicle	Flight condition	Thruster	Wire diameter	Reynolds number	Vortex street?
V3	Loiter	Positive exposed DC corona thruster	127 microns	60.8	Onset
		Negative exposed DC corona thruster	127 microns	61.1	Onset
		Leading- & trailing-edge DC corona thruster	127 microns	59.3	Onset
Package-delivery monoplane	Cruise	Box-tail MSD thruster	56 microns	102.7	Pure
			7.6 microns	13.9	No (steady)
		Forward MSD thrusters	56 microns	102.3	Pure
			7.6 microns	13.9	No (steady)
	Hover	Box-tail MSD thruster	56 microns	68.9	Onset
			7.6 microns	9.3	No (steady)
		Forward thrusters	56 microns	66.8	Onset
			7.6 microns	9.1	No (steady)
Package-delivery box wing	Cruise	Box-tail MSD thruster	56 microns	100.8	Pure
			7.6 microns	13.7	No (steady)
		Box-wing MSD thruster	56 microns	100.8	Pure
			7.6 microns	13.7	No (steady)
	Hover	Box-tail MSD thruster	56 microns	59.1	Onset
			7.6 microns	8.0	No (steady)
		Box-wing MSD thruster	56 microns	62.0	Onset
			7.6 microns	8.4	No (steady)
Surveillance monoplane	Loiter	Box-tail MSD thruster	56 microns	51.7	Onset
	Climb	Box-tail MSD thruster	56 microns	57.5	Onset

Table 40 shows that thrusters with reduced wire diameters (7.6 microns) do not produce vortex streets. However, the remaining cases are either in the onset regime or the pure regime; a vortex street may be encountered. These effects should be considered in future work.

7 Conclusions

Electroaerodynamic (EAD) propulsion is a novel means of generating thrust without any moving parts. EAD thrusters work by using high voltages to accelerate ions, which then create thrust through collisions with neutral air molecules. EAD thrusters have no moving parts, and are therefore almost silent. EAD propulsion may therefore be useful for aircraft propulsion in applications where silence is valuable, such as for surveillance or last-mile package delivery.

A fixed-wing, heavier-than-air, EAD-powered aircraft (the V2) has previously achieved steady level flight, demonstrating that EAD for fixed-wing, heavier-than-air aircraft propulsion is feasible. The primary goal of this thesis is to determine whether EAD propulsion is practical. A practical aircraft is defined in this thesis as one with sufficient payload capacity, range and/or endurance, and flight performance to be of interest in some initial application.

EAD propulsion systems, including thrusters, batteries, and power converters, are characterized to a level of detail suitable for aircraft design in Chapter 2. The performance of exposed EAD thrusters can be improved, relative to those that powered the V2, by increasing the gap spacing and applied DC voltage. The achievable benefits are limited by electrode array size, non-ideal effects, and voltage limitations. Multistaged ducted (MSD) EAD thrusters are more powerful and efficient than exposed thrusters, in part because the duct contributes to thrust. These benefits are offset by the increased mass and drag of the duct. Finally, the battery pack and power converter on the V2 are compared with the state-of-the-art; sizing models for both components are developed.

Chapter 3 describes the V3, a third-generation EAD-powered airframe developed by the author in collaboration with a team of graduate and undergraduate students. The V3 is designed for a nominal surveillance mission, because low noise may be beneficial in this application. Requirements are based on the Raven, an existing fixed-wing military surveillance UAV. An efficient multidisciplinary optimization framework, utilizing signomial programming, is developed to design and optimize the V3. The framework incorporates empirical models for thruster performance, along with aerodynamic, structural, weight, and power-electronics models. A biplane configuration is identified via a trade study as the best option for the V3, in part because

of a tradeoff between endurance and portability requirements. The V3 is predicted to have an endurance almost an order of magnitude greater than the V2; these benefits are obtained partly because it incorporates multistaged surface-integrated (MSI) thrusters with increased gap spacing and voltage, and partly because of increased battery specific energy.

Flight testing of the V3 with a substitute propulsion system reveals that excess thrust for climb is the driving requirement for this class of aircraft: a practical EAD aircraft requires more thrust than a feasible one, in order to climb. The V3 architecture as developed is incapable of meeting a service-ceiling climb rate requirement. Therefore, answering the research question (can a practical EAD-powered aircraft be designed and built) requires that climb performance be included in the definition of sufficient flight performance to be considered practical.

In Chapter 4, two uncrewed aircraft concepts (a monoplane and a box wing), powered by MSD thrusters, are designed for a nominal last-mile package delivery mission. As with the surveillance mission, low noise may be beneficial in this application. Decoupled thrusters, with low-power ion sources and low-drag electrodes, are used, along with high-specific-power batteries and power converters. Requirements are based on last-mile drone package delivery services under development, and include vertical takeoff and landing. As in Chapter 3, the vehicles are designed using a custom multidisciplinary optimization framework, utilizing signomial programming. The framework includes a one-dimensional physics-based model for MSD thrusters, along with aerodynamic, structural, weight, and power-electronics models. Lessons from the V3 design and flight testing are incorporated.

Both the monoplane and the box wing are capable of flying the nominal package delivery mission. However, this result is contingent on improvements in four technological areas, relative to the state of the art. Specifically, the aircraft require: efficient ion generation methods with reduced power draw, quantified via the ionization energy; miniaturized thruster electrodes with lower duct pressure losses, quantified via the stage loss coefficient; lighter power converters with greater output power, quantified via the power-converter specific power; and lighter batteries with greater output power, quantified via the battery specific power. Therefore, referencing the research question, EAD aircraft for last-mile package delivery can be practical if the requisite technological improvements can be obtained. Plausible development paths are identified and discussed for all

four technologies. The technologies' identification, as well as the associated parameter by which improvement can be quantified, is a key contribution of this thesis.

In Chapter 5, another uncrewed aircraft concept (a monoplane) powered by MSD thrusters is designed for a nominal surveillance mission. The goal is to determine whether EAD propulsion for a surveillance mission can be practical, a question left unanswered in Chapter 3. A service-ceiling climb rate requirement is included, based on the lessons learned from V3 flight testing. The surveillance monoplane is designed using a design optimization framework incorporating most of the models and parameter assumptions as the framework developed in Chapter 4.

The MSD monoplane is capable of flying the nominal surveillance mission, including a climb requirement. This result is contingent on fewer technological improvements than are required for the package delivery mission. Specifically, the surveillance mission can be flown using thruster electrodes with higher drag losses, and with a power converter with lower specific power, compared to those required for the aircraft designed in Chapter 4. Furthermore, unlike for the package delivery mission, no improvements in battery specific power (relative to the state of the art) are required. It should therefore be easier to design an EAD-powered aircraft for a surveillance mission than for a package delivery mission.

A summary of design data for the vehicles designed in this thesis is provided in Table 41. The V2 is also shown for comparison. The V3 and the MSD surveillance monoplane are designed for a loiter mission, so data from their loiter mission segments is labeled as cruise data. The V3 max thrust and power draw are encountered during takeoff, the MSD package-delivery vehicles' max thrust and power draw are encountered during hover, and the MSD surveillance monoplane max thrust and power draw are encountered during climb. As before, efficiency is defined as the product of thrust and flight speed, divided by battery power draw.

Table 41: Data summary for the EAD aircraft designed in this thesis, as well as for the V2.

Aircraft	V2	V3	Package-delivery monoplane	Package-delivery box wing	Surveillance monoplane
Thruster type	Unducted	Unducted	Ducted	Ducted	Ducted
Ion source	DC corona	DC corona	Decoupled	Decoupled	Decoupled
Length	2.0 m	2.0 m	1.6 m	1.5 m	1.4 m
Wingspan	5.1 m	3.5 m	2.2 m	1.6 m	3.0 m
Takeoff mass	2.45 kg	3.04 kg	20.8 kg	18.6 kg	4.18 kg
Cruise speed	4.8 m/s	6.8 m/s	25.5 m/s	25.2 m/s	10.8 m/s
Cruise thrust	3.2 N	3.6 N	19.9 N	18.3 N	2.4 N
Cruise battery power draw	620 W	477 W	5.6 kW	5.0 kW	540 W
Cruise efficiency	2.5%	5.2%	9.1%	9.3%	4.9%
Max thrust	3.2 N	3.8 N	224.0 N	200.4 N	4.3 N
Max battery power draw	620 W	515 W	29.9 kW	26.8 kW	1.05 kW
Endurance	90 s	13.8 min	-	-	30 min
Mission radius	-	-	10 km	10 km	-

Can a practical EAD-powered fixed-wing aircraft be designed and built? The answer depends on the application of interest. If the application is a surveillance mission, a practical EAD aircraft can be built if improvements in ion generation, electrode duct pressure losses, and power-converter specific power can be obtained. If the initial application is a last-mile package delivery mission, additional improvements in electrode duct pressure losses and power-converter specific power are required, relative to the surveillance mission. Improved battery specific power is required as well, unlike for the surveillance mission. Plausible implementation paths to obtaining the requisite improvements in all four areas exist.

The contributions of this thesis can be summarized as follows. Firstly, mission requirements for two prospective initial applications of EAD aircraft propulsion (surveillance and last-mile package delivery) are identified. The requirements for a surveillance mission must consider climb performance. The second contribution concerns information on how to design EAD-powered aircraft. They can be designed via efficient multidisciplinary optimization frameworks, empirical

and physics-based thruster performance models, and aerodynamic, structural, weight, and power-electronics models. The third contribution is an assessment of the technological improvements required for EAD aircraft propulsion to be practical. Four technological improvement areas (thruster ionization energy, duct pressure losses, power-converter specific power, and battery specific power) are identified and parameterized. The extent to which improvements in each area are required is determined, and plausible development paths are identified.

Future work should focus on experimentally demonstrating the technological improvements identified in this thesis as required by a practical EAD aircraft. This will enable the design, development, and flight testing of a practical fixed-wing, heavier-than-air, EAD-powered aircraft.

Appendix A Exposed thruster experimental data

Thrust-to-power vs. thrust data for single-stage exposed thrusters is shown in Figure 60 – Figure 62. This data is used to develop the V3 thruster performance model fits (Section 3.2.4), results from which are also shown.

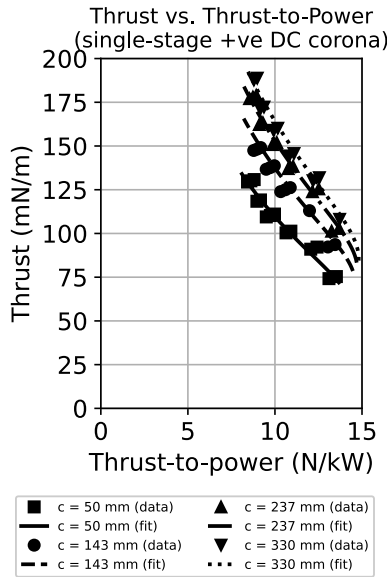


Figure 60: Thrust vs. thrust-to-power for a single-stage DC corona thruster with positive polarity.

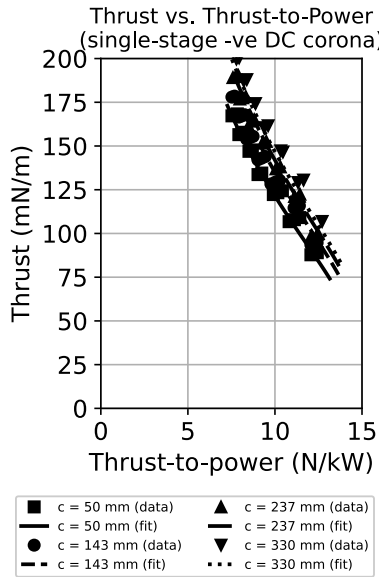


Figure 61: Thrust vs. thrust-to-power for a single-stage DC corona thruster with negative polarity.

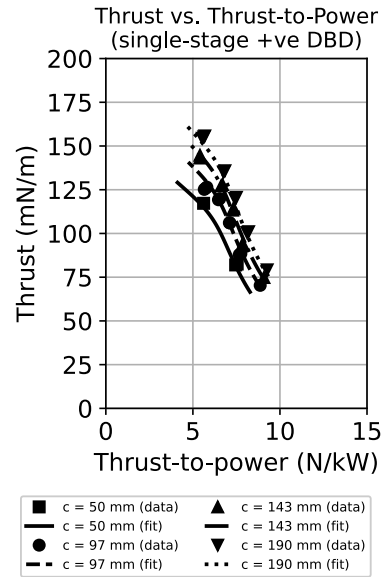


Figure 62: Thrust vs. thrust-to-power for a single-stage DBD thruster with positive polarity.

Figure 60, Figure 61, and Figure 62 all show that thruster performance improves with increased collector chord. This is hypothesized to be caused by a reduction in reverse emission due to larger collector airfoil leading-edge radii.

Figure 60, Figure 61, and Figure 62 show that corona thrusters outperform DBDs. This is partly because a larger data range is collected for coronas than DBDs. Corona thrusters are tested with chords up to 330 mm and gap spacings up to 150 mm; the corresponding values for DBD thrusters (Figure 62) are 190 mm and 130 mm. The corona thrusters tested should therefore benefit more from increased gap spacing (Section 2.2.3); they should also suffer less from reverse emission. Finally, negative corona thrusters slightly outperform positive ones. The cause of this is unclear.

Thrust-to-power vs. thrust data for two-stage exposed thrusters is shown in Figure 63, Figure 64, Figure 65, and Figure 66.

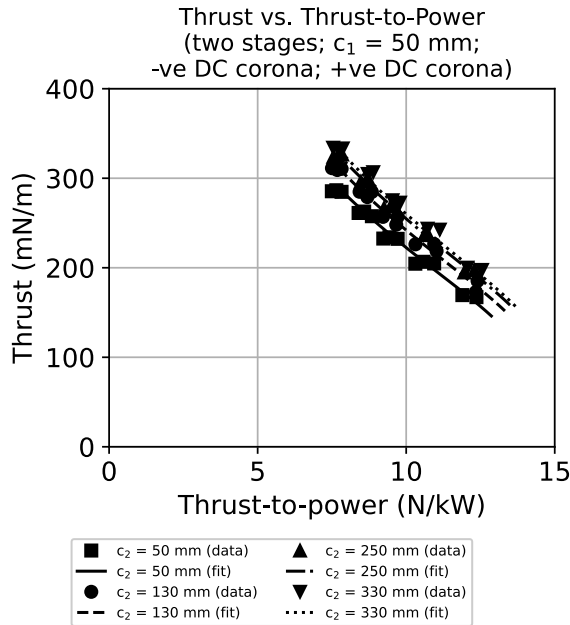


Figure 63: Thrust vs. thrust-to-power for a two-stage thruster, with a negative DC corona first stage and a positive DC corona second stage. The first collector chord is 50 mm.

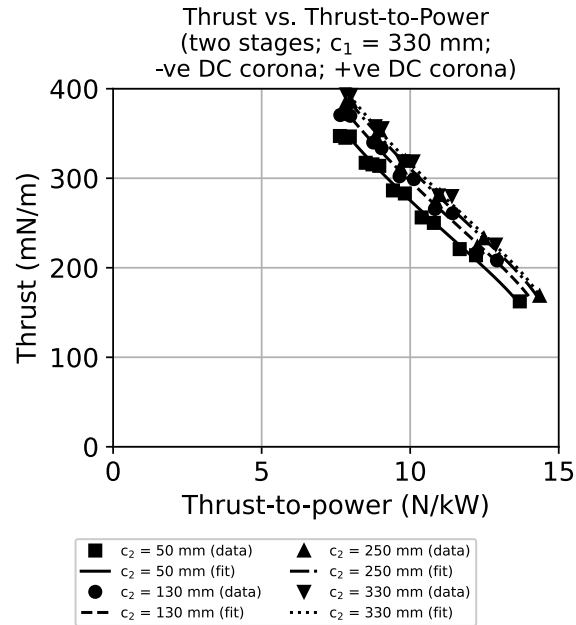


Figure 64: Thrust vs. thrust-to-power for a two-stage thruster, with a negative DC corona first stage and a positive DC corona second stage. The first collector chord is 330 mm.

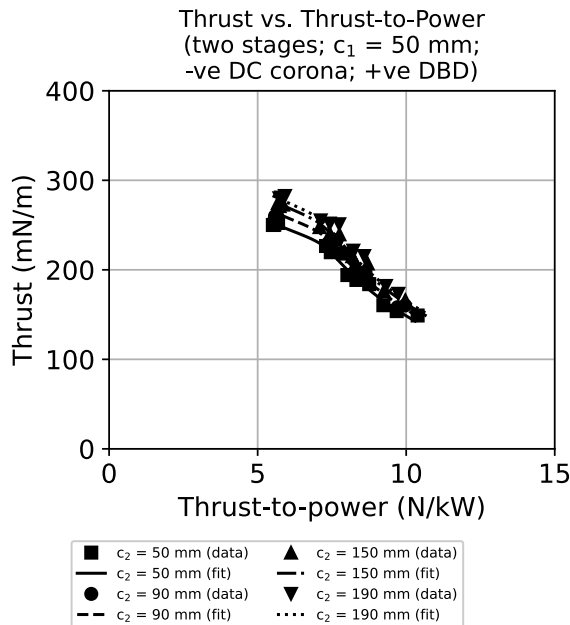


Figure 65: Thrust vs. thrust-to-power for a two-stage thruster, with a negative DC corona first stage and a positive DBD second stage. The first collector chord is 50 mm.

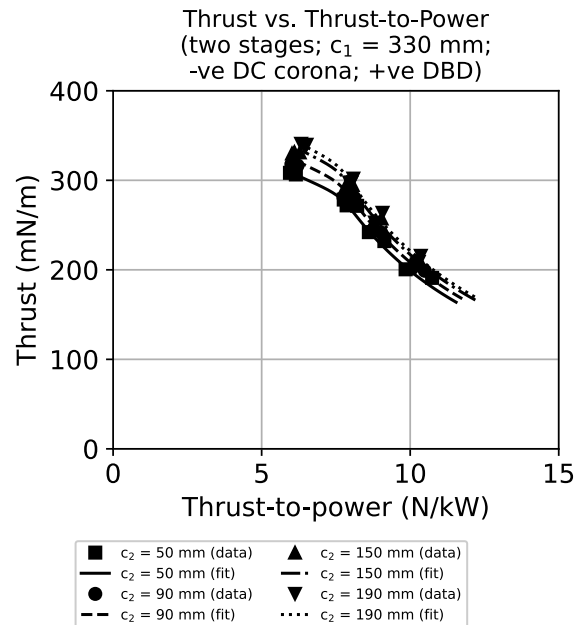


Figure 66: Thrust vs. thrust-to-power for a two-stage thruster, with a negative DC corona first stage and a positive DBD second stage. The first collector chord is 330 mm.

Figure 63, Figure 64, Figure 65, and Figure 66 show similar trends to the single-stage thrusters: thrust increases with increased collector chord (both c_1 and c_2), and corona thrusters outperform DBD thrusters.

Figure 60 through Figure 66 all show reasonable agreement between the fits and the experimental data. RMS errors for each thruster type and fit are summarized in Table 42. Errors are below 4% in all cases.

Table 42: Exposed thruster fit RMS errors.

Thruster type	Fit	RMS error
Single-stage positive DC corona	$\frac{P}{b} = f\left(c, \frac{T}{b}\right)$	2.8%
	$V = f\left(c, \frac{T}{b}\right)$	2.6%
	$T_{\max} = f(c)$	0.4%
Single-stage negative DC corona	$\frac{P}{b} = f\left(c, \frac{T}{b}\right)$	3.2%
	$V = f\left(c, \frac{T}{b}\right)$	2.5%
	$T_{\max} = f(c)$	2.1%
Two-stage positive DC corona + negative DC corona	$\frac{P}{b} = f\left(c_1, c_2, \frac{T}{b}\right)$	2.6%
	$V = f\left(c_1, c_2, \frac{T}{b}\right)$	2.6%
	$T_{\max} = f(c_1, c_2)$	1.2%
Single-stage positive DBD	$\frac{P}{b} = f\left(c, \frac{T}{b}\right)$	2.6%
	$V = f\left(c, \frac{T}{b}\right)$	1.7%
	$T_{\max} = f(c)$	1.0%
Two-stage negative DC corona + positive DBD	$\frac{P}{b} = f\left(c_1, c_2, \frac{T}{b}\right)$	2.5%
	$V = f\left(c_1, c_2, \frac{T}{b}\right)$	0.7%
	$T_{\max} = f(c_1, c_2)$	0.8%

Appendix B Induced drag of biplanes and tandem wings

The induced drag model discussed in Section 3.2.6.3 applies to monoplanes. However, induced drag of the biplane and tandem wing configurations are affected by interference between the two wings. Equation (54) is therefore not directly applicable.

For a biplane, induced drag can be modeled following the treatment of Gudmundsson [77] as

$$(C_D)_{\text{induced}} = \frac{1 + \sigma}{2} \frac{C_L^2}{\pi e_{\text{Oswald}} \text{AR}} \quad (77)$$

$$\sigma = \frac{1 - 0.66 \frac{h}{b}}{1.055 + 3.7 \frac{h}{b}} \quad (78)$$

where σ is the biplane interference factor, h is the vertical spacing between the two wings, and b is the planar wingspan. Equation (78) is only valid for $0.05 < \frac{h}{b} < 0.4$.

Equation (78) is not immediately compatible with signomial programming. Instead, a two-term posynomial fit is applied to $\frac{1+\sigma}{2} = f\left(\frac{h}{b}\right)$, for $0.05 < \frac{h}{b} < 0.4$. The resulting fit gives an RMS error of 1.1%.

Equation (78) does not apply to the tandem wing. Instead, tandem-wing drag is modeled by assuming that $\frac{1+\sigma}{2} = 1.025$. $\frac{1+\sigma}{2} = 1$ is analogous to a biplane with a vertical spacing of 0.

Appendix C V3 wing structural model

The V3 wing structural model is described in this Appendix. The wing models for the MSD vehicles (Chapters 4 and 5) are similar, except that the shear loads are taken by the spar web, instead of the spar core.

The V3 wing is sized using loads from a symmetric maneuver pull-up, with a limit load factor of 2.5. This load factor is within the range of typical values for general-aviation aircraft [62]. The V3 wing spar consists of carbon-fiber spar caps and a balsa core. The spar caps take the bending loads, while the core takes the shear. The spar root bending moment, root shear load, and wing tip deflection are then computed using

$$M_{\text{root}} = NW_{\text{fuselage}} \frac{1 + 2\lambda}{1 + \lambda} \quad (79)$$

$$S_{\text{root}} = \frac{NW_{\text{fuselage}}}{2} \quad (80)$$

$$(I_{\text{cap}})_{\text{root}} = 2c_{\text{spar}}(t_{\text{cap}})_{\text{root}} \left[\frac{(t_{\text{core}})_{\text{root}}}{2} \right]^2 \quad (81)$$

$$\Delta_{\text{tip}} = \frac{NW_{\text{fuselage}}}{E_{\text{cap}}(I_{\text{cap}})_{\text{root}}} \frac{b^3}{96} \frac{1 + 2\lambda}{1 + \lambda} \quad (82)$$

where M_{root} is the spar root bending moment, $N = 2.5$ is the load factor, W_{fuselage} is the fuselage weight (i.e., not including the weight of the wing or wing-mounted thrusters), λ is the wing taper ratio, S_{root} is the spar root shear load, $(I_{\text{cap}})_{\text{root}}$ is the spar cap root fourth moment of area, c_{spar} is the spar chord, $(t_{\text{cap}})_{\text{root}}$ is the spar cap root thickness, $(t_{\text{core}})_{\text{root}}$ is the spar core root thickness, Δ_{tip} is the wing tip deflection, E_{cap} is the spar cap Young's modulus, and b is the wingspan. Equations (79) and (82) are obtained from Drela [92], assuming approximately constant wing curvature. Equation (81) is obtained from Burton & Hoburg [81], assuming a thin spar cap; i.e., $(t_{\text{cap}})_{\text{root}} \ll (t_{\text{core}})_{\text{root}}$. The wing tip deflection is constrained to be less than 5% of the wingspan.

Bending and shear stresses are then computed using

$$A_{\text{root}} = c_{\text{spar}}(t_{\text{core}})_{\text{root}} \quad (83)$$

$$(\sigma_{\text{bending}})_{\text{cap}} = \frac{M_{\text{root}}}{(I_{\text{cap}})_{\text{root}}} \frac{(t_{\text{core}})_{\text{root}}}{2} \quad (84)$$

$$(\sigma_{\text{bending}})_{\text{core}} = (\sigma_{\text{bending}})_{\text{cap}} \frac{E_{\text{core}}}{E_{\text{cap}}} \quad (85)$$

$$(\sigma_{\text{shear}})_{\text{core}} = \frac{3 S_{\text{root}}}{2 A_{\text{root}}} \quad (86)$$

where A_{root} is the spar core root cross-sectional area, $(\sigma_{\text{bending}})_{\text{cap}}$ is the cap bending stress, $(\sigma_{\text{bending}})_{\text{core}}$ is the core bending stress, $(\sigma_{\text{shear}})_{\text{core}}$ is the core shear stress, and E_{core} is the core Young's modulus. Equation (84) is Navier's equation for beam bending, while Equation (85) is derived by assuming that the strain at the interface between the spar caps and core are equal. Finally, Equation (86) holds for a square beam section.

Finally, the stresses are constrained to be less than the yield strengths of their respective component materials, including factors of safety. This is done via

$$s_{\text{bending}} (\sigma_{\text{bending}})_{\text{cap}} \leq (\sigma_{\text{yield, bending}})_{\text{cap}} \quad (87)$$

$$s_{\text{bending}} (\sigma_{\text{bending}})_{\text{core}} \leq (\sigma_{\text{yield, bending}})_{\text{core}} \quad (88)$$

$$s_{\text{shear}} (\sigma_{\text{shear}})_{\text{core}} \leq (\sigma_{\text{yield, shear}})_{\text{core}} \quad (89)$$

where $s_{\text{bending}} = s_{\text{shear}} = 1.5$ are factors of safety, $\sigma_{\text{yield, bending}}$ is the bending yield strength (minimum of the tensile and compressive yield strengths), and $\sigma_{\text{yield, shear}}$ is the shear yield strength. The active constraint is typically Equation (88); i.e., the wing is normally sized by bending stress in the spar core. This failure mode was encountered by the author's collaborators during structural testing of prototype V3 wing spars: the spar core failed in compression, causing the upper spar cap to buckle.

Appendix D V3 wing airfoil drag model

This Appendix describes the airfoil drag model for the V3 wing. The airfoil drag model models for the MSD vehicles (Chapters 4 and 5) are obtained similarly.

The two-dimensional wing airfoil drag coefficient is estimated using a fit to data from XFOIL [93]. Data is obtained for the NACA 44XX (NACA 4-series) airfoils, as a function of three variables:

- **Wing thickness-to-chord ratio:** $9\% \leq \frac{t}{c} \leq 13\%$. The XX above signifies that thickness-to-chord ratio is a design variable.
- **Wing mean Reynolds number:** $8 \times 10^4 \leq Re \leq 2 \times 10^5$. The Reynolds number is estimated using wing mean chord.
- **2D lift coefficient:** $0.5 \leq C_l \leq 1.19$. C_l is approximately equal to the wing 3D lift coefficient C_L .

The resulting data set contains 1,024 data points. The posynomial fit [80] has four terms; it can be written as

$$\begin{aligned} (C_{d_{\text{airfoil}}})_{\text{wing}} = & \left[(9.03388 \times 10^{35}) \left(\frac{t}{c}\right)^{5.76137} (Re)^{-7.80764} (C_l)^{2.80295} \right. \\ & + (1.18527 \times 10^{22}) \left(\frac{t}{c}\right)^{-0.0125994} (Re)^{-6.15163} (C_l)^{-0.694969} \\ & + (5585.97) \left(\frac{t}{c}\right)^{1.5999} (Re)^{-2.07591} (C_l)^{3.47025} \\ & \left. + (4781.15) \left(\frac{t}{c}\right)^{1.79818} (Re)^{-2.34898} (C_l)^{-3.35404} \right]^{\frac{1}{4.66957}} \end{aligned} \quad (90)$$

The fit RMS error is 1.0%. Equation (90) is directly implemented in design optimization

Airfoil drag fits for the V3 pylon, horizontal tail, vertical tail, and thruster collectors are prepared similarly, except without the dependence on 2D lift coefficient; i.e., $C_{d_{\text{airfoil}}} = f\left(\frac{t}{c}, Re\right)$. Fit ranges and RMS errors are provided in Table 14.

Appendix E Thruster drag model adjustments for wake velocity

An unducted thruster operates in its own ionic wind, so its components (emitter and collector) effectively “see” a flow velocity v_{eff} and dynamic pressure q_{eff} that are greater than freestream, increasing drag. A model for this effect was developed in Refs. [14], [15], and is repeated here.

v_{eff} and q_{eff} are estimated using

$$q_{\text{eff}} = \frac{1}{2} \rho v_{\text{eff}}^2 \quad (91)$$

$$q_{\text{eff}} = q_{\infty} + q_{\text{iw}} \quad (92)$$

$$q_{\text{iw}} = \frac{1}{2} \varepsilon \left(\frac{V}{d} \right)^2 \quad (93)$$

where q_{∞} is the freestream dynamic pressure and q_{iw} is the pressure increase due to the ionic wind. Equation (93) is obtained by balancing the electrostatic and dynamic pressures, as discussed in Chapter 2.6.1 of Gilmore [15]. q_{iw} and q_{eff} are also known as the ionic-wind pressure and wake pressure respectively.

In computing the Reynolds number for unducted thruster components that serve as either emitters or collectors, v_{eff} is used instead of v_{∞} (freestream velocity). Also, q_{eff} is used instead of q_{∞} to compute drag. In practice, the difference between v_{eff} and v_{∞} for unducted thrusters is typically on the order of 2 m/s or less. This can be seen from the ionic-wind velocities in Appendix J.

This model is not applied to ducted thrusters, because the flow velocity through the duct must be constant. This is because of conservation of mass in a one-dimensional system: the mass flow rate $\dot{m} = \rho v_2 A_2 = \rho v_3 A_3$ is constant (see Figure 8 for subscript definitions). The MSD thruster model in this work is incompressible and $A_2 = A_3$, so $v_2 = v_3$ and the emitter and collector “see” the same flow velocity. This can also be seen from Equation (10).

Appendix F Cylinder drag model

The estimates for the drag of cylindrical wires in this thesis are obtained using a posynomial fit [80] to cylinder drag data from Figure 1.12 of Ref. [135]. The resulting model is

$$\text{Re}_{\text{wire}} = \frac{\nu d_{\text{wire}}}{\nu} \quad (94)$$

$$(C_d)_{\text{wire}} = (2298.12 \text{ Re}_{\text{wire}}^{-0.958591} + 8.11799 \times 10^6 \text{ Re}_{\text{wire}}^{-3.80682})^{\frac{1}{7.16293}} \quad (95)$$

$$D_{\text{wire}} = \frac{1}{2} \rho \nu^2 l_{\text{wire}} d_{\text{wire}} (C_d)_{\text{wire}} \quad (96)$$

where Re_{wire} is the wire local Reynolds number, ν is the local flow velocity, d_{wire} is the wire diameter, $(C_d)_{\text{wire}}$ is the wire drag coefficient, l_{wire} is the wire length, and D_{wire} is the wire drag. Data for the fit in Equation (95) is obtained for $1 \leq \text{Re}_{\text{wire}} \leq 1,000$; the fit RMS error is 3.6%.

Appendix G V3 sketches

Sketches of the V3, generated using Open Vehicle Sketch Pad (OpenVSP) [109], are shown in Figure 67 – Figure 70. All sketches are drawn using dimensions from the design optimization results; they are therefore to scale.



Figure 67: Front view of the V3.



Figure 68: Side view of the V3.

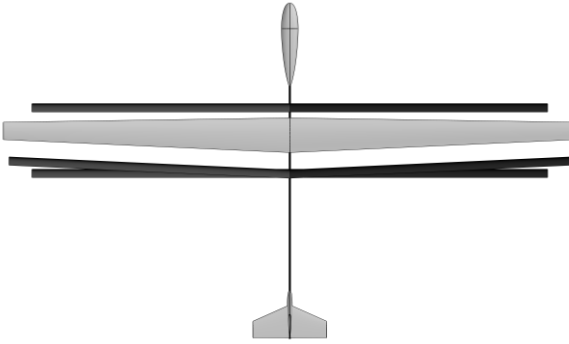


Figure 69: Top view of the V3.

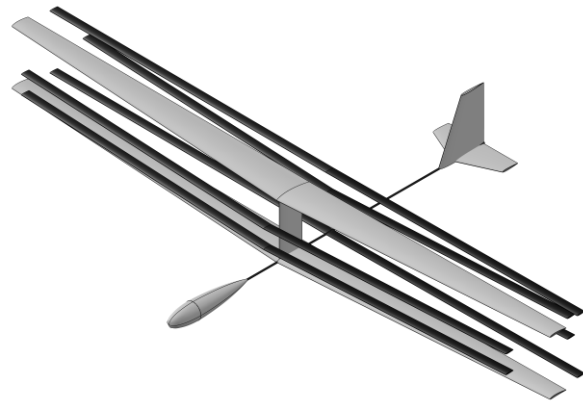


Figure 70: Isometric view of the V3.

Appendix H V3 dimensional data

Detailed dimensional data for the V3, taken from the optimization results, is given in Table 43.

Table 43: Detailed dimensional data for the V3.

Overall length	2.036 m
Overall wingspan	3.500 m
Takeoff mass	3.04 kg
Takeoff weight	29.8 N
Wing loading	2.76 kg/m ²
Empty mass fraction	47.8%
Max thrust	3.76 N
Max power draw	515.0 W
Max thrust-to-weight	0.13
Fuselage pod length	0.519 m
Fuselage pod radius	0.051 m
Fuselage pod diameter	0.102 m
Fuselage pod volume	2.804 l
Fuselage pod storage volume	1.402 l
Tail boom length	2.036 m
Tail boom radius	0.005 m
Tail boom diameter	0.010 m
Tail boom wall thickness	1.50 mm
Planar wing span	3.500 m
Planar wing area	0.551 m ²
Planar wing mean chord	0.157 m
Planar wing root chord	0.210 m
Planar wing tip chord	0.105 m
Planar wing aspect ratio	22.25
Planar wing taper ratio	0.50
Planar wing t/c ratio	9.0%
Biplane wing spacing (vertical)	0.348 m
Biplane wing spacing	10.0%

(% of span)	
Pylon height (span)	0.348 m
Pylon chord	0.147 m
Pylon aspect ratio	2.37
Pylon t/c ratio	15.0%
Horizontal tail span	0.45 m
Horizontal tail chord	0.15 m
Vertical tail span	0.34 m
Vertical tail chord	0.22 m
Battery volume	401.8 cm ³
Battery energy capacity	110.9 Wh
Battery maximum power	1.93 kW
HVPC maximum input power	0.52 kW
HVPC maximum output power	0.44 kW
HVPC specific power	1.03 kW/kg
HVPC efficiency	85.0%
Positive exposed DC corona thruster span	6.30 m
Positive exposed DC corona thruster geometric span	3.15 m
Positive exposed DC corona thruster collector chord	50.0 mm
Positive exposed DC corona thruster collector covered fraction	30.0%
Positive exposed DC corona thruster gap spacing	105.6 mm
Positive exposed DC corona thruster DC corona emitter diameter	0.127 mm
Positive exposed DC corona thruster height per stage	0.158 m

Positive exposed DC corona thruster total height	0.317 m
Positive exposed DC corona thruster number of stages	1.0
Positive exposed DC corona thruster number of thrusters per stage	2.0
Positive exposed DC corona thruster number of thrusters above pylon	0.0
Positive exposed DC corona thruster max applied voltage	60.0 kV
Positive exposed DC corona thruster max thrust per span	133.4 mN/m
Negative exposed DC corona thruster span	6.30 m
Negative exposed DC corona thruster geometric span	3.15 m
Negative exposed DC corona thruster collector chord	50.0 mm
Negative exposed DC corona thruster collector covered fraction	30.0%
Negative exposed DC corona thruster gap spacing	105.6 mm
Negative exposed DC corona thruster DC corona emitter diameter	0.127 mm
Negative exposed DC corona thruster height per stage	0.142 m
Negative exposed DC corona thruster total height	0.283 m
Negative exposed DC corona thruster number of stages	1.0

Negative exposed DC corona thruster number of thrusters per stage	2.0
Negative exposed DC corona thruster number of thrusters above pylon	0.0
Negative exposed DC corona thruster max applied voltage	60.0 kV
Negative exposed DC corona thruster max thrust per span	168.2 mN/m
LE/TE DC corona thruster span	6.86 m
LE/TE DC corona thruster geometric span	3.43 m
LE/TE DC corona thruster 1st collector chord	170.0 mm
LE/TE DC corona thruster 1st collector covered fraction	30.0%
LE/TE DC corona thruster 2nd collector chord	50.0 mm
LE/TE DC corona thruster 2nd collector covered fraction	30.0%
LE/TE DC corona thruster 1st gap spacing	116.7 mm
LE/TE DC corona thruster 2nd gap spacing	116.7 mm
LE/TE DC corona thruster DC corona emitter diameter	0.127 mm
LE/TE DC corona thruster max applied voltage	60.0 kV
LE/TE DC corona thruster max thrust per span	324.3 mN/m

Appendix I V3 mass breakdown

A mass breakdown for the V3 is provided in Table 44. The design mass data is taken directly from the optimization results; the as-built mass data is obtained via measurement of built components, as reported by Perovich [71].

Table 44: Mass breakdown for the V3.

Component	Design		As-built	
	Mass (kg)	Mass / total (-)	Mass (kg)	Mass / total (-)
Fuselage pod	0.07	2.2%	0.06	1.5%
Tail boom	0.14	4.7%	0.27	7.4%
Wings	0.46	15.0%	0.85	23.6%
Pylon	0.12	3.8%	0.13	3.6%
Horizontal tail	0.02	0.7%	0.06	1.5%
Vertical tail	0.04	1.2%	0.05	1.4%
Landing gear	0.03	0.9%	0.13	3.5%
Exposed thrusters	0.10	3.2%	0.37	10.4%
Leading- and trailing-edge thruster	0.11	3.6%	0.19	5.3%
Battery	0.96	31.7%	0.28	7.7%
Power converter	0.42	13.9%	0.76	21.1%
Payload	0.20	6.6%	0.17	4.7%
Miscellaneous	0.10	3.3%	0.01	0.4%
Margin	0.28	9.1%	0.28	7.9%
Total	3.04	100.0%	3.60	100.0%

The design and as-built mass accounting systems differ in the following ways:

- **Battery and power converter:** the battery pack used for flight testing weighed 0.28 kg, much less than the design battery mass of 0.96 kg. In addition, the V3 built airframe did not have a power converter, but it did have a motor, propeller, and motor pylon. To compensate for all of this, ballast weighing 0.55 kg is added to the airframe during flight testing. The as-built power-converter mass in Table 44 therefore includes the motor, propeller, motor pylon, and ballast.
- **Payload:** the V3 carried a camera weighing 0.171 kg during flight testing, slightly less than the design payload mass of 0.2 kg.

- **Avionics:** the as-built mass includes only servo mass as part of miscellaneous mass. The mass of the receiver, pitot tube (used to measure airspeed), and the rest of the avionics system is included in the margin instead.

Appendix J V3 performance data

Detailed performance data for the V3, broken down by mission segment, is provided in Table 45.

This data is taken directly from the optimization results.

Table 45: Detailed performance data for the V3.

Mission segment	Takeoff	Loiter	Bank	Dash	Units
Segment time	n/a	13.8	0.0	0.0	minutes
Segment battery energy	n/a	393.30	0.50	0.5	kJ
Airspeed	6.82	6.82	6.82	7.50	m/s
Lift coefficient	0.95	0.95	1.01	0.79	-
Profile drag coefficient	778.9	778.7	786.3	705.6	Counts
Induced drag coefficient	250.2	250.2	283.4	170.9	Counts
Margin drag coefficient	123.5	123.5	128.4	105.2	Counts
Total drag coefficient	1152.6	1152.5	1198.1	981.7	Counts
Lift-to-drag ratio	8.2	8.2	8.4	8.0	-
Thrust (total)	3.76	3.62	3.76	3.73	N
Thrust (positive exposed DC corona thruster)	0.79	0.76	0.79	0.78	N
Thrust (negative exposed DC corona thruster)	0.95	0.92	0.95	0.95	N
Thrust (LE/TE DC corona thruster)	2.02	1.94	2.02	2.00	N
Power (battery)	515.0	476.6	515.0	506.3	W
Power (HVPC)	437.7	405.1	437.8	430.3	W
Power (positive exposed DC corona thruster)	89.8	82.7	89.9	88.2	W
Power (negative exposed DC corona thruster)	114.7	107.2	114.7	113.0	W
Power (LE/TE DC corona thruster)	233.3	215.2	233.2	229.1	W
Voltage (positive exposed DC corona thruster)	59.6	59.3	59.6	59.5	kV
Thrust-to-power (positive exposed DC corona thruster)	8.76	9.13	8.75	8.84	N/kW
Thrust per span (positive exposed DC corona thruster)	124.8	119.9	124.8	123.7	mN/m
Power per span (positive exposed DC corona thruster)	14.25	13.13	14.27	13.99	W/m
Ionic-wind velocity (positive exposed DC corona thruster)	1.52	1.52	1.52	1.52	m/s

Wake velocity (positive exposed DC corona thruster)	6.99	6.99	6.99	7.66	m/s
Ionic-wind pressure (positive exposed DC corona thruster)	1.42	1.41	1.42	1.42	N/m ²
Wake pressure (positive exposed DC corona thruster)	29.92	29.91	29.92	35.91	N/m ²
Voltage (negative exposed DC corona thruster)	59.9	59.6	59.9	59.8	kV
Thrust-to-power (negative exposed DC corona thruster)	8.31	8.58	8.31	8.37	N/kW
Thrust per span (negative exposed DC corona thruster)	151.2	146.0	151.2	150.1	mN/m
Power per span (negative exposed DC corona thruster)	18.20	17.01	18.20	17.94	W/m
Ionic-wind velocity (negative exposed DC corona thruster)	1.70	1.70	1.70	1.70	m/s
Wake velocity (negative exposed DC corona thruster)	7.03	7.03	7.03	7.69	m/s
Ionic-wind pressure (negative exposed DC corona thruster)	1.78	1.76	1.78	1.78	N/m ²
Wake pressure (negative exposed DC corona thruster)	30.28	30.27	30.28	36.26	N/m ²
Voltage (LE/TE DC corona thruster)	59.9	59.6	59.9	59.8	kV
Thrust-to-power (LE/TE DC corona thruster)	8.67	9.03	8.67	8.75	N/kW
Thrust per span (LE/TE DC corona thruster)	294.7	283.1	294.7	292.1	mN/m
Power per span (LE/TE DC corona thruster)	34.01	31.37	34.00	33.40	W/m
Ionic-wind velocity 1 (LE/TE exposed DC corona thruster)	1.38	1.37	1.38	1.38	m/s
Wake velocity 1 (LE/TE exposed DC corona thruster)	6.96	6.96	6.96	7.63	m/s
Ionic-wind pressure 1 (LE/TE exposed DC corona thruster)	1.16	1.15	1.16	1.16	N/m ²
Wake pressure 1 (LE/TE exposed DC corona thruster)	29.67	29.66	29.67	35.65	N/m ²
Ionic-wind velocity 2 (LE/TE exposed DC corona thruster)	1.38	1.37	1.38	1.38	m/s
Wake velocity 2 (LE/TE exposed DC corona thruster)	6.96	6.96	6.96	7.63	m/s
Ionic-wind pressure 2 (LE/TE exposed DC corona thruster)	1.16	1.15	1.16	1.16	N/m ²
Wake pressure 2 (LE/TE exposed DC corona thruster)	29.67	29.66	29.67	35.65	N/m ²

Appendix K V3 aerodynamic design

Aerodynamic analysis and design of the V3, beyond that performed by the optimizer, forms the subject of this Appendix.

Airfoil selection: the wing airfoil profile drag model (Appendix D) uses XFOIL data from the NACA 44XX series of airfoils. Thickness-to-chord ratio is a design variable, hence the XX. The optimizer selects a thickness-to-chord ratio of 9%, equal to the lower limit (see Section 3.2.6). However, the V3 wing uses the Aquila SM airfoil (the same airfoil as the V2 wing), instead of the NACA 4409 airfoil thus recommended by the optimizer. Two modifications are made to the Aquila SM:

- **The thickness-to-chord ratio is rescaled** to 9%, in line with the design optimization results. The original Aquila SM has a thickness-to-chord ratio of 9.3%.
- **The leading-edge radius is increased** from 0.79% to 0.92%. Since the wing leading edge is also a thruster collector, this choice helps mitigate reverse emission (see Appendix A).

This choice of airfoil is made for two reasons:

- **Drag:** analysis in XFOIL [93] reveals that the profile drag coefficient of the modified Aquila SM in loiter is 234 counts, about 6% lower than that of the NACA 4409 (247 counts).
- **Manufacturing:** the Aquila SM, unlike the NACA 4409, has a flat bottom surface. Wings using it can therefore be built on a flat table, without a specialized jig.

The profile drag model for the thruster collectors (Table 14) uses data from the HT14 airfoil, with its thickness-to-chord ratio rescaled to 10%. Once the optimizer selects a design point, the HT14 leading-edge radius is increased from 1.5% to 2.6%. This change does not affect profile drag (which stays fixed at 221 counts), but it serves to mitigate reverse emission.

The wing and collector airfoils are shown in Figure 71 and Figure 72 respectively.



Figure 71: The modified Aquila SM airfoil used for the V3 wing.



Figure 72: The modified HT14 airfoil used for the V3 thruster collectors.

Stability and control: A model of the V3 is constructed using the Athena Vortex Lattice (AVL) software package [136], in order to verify that the V3 is both stable and controllable in flight. An isometric view of the model is shown in Figure 73.

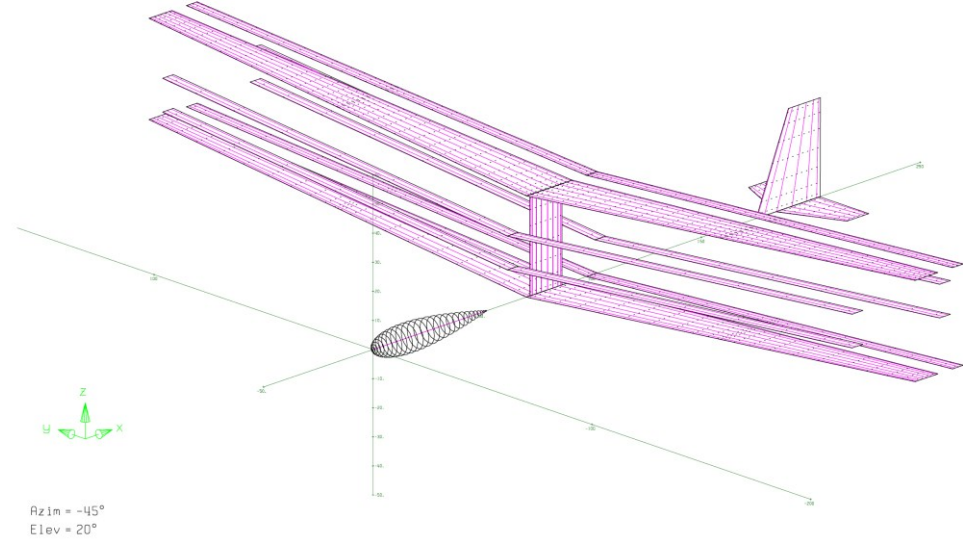


Figure 73: AVL model of the V3.

Recall from Section 3.2.2.1 that the V3 lacks ailerons. Instead, the elevator and rudder are used for control. This requires the wing to have sufficient dihedral, so that the aircraft can be controlled via yaw-roll coupling. In addition, the collectors have limited structural support (Section 3.2.7.4). Collector incidence angles are therefore set such that their contribution to lift is close to 0.

Dihedral and incidence angles for the wing, collectors, and horizontal tail are provided in Table 46. These values are used as inputs to the AVL model.

Table 46: Incidence and dihedral angles for the V3 components.

Component	Incidence	Dihedral
Upper wing	6°	5°
Upper wing trailing-edge collector	6°	5°
Lower wing	7°	5°
Lower wing trailing-edge collector	6°	5°
First-stage exposed collectors (both)	-3°	5°
Second-stage exposed collectors (both)	5°	5°
Horizontal tail	2°	0°

AVL analysis is carried out under loiter conditions. A Trefftz plot of the results, showing lift as a function of spanwise location, is shown in Figure 74.

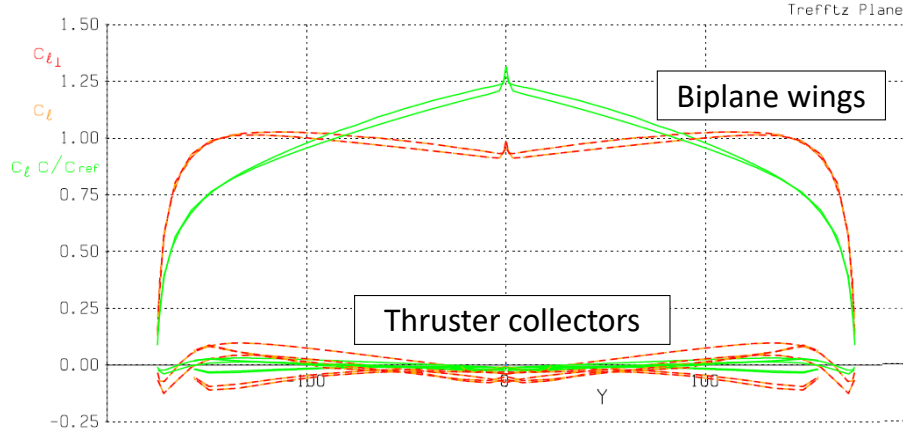


Figure 74: Trefftz plot for the V3, showing lift as a function of spanwise location Y (in cm).

Figure 74 shows that virtually all of the lift is carried by the biplane wings. The contribution from the thruster collectors is negligible, as desired.

In addition to loiter, the aircraft is analyzed in a bank of 20° , and during a stall segment ($C_L = C_{L_{max}} = 1.15$). Requirements for all three flight conditions, along with the associated analysis results, are provided in Table 47.

Table 47: Requirements and analysis results for each flight condition analyzed in AVL.

Flight condition	Requirement	Results
Loiter	Longitudinal static margin close to 15%.	Neutral point is at $x = 78.0$ cm, while CG is at 75.5 cm. With $\bar{c} = 15.7$ cm, the longitudinal static margin is 16%.
	Trimmed elevator angle close to 0.	1.4° of down elevator is required to trim.
	Positive lateral static stability: $C_{n_\beta} > 0$; $C_{l_\beta} < 0$.	$C_{n_\beta} = 0.0289$; $C_{l_\beta} = -0.163$. Aircraft is laterally statically stable.
	Validate optimization model for induced drag.	Optimizer returns an induced drag coefficient of 250 counts, 17% higher than the AVL value of 213 counts. Optimizer is therefore conservative.
Bank	Verify that the aircraft can be trimmed using rudder and elevator only in a 20° level bank at loiter speed.	Control-surface angles for trim: elevator = -3.1° ; rudder = -7.4° . Tip stall not encountered.
Stall	Check for any problematic tip stall tendencies.	Tip stall not encountered. Largest local lift coefficient (on upper wing) is 1.17.

Table 47 shows that the tabulated requirements are met. In particular, wing dihedral means that the aircraft is laterally both stable and controllable. Lateral static stability in loiter requires that the stability derivatives $C_{n\beta}$ (derivative of yawing moment with respect to sideslip angle) and $C_{l\beta}$ (derivative of rolling moment with respect to sideslip angle) be positive and negative respectively [62]. Table 47 shows that both of these conditions are met. In addition, the aircraft can be trimmed in bank with only the elevator and rudder; ailerons are not required. Similarly, the loiter analysis in Table 47 shows that the V3 is longitudinally statically stable, with a static margin of 16%.

The analysis in this Appendix assumes that the V3 center of gravity is located at $x = 75.5$ cm behind the nose. A component CG analysis in a spreadsheet is conducted to verify this. The camera payload is mounted in the tail, but the required CG location is achieved. For comparison, the middle of the pylon is located at $x = 79.5$ cm behind the nose.

Appendix L V3 mass and drag model issues

As discussed in Section 3.3.4, the V3 airframe does not perform as well as designed. One cause is underprediction of vehicle mass by the design model. Table 44 shows that the measured mass of the V3 airframe (including adjustments for the power converter, motor, and motor pylon) is 3.60 kg, 18.4% higher than the design value of 3.04 kg. The mass model has the following issues [71]:

- **Epoxy margins:** when estimating a composite component using its dimensions, a rule of thumb is to multiply the material density by 2, to account for the mass of the resin (not just the fibers). This rule of thumb is not incorporated into V3 design optimization, but it is incorporated into design optimization of the MSD aircraft. Similarly, while component-level mass margins are maintained, the mass of other adhesives (ex. tape) are not included.
- **Component availability:** some components are not available in the dimensions specified by the optimizer; heavier substitutes are used instead. For example, the optimization results specify a Kevlar tube with a diameter of 1 cm and a wall thickness of 1.5 mm for the tail boom. A tube with the required dimensions could not be obtained, and so a tube with approximately twice the required diameter is used instead. This approximately doubles the tail-boom mass. Component availability issues with the wing spar caps also increase mass.
- **Landing and handling loads:** several components on the aircraft are ultimately sized by landing loads, rather than by aerodynamic loads predictable during optimization. This results in increased mass. For example, the landing gear (designed and built by the author) went through several design iterations to improve crashworthiness. Its final (measured) mass is 128 g, almost five times as high as assumed by the optimizer.
- **Detailed design information:** the mass of some components is accounted for implicitly, via margins. However, challenges were encountered during detailed design that resulted in the margins being exceeded. For example, the exposed collectors require carbon-fiber stiffeners for structural rigidity, increasing their mass by a factor of more than 3 relative to design mass. Similarly, the tail is built out of balsa wood; it weighs almost twice as much as the foam tail assumed by the optimizer. Neither of these design changes are included in design optimization. Similar arguments can be made for the pylon spar and for the exposed-

thruster holders, for both of which mass is modeled via margins rather than via explicit geometry-dependent models.

The drag model may also contribute to the higher-than-expected cruise throttle setting. Lift-to-drag ratio was not estimated from the flight tests, but the drag model (like the mass model) relies in several places on margins, rather than explicit geometry models. For example, the exposed-thruster holders are not explicitly included in the drag model; they are included via a margin. Similarly, the aforementioned landing-gear redesign for crashworthiness likely increases drag as well as mass.

These issues mostly relate to modeling and documentation; i.e., they can be fixed by ensuring that the assumptions made by the design model are consistent with what is actually built and tested. They should therefore be addressable in a redesign.

Appendix M Package delivery aircraft 3-view sketches

3-view, to-scale sketches of the package-delivery monoplane are shown in Figure 75 – Figure 80.

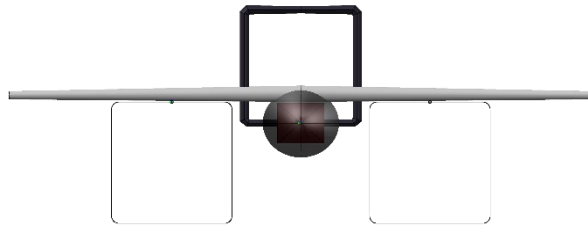


Figure 75: Front view of the monoplane in wingborne flight.



Figure 76: Front view of the monoplane in hover.

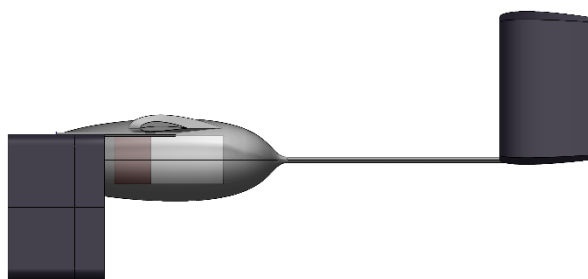


Figure 77: Side view of the monoplane in wingborne flight.

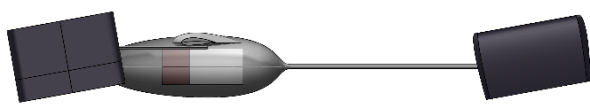


Figure 78: Side view of the monoplane in hover.

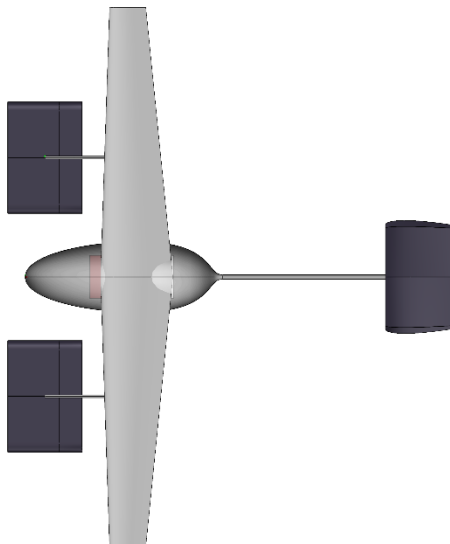


Figure 79: Top view of the monoplane in wingborne flight.

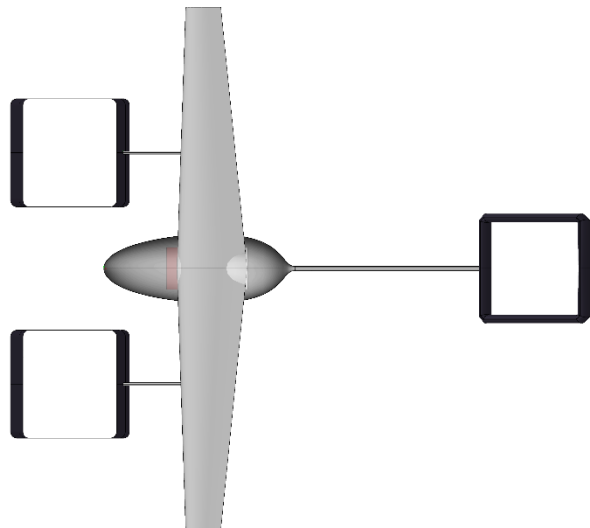


Figure 80: Top view of the monoplane in hover.

3-view, to-scale sketches of the package-delivery box wing are shown in Figure 81 – Figure 86.

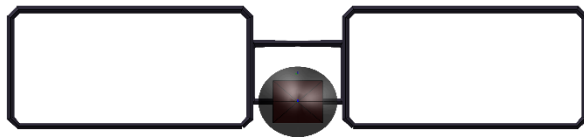


Figure 81: Front view of the box wing in wingborne flight.



Figure 82: Front view of the box wing in hover.

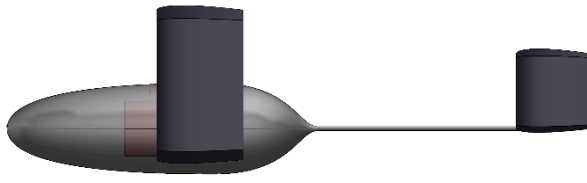


Figure 83: Side view of the box wing in wingborne flight.



Figure 84: Side view of the box wing in hover.

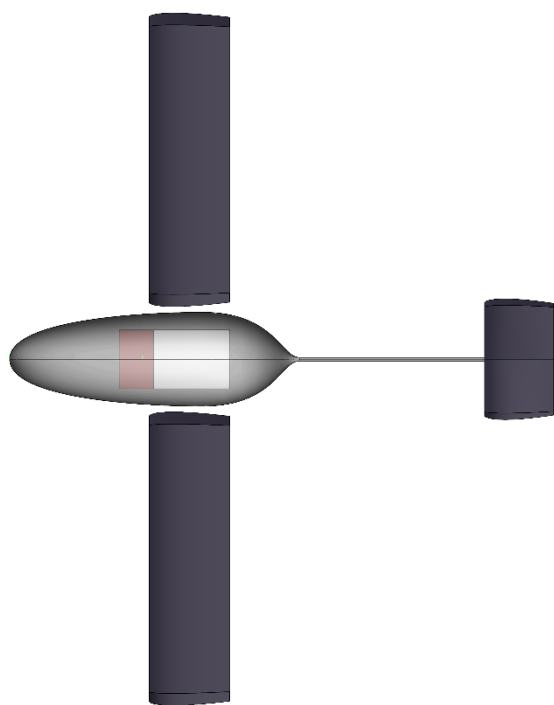


Figure 85: Top view of the box wing in wingborne flight.

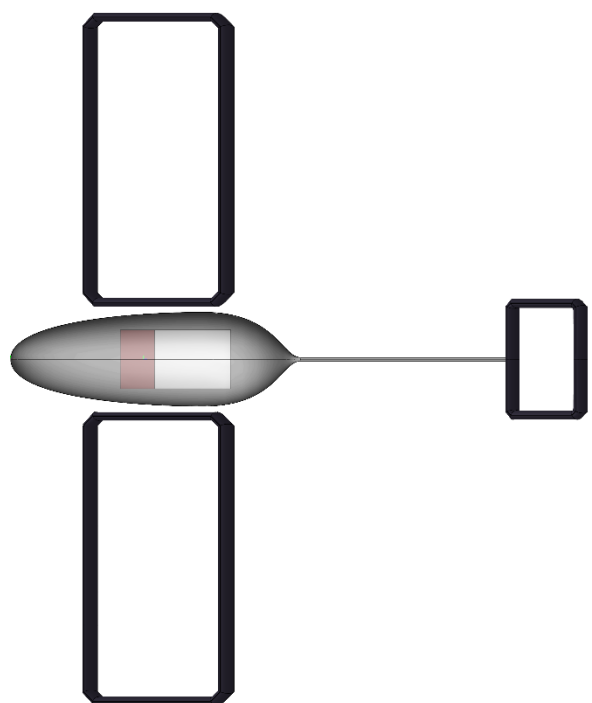


Figure 86: Top view of the box wing in hover.

All sketches are drawn using dimensions from the design optimization results.

Appendix N MSD thruster optimization model modifications

As mentioned in Section 2.3, equations (11), (12), (14), (18), (20), and (24) are reformulated for design optimization. This is done for one of two reasons:

- **The original form is not SP-compatible.** As mentioned in Section 3.2.3, a signomial program (the design optimization algorithm used in this work) requires that all models be formulated as monomial, posynomial, and signomial functions.
- **The original form is an equality, when an inequality would suffice.** In a signomial program, inequality constraints are generally more numerically efficient and robust than equality constraints. Posynomial equality relaxation [63] ensures that all inequality constraints are exactly satisfied at the optimum.

Therefore, for design optimization, equations (11), (12), (14), (18), (20), and (24) are written as equations (97)-(102) respectively:

$$v_4^2 \leq v_\infty^2 + 2 \frac{\Delta P}{\rho} \quad (97)$$

$$\frac{T}{A_2} + \frac{D_{\text{wall}}}{A_2} + \rho v_4 v_\infty \phi \leq \rho v_4^2 \phi \quad (98)$$

$$n(\Delta P)_{\text{EAD}} \geq \Delta P + n(\Delta P)_{\text{loss}} \quad (99)$$

$$\overline{(\Delta P)_{\text{EAD}}} + \frac{1}{3} \overline{v_2}^2 \leq 1 + \frac{2}{3} \overline{v_2} \quad (100)$$

$$\bar{J} \geq 1 + 2\bar{v}_2 + \bar{v}_2^2 \quad (101)$$

$$\frac{P}{A_2} \geq \left(\frac{P}{A_2} \right)_{\text{ion}} + \left(\frac{P}{A_2} \right)_{\text{accel}} \quad (102)$$

Appendix O MSD box wing modeling details

Modeling details specific to the box wing are discussed in this Appendix.

Lift distribution: unlike for a monoplane, the optimal lift distribution of a box wing is not elliptical [137], [138]. Instead, it consists of “a constant and an elliptical part for the horizontal wings and a linear and butterfly-shaped part for the vertical wings” [137]. This should in principle affect the box-wing drag and structural models, but it is neglected for the purpose of this study. Instead, a conservative value of wing Oswald efficiency (Table 26) is used.

Induced drag: like the biplane and tandem wing (Appendix B), induced drag of the box wing is affected by aerodynamic interference between the two wings. This effect can be modeled as a function of the wing height-to-span ratio [137], [139] as

$$\frac{(D_i)_{\text{box}}}{(D_i)_{\text{planar}}} = f\left(\frac{h}{b}\right) = \frac{k_1 + k_2 \frac{h}{b}}{k_3 + k_4 \frac{h}{b}} \quad (103)$$

where D_i is induced drag, h is the wing height (vertical distance between the upper and lower wings), b is the planar wingspan, and k_1-k_4 are constants. The subscripts $(\)_{\text{box}}$ and $(\)_{\text{planar}}$ refer to the box wing and to an equivalent planar wing respectively.

Box wing height is an optimizer design variable, but Equation (103) is not used directly in design optimization. This is because Equation (103) is a signomial equation, which cannot generally be solved as efficiently as a monomial or posynomial [85]. Instead, values for k_1-k_4 are obtained from Ref. [57]. A posynomial fit [80] to Equation (103) is then obtained as

$$\frac{(D_i)_{\text{box}}}{(D_i)_{\text{planar}}} = \left[0.941763 \left(\frac{h}{b} \right)^{-0.0195267} \right]^{10} \quad (104)$$

Equation (104) corresponds to data for $0.03 \leq \frac{h}{b} \leq 0.8$; the fit RMS error is 3.99%. Equation (104) is a monomial equation, and is directly implemented in design optimization.

Wing curvature: the wing structural model (Appendix C) assumes the wing bends with constant curvature due to the applied lift force. Ref. [92] shows that this approximation is reasonable for a wing taper ratio of 0.5 (the monoplane value), but overestimates the wing tip deflection for a taper

ratio of 1.0 (the box wing value). Since the wing tip deflection is constrained to below 5% of the wingspan for both vehicles, constant bending curvature is therefore a conservative approximation.

Electroaerodynamic interference: the box wing contains a thruster, so the lift and induced drag of the wing should be affected by the thruster, and vice versa. For the purpose of this study, this effect is neglected. Instead, it is assumed that lift and induced drag are both independent of thrust. The same approximation is made for the box tail. This is discussed further in Section 6.4.

Appendix P Package delivery aircraft hover balance model

The MSD package-delivery aircraft must balance in hover; i.e., the moments from each thruster, taken about the vehicle center of gravity (CG), must sum to zero. Models for ensuring this are the subject of this Appendix.

For the purpose of design optimization, the center of gravity of both vehicles is assumed to be located 60% of the distance along the fuselage-pod length, and also at the wing 50% chord position. Ideally, the payload centroid should also be close to the CG, so that the CG does not shift if the payload is changed or dropped.

A side view of the monoplane in hover, including the hover balance model parameters, is shown in Figure 87.

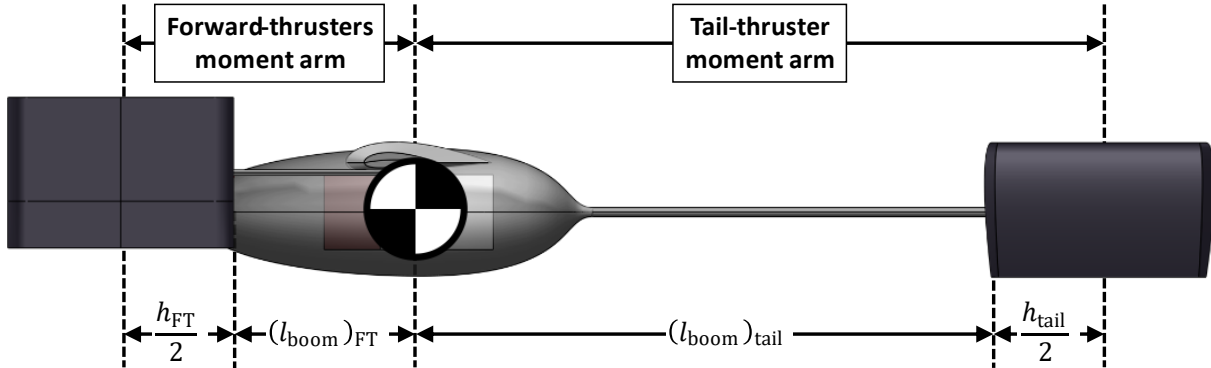


Figure 87: Side view of the monoplane, showing the hover balance model parameters.

The forward-thruster booms extend forwards from the CG to the forward thrusters, while the tail boom extends backwards from the CG to the box tail. Therefore, the moment arms of the forward thrusters and tail thruster are computed as

$$(l_{\text{momentArm}})_{\text{FT}} = \frac{h_{\text{FT}}}{2} + (l_{\text{boom}})_{\text{FT}} \quad (105)$$

and

$$(l_{\text{momentArm}})_{\text{tail}} = \frac{h_{\text{tail}}}{2} + (l_{\text{boom}})_{\text{tail}} \quad (106)$$

respectively, where $l_{\text{momentArm}}$ is the moment-arm length and h is the height. The subscripts $(\)_{\text{FT}}$, $(\)_{\text{boom}}$, and $(\)_{\text{tail}}$ refer to the forward thrusters, boom, and tail respectively.

Because the CG is located at the wing 50% chord position, the forward-thruster boom must be at least as long as half the wing root chord. The forward thrusters are also offset forwards from the wing by an amount equal to half the forward-thruster height, to ensure that their flow fields do not interfere in hover. This can be stated mathematically as

$$(l_{\text{boom}})_{\text{FT}} \geq \frac{1}{2} h_{\text{FT}} + \frac{1}{2} (c_{\text{root}})_{\text{wing}} \quad (107)$$

where $(c_{\text{root}})_{\text{wing}}$ is the wing root chord.

Finally, the hover balance constraint can be written as

$$2(T_{\text{hover}})_{\text{FT}}(l_{\text{momentArm}})_{\text{FT}} = (T_{\text{hover}})_{\text{tail}}(l_{\text{momentArm}})_{\text{tail}} \quad (108)$$

where T_{hover} is the hover thrust. The factor of 2 accounts for the two forward thrusters.

A side view of the box wing, including the hover balance moment arms, is shown in Figure 88.

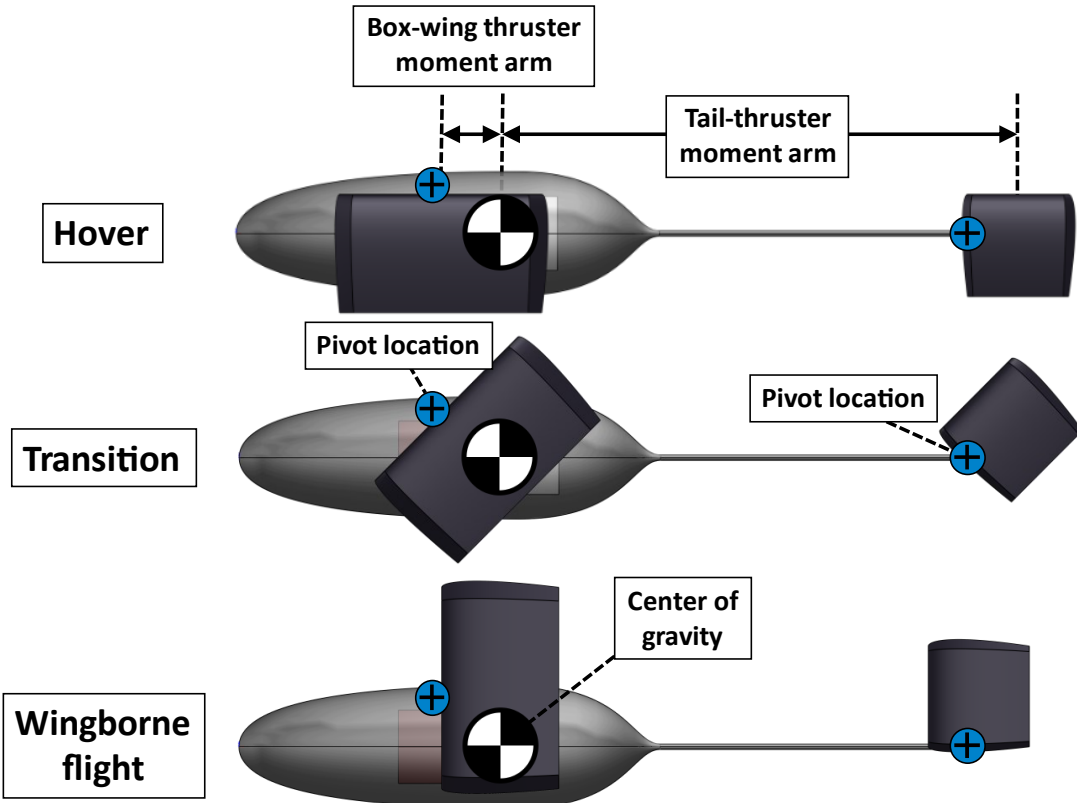


Figure 88: Side view of the box wing in hover (top), during transition (middle) and in wingborne flight (bottom). The thruster moment arms, the thruster pivot locations (blue circles with black crosses) and the center of gravity are also shown.

Equations (105)-(108) are required for the monoplane, to set the length (and, by extension, the mass and drag) of the forward-thruster booms during optimization. The box wing lacks a similar set of optimization constraints. Instead, the box-wing thruster pivot location (relative to the fuselage) is selected during post-processing, to ensure that the vehicle balances in hover. Figure 88 shows how this works: as the wing tilts for hover (top), its thrust vector moves forwards, so the box-wing thruster moment arm correctly extends forwards of the CG.

Vehicle center-of-gravity locations are estimated during post-processing, using a bottom-up approach in a spreadsheet. Results are in Table 48; they are defined relative to the vehicles' nose.

Table 48: Estimated center-of-gravity locations for the monoplane and box wing.

	Wingborne CG	Hover CG
Monoplane	47.7 cm	46.4 cm
Box wing	52.1 cm	49.4 cm

Table 48 shows that the CG locations are slightly different in wingborne flight and hover. This is because the nacelles and thrusters are in slightly different locations before vs. after they tilt. Also, the CG locations do not exactly correspond to the wing 50% chord position, as the optimizer assumes. Despite this, dimensional and thrust data is used to show (again in a spreadsheet) that the vehicles balance in hover. Results from the hover balance analysis are shown in Table 49.

Table 49: Results from the hover balance analysis.

	Monoplane		Box wing	
	Forward thrusters	Box-tail thruster	Box-wing thruster	Box-tail thruster
Hover thrust (total)	154.4 N	69.5 N	183.7 N	16.7 N
Thrust vector location	-14.0 cm	180.4 cm	39.3 cm	160.1 cm
Moment arm	60.3 cm	-134.0 cm	10.1 cm	-110.7 cm
Moment	9315 N-cm	-9316 N-cm	1853 N-cm	-1853 N-cm
Net moment / moment	0.0%	0.0%	0.0%	0.0%

For each vehicle and thruster, Table 49 gives the hover thrust (from the optimizer) and thrust vector location (estimated geometrically). The moment arm is the difference between the thrust vector and hover CG location (from Table 48). The moment is then the product of the hover thrust and

moment arm. Finally, the net moments sum to 0 for both vehicles, indicating that they balance in hover as required.

Note that the monoplane forward-thruster centroid in Table 49 is negative, indicating that it is located forwards of the nose. This can also be seen from Figure 87.

Appendix Q Package delivery aircraft dimensional data

Detailed dimensional data for the package delivery monoplane and box wing, taken directly from the optimization results, is given in Table 50 and Table 51 respectively. Note that number of thruster stages is approximated as a continuous variable, rather than as an integer.

Table 50: Dimensional data for the monoplane.

Parameter	Value
Overall length	1.621 m
Overall wingspan	2.214 m
Takeoff mass	20.8 kg
Takeoff weight	203.6 N
Wing loading	42.2 kg/m ²
Empty mass fraction	46.3%
Max power draw	29.91 kW
Fuselage pod length	0.810 m
Fuselage pod usable length	0.344 m
Fuselage pod width	0.290 m
Fuselage pod usable width	0.178 m
Fuselage pod height	0.259 m
Fuselage pod usable height	0.152 m
Tail boom length	1.135 m
Tail boom exposed length	0.810 m
Tail boom diameter	0.018 m
Tail boom wall thickness	2.00 mm
Planar wing span	2.214 m
Planar wing area	0.492 m ²
Planar wing mean chord	0.222 m
Planar wing root chord	0.296 m
Planar wing tip chord	0.148 m
Planar wing mean thickness	45.7 mm
Planar wing aspect ratio	9.96
Planar wing taper ratio	0.5
Planar wing t/c ratio	20.6%

Box tail chord	0.281 m
Box tail width	0.421 m
Box tail height	0.421 m
Box tail total horizontal planform area	0.237 m ²
Box tail total vertical planform area	0.237 m ²
Box tail section t/c ratio	10%
Forward booms length	0.377 m
Forward booms diameter	0.011 m
Forward booms wall thickness	2.00 mm
Forward nacelles quantity	2
Forward nacelles chord	0.305 m
Forward nacelles width	0.458 m
Forward nacelles height	0.458 m
Forward nacelles total horizontal planform area	0.279 m ²
Forward nacelles total vertical planform area	0.279 m ²
Battery length	0.115 m
Battery width	0.178 m
Battery height	0.152 m
Battery volume	3115.7 cm ³
Battery energy capacity	1495.5 Wh
Battery maximum power	29.91 kW
HVPC maximum input power	29.91 kW
HVPC maximum output power	25.42 kW

Box-tail thruster number of stages	19.5
Box-tail thruster gap spacing	10.0 mm
Box-tail thruster stage length	0.012 m
Box-tail thruster duct length	0.234 m
Box-tail thruster total length	0.281 m
Box-tail thruster duct cross-sectional area	0.177 m ²
Box-tail thruster exit cross-sectional area	0.177 m ²
Box-tail thruster exit area ratio	1.0

Forward thrusters quantity	2
Forward thrusters number of stages	21.2
Forward thrusters gap spacing	10.0 mm
Forward thrusters stage length	0.012 m
Forward thrusters duct length	0.254 m
Forward thrusters total length	0.305 m
Forward thrusters duct cross-sectional area	0.209 m ²
Forward thrusters exit cross-sectional area	0.209 m ²
Forward thrusters exit area ratio	1.0

Table 51: Dimensional data for the box wing.

Parameter	Value
Overall length	1.508 m
Overall wingspan	1.602 m
Takeoff mass	18.6 kg
Takeoff weight	182.2 N
Wing loading	24.1 kg/m ²
Empty mass fraction	45.7%
Max power draw	26.77 kW
Fuselage pod length	0.872 m
Fuselage pod usable length	0.332 m
Fuselage pod width	0.283 m
Fuselage pod usable width	0.178 m
Fuselage pod height	0.253 m
Fuselage pod usable height	0.152 m
Tail boom length	1.508 m
Tail boom exposed length	0.636 m
Tail boom diameter	0.011 m
Tail boom wall thickness	2.00 mm
Box wing planform area	0.772 m ²
Planar wing span	1.602 m
Planar wing area	0.386 m ²
Planar wing mean chord	0.241 m
Planar wing root chord	0.242 m
Planar wing tip chord	0.240 m
Planar wing mean thickness	40.7 mm
Planar wing aspect ratio	6.64
Planar wing taper ratio	1.0
Planar wing t/c ratio	16.9%
Wing vertical section span	0.360 m
Wing vertical section area	0.086 m ²
Wing vertical section chord	0.240 m
Wing vertical section t/c ratio	16.9%
Box tail chord	0.209 m
Box tail width	0.314 m

Box tail height	0.186 m
Box tail total horizontal planform area	0.132 m ²
Box tail total vertical planform area	0.078 m ²
Box tail section t/c ratio	10%
Battery length	0.103 m
Battery width	0.178 m
Battery height	0.152 m
Battery volume	2788.4 cm ³
Battery energy capacity	1338.5 Wh
Battery maximum power	26.77 kW
HVPC maximum input power	26.77 kW
HVPC maximum output power	22.75 kW
Box-tail thruster number of stages	14.5
Box-tail thruster gap spacing	10.0 mm
Box-tail thruster stage length	0.012 m
Box-tail thruster duct length	0.175 m
Box-tail thruster total length	0.209 m
Box-tail thruster duct cross-sectional area	0.058 m ²
Box-tail thruster exit cross-sectional area	0.058 m ²
Box-tail thruster exit area ratio	1.0
Box-wing thruster number of stages	16.7
Box-wing thruster gap spacing	10.0 mm
Box-wing thruster stage length	0.012 m
Box-wing thruster duct length	0.201 m
Box-wing thruster total length	0.241 m
Box-wing thruster duct cross-sectional area	0.576 m ²
Box-wing thruster exit cross-sectional area	0.576 m ²
Box-wing thruster exit area ratio	1.0

Appendix R Package delivery aircraft mass breakdowns

Mass breakdowns for the package-delivery monoplane and box wing, taken directly from the optimization results, are given in Table 52 and Table 53 respectively.

Table 52: Mass breakdown for the monoplane.

Component	Mass (kg)	Mass / Total (-)
Fuselage pod	0.47	2.2%
Tail boom	0.41	2.0%
Wing	1.10	5.3%
Box tail	0.67	3.2%
Forward nacelles	0.91	4.4%
Forward booms	0.16	0.8%
Landing gear	0.76	3.6%
Payload	1.20	5.8%
Payload mount	0.30	1.4%
Battery	7.48	36.0%
Power converter	2.46	11.9%
Box-tail thruster	0.49	2.4%
Forward thrusters	1.27	6.1%
Box-tail thruster tilting mechanism	0.29	1.4%
Forward thrusters tilting mechanism	0.54	2.6%
Avionics	0.38	1.8%
Margin	1.89	9.1%
Total	20.77	100.0%

Table 53: Mass breakdown for the box wing aircraft.

Component	Mass (kg)	Mass / Total (-)
Fuselage pod	0.49	2.6%
Tail boom	0.32	1.7%
Wing	1.98	10.7%
Box tail	0.26	1.4%
Landing gear	0.68	3.6%
Payload	1.20	6.5%
Payload mount	0.30	1.6%
Battery	6.69	36.0%
Power converter	2.20	11.9%
Box-tail thruster	0.12	0.7%
Box-wing thruster	1.38	7.4%
Box-wing thruster tilting mechanism	0.84	4.5%
Box-tail thruster tilting mechanism	0.09	0.5%
Avionics	0.34	1.8%
Margin	1.69	9.1%
Total	18.58	100.0%

Appendix S Package delivery aircraft performance data

Time, distance travelled, and battery energy consumed for both package-delivery aircraft is provided in Table 54. This data is taken directly from the optimization results.

Table 54: Mission segment time, distance travelled, and battery energy consumed.

Mission segment	Monoplane			Box wing		
	Time (s)	Distance (km)	Battery energy (Wh)	Time (s)	Distance (km)	Battery energy (Wh)
Takeoff	5.0	n/a	41.5	5.0	n/a	37.2
Climb	1.0	0.0	2.4	1.0	0.0	2.1
Cruise out	392.6	10.0	609.4	396.2	10.0	547.5
Payload drop	20.0	n/a	166.2	20.0	n/a	148.7
Turn around	14.1	0.4	25.2	10.7	0.2	18.2
Cruise in	392.6	10.0	609.4	396.2	10.0	547.5
Landing	5.0	n/a	41.5	5.0	n/a	37.2

Detailed performance data, broken down by mission segment, is provided in Table 55 and Table 56 for the monoplane and box wing respectively. Note that the payload mass is not deducted from the aircraft mass after the payload drop, as the vehicle needs to be able to return with the payload if necessary. Therefore, all three hover segments (takeoff, payload drop, and landing) yield identical performance data. The same is true for both cruise segments (cruise out and cruise in).

Table 55: Performance data by mission segment for the monoplane.

Mission segment	Hover	Climb	Cruise	Bank	Units
Airspeed	n/a	25.5	25.5	25.5	m/s
Lift coefficient	n/a	1.04	1.04	1.20	-
Profile drag coefficient	n/a	492.9	492.9	514.8	Counts
Induced drag coefficient	n/a	433.3	433.3	577.7	Counts
Margin drag coefficient	n/a	92.6	92.6	109.3	Counts
Total drag coefficient	n/a	1018.9	1018.9	1201.8	Counts
Lift-to-drag ratio	n/a	10.2	10.2	10.0	-
Thrust (total)	224.0	32.1	19.9	23.5	N
Thrust (box-tail thruster)	69.5	10.1	6.4	7.5	N
Thrust (forward thrusters)	154.4	22.0	13.5	16.0	N
Thrust per thruster (box-tail thruster)	69.5	10.1	6.4	7.5	N
Thrust per thruster (forward thrusters)	77.2	11.0	6.8	8.0	N

Power (battery)	29.91	8.52	5.59	6.41	kW
Power (HVPC)	25.42	7.24	4.75	5.45	kW
Power (box-tail thruster)	8.24	2.29	1.50	1.73	kW
Power (forward thrusters)	17.18	4.96	3.25	3.73	kW
Power per thruster (box-tail thruster)	8.24	2.29	1.50	1.73	kW
Power per thruster (forward thrusters)	8.59	2.48	1.62	1.86	kW
Voltage (box-tail thruster)	10.00	6.02	5.14	5.41	kV
Voltage (forward thrusters)	9.31	5.65	4.81	5.07	kV
Thrust-to-power (box-tail thruster)	8.44	4.42	4.26	4.34	N/kW
Thrust-to-power (forward thrusters)	8.99	4.44	4.16	4.29	N/kW
Thrust density (box-tail thruster)	391.9	57.0	36.1	42.3	N/m ²
losses due to wall friction	3.3	7.1	6.8	6.9	N/m ²
Thrust density (forward thrusters)	368.9	52.5	32.3	38.2	N/m ²
losses due to wall friction	3.1	6.9	6.7	6.7	N/m ²
Power density (box-tail thruster)	46.44	12.90	8.48	9.73	kW/m ²
ionization	0.30	0.14	0.11	0.12	kW/m ²
acceleration	46.14	12.76	8.37	9.61	kW/m ²
Power density (forward thrusters)	41.05	11.84	7.75	8.90	kW/m ²
ionization	0.29	0.14	0.10	0.11	kW/m ²
acceleration	40.76	11.70	7.65	8.79	kW/m ²
Bulk velocity (box-tail thruster)	18.0	27.4	26.8	27.0	m/s
Bulk velocity (forward thrusters)	17.4	27.3	26.7	26.8	m/s
Exit velocity (box-tail thruster)	18.0	27.4	26.8	27.0	m/s
Exit velocity (forward thrusters)	17.4	27.3	26.7	26.8	m/s
Current density (box-tail thruster)	236.6	108.7	83.6	91.1	mA/m ²
Current density (forward thrusters)	206.6	97.9	75.1	81.9	mA/m ²
Stage current (box-tail thruster)	42.0	19.3	14.8	16.2	mA
per thruster	42.0	19.3	14.8	16.2	mA
Stage current (forward thrusters)	43.3	20.5	15.7	17.1	mA
per thruster	21.6	10.2	7.9	8.6	mA
Stage EAD pressure rise (box-tail thruster)	10.53	4.09	3.03	3.34	Pa

Stage EAD pressure rise (forward thrusters)	9.15	3.62	2.67	2.95	Pa
Stage electrode losses (box-tail thruster)	0.40	0.92	0.88	0.89	Pa
Stage electrode losses (forward thrusters)	0.37	0.91	0.87	0.88	Pa
Total pressure rise (box-tail thruster)	197.6	61.9	41.9	47.8	Pa
Total pressure rise (forward thrusters)	186.0	57.5	38.1	43.8	Pa

Table 56: Performance data by mission segment for the box wing.

Mission Segment	Hover	Climb	Cruise	Bank	Units
Segment distance	n/a	0.0	10.0	0.2	km
Segment battery energy	133.8	7.5	1971.1	65.5	kJ
Airspeed	n/a	23.2	25.2	19.2	m/s
Lift coefficient	n/a	0.71	0.60	1.20	-
Profile drag coefficient	n/a	237.1	229.6	274.0	Counts
Induced drag coefficient	n/a	447.0	321.8	1272.9	Counts
Margin drag coefficient	n/a	68.4	55.1	154.7	Counts
Total drag coefficient	n/a	752.6	606.6	1701.6	Counts
Lift-to-drag ratio	n/a	9.5	10.0	7.1	-
Thrust (total)	200.4	31.2	18.3	29.8	N
Thrust (box-tail thruster)	16.7	2.5	1.4	2.4	N
Thrust (box-wing thruster)	183.7	28.7	16.8	27.4	N
Power (battery)	26.77	7.54	4.98	6.14	kW
Power (HVPC)	22.75	6.41	4.23	5.22	kW
Power (box-tail thruster)	1.93	0.57	0.39	0.46	kW
Power (box-wing thruster)	20.83	5.84	3.84	4.76	kW
Voltage (box-tail thruster)	9.92	6.12	5.24	5.77	kV
Voltage (box-wing thruster)	9.72	5.89	4.98	5.57	kV
Thrust-to-power (box-tail thruster)	8.69	4.42	3.71	5.26	N/kW
Thrust-to-power (box-wing thruster)	8.82	4.91	4.38	5.74	N/kW
Thrust density (box-tail thruster)	287.1	43.0	24.6	41.4	N/m ²
losses due to wall friction	3.6	8.6	9.4	6.3	N/m ²
Thrust density (box-wing thruster)	318.8	49.8	29.2	47.5	N/m ²
losses due to wall friction	2.1	4.5	5.0	3.4	N/m ²

Power density (box-tail thruster)	33.04	9.73	6.61	7.88	kW/m ²
ionization	0.22	0.10	0.08	0.09	kW/m ²
acceleration	32.82	9.63	6.53	7.79	kW/m ²
Power density (box-wing thruster)	36.15	10.14	6.67	8.26	kW/m ²
ionization	0.24	0.11	0.09	0.10	kW/m ²
acceleration	35.90	10.03	6.58	8.17	kW/m ²
Bulk velocity (box-tail thruster)	15.4	24.9	26.3	21.1	m/s
Bulk velocity (box-wing thruster)	16.2	25.0	26.3	21.2	m/s
Exit velocity (box-tail thruster)	15.4	24.9	26.3	21.1	m/s
Exit velocity (box-wing thruster)	16.2	25.0	26.3	21.2	m/s
Current density (box-tail thruster)	227.5	108.1	85.6	92.8	mA/m ²
Current density (box-wing thruster)	220.7	101.7	79.0	87.6	mA/m ²
Stage current (box-tail thruster)	13.3	6.3	5.0	5.4	mA
Stage current (box-wing thruster)	127.2	58.6	45.5	50.5	mA
Stage EAD pressure rise (box-tail thruster)	10.28	4.19	3.14	3.68	Pa
Stage EAD pressure rise (box-wing thruster)	9.90	3.90	2.85	3.45	Pa
Stage electrode losses (box-tail thruster)	0.29	0.76	0.85	0.54	Pa
Stage electrode losses (box-wing thruster)	0.32	0.77	0.85	0.55	Pa
Total pressure rise (box-tail thruster)	145.4	49.8	33.3	45.7	Pa
Total pressure rise (box-wing thruster)	160.4	52.4	33.5	48.5	Pa

Appendix T MSD surveillance monoplane 3-view sketches

OpenVSP sketches of the MSD surveillance monoplane are shown in Figure 89 – Figure 91. All sketches are generated using dimensions from the design optimization results; they are therefore to scale.



Figure 89: Front view of the MSD surveillance monoplane.

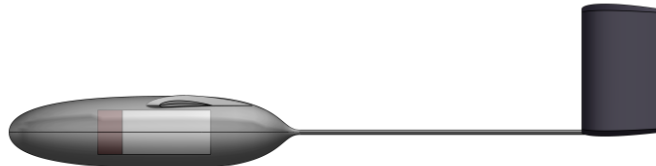


Figure 90: Side view of the MSD surveillance monoplane.

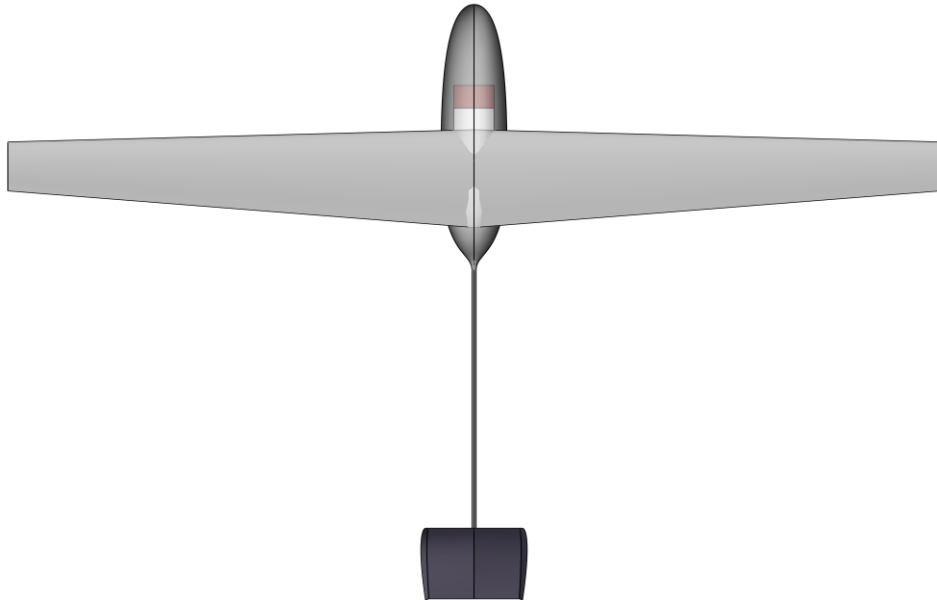


Figure 91: Top view of the MSD surveillance monoplane.

Appendix U MSD surveillance monoplane dimensional data

Detailed dimensional data for the MSD surveillance monoplane, taken from the optimization results, is given in Table 57. Number of thruster stages is treated as a continuous variable.

Table 57: Dimensional data for the MSD surveillance monoplane.

Overall length	1.383 m
Overall wingspan	3.028 m
Takeoff mass	4.2 kg
Takeoff weight	41.0 N
Wing loading	7.6 kg/m ²
Empty mass fraction	52.7%
Max thrust	4.33 N
Max power draw	1.05 kW
Fuselage pod length	0.657 m
Fuselage pod usable length	0.256 m
Fuselage pod width	0.163 m
Fuselage pod usable width	0.100 m
Fuselage pod height	0.163 m
Fuselage pod usable height	0.100 m
Tail boom length	1.383 m
Tail boom exposed length	0.725 m
Tail boom diameter	0.006 m
Tail boom wall thickness	2.00 mm
Planar wing span	3.028 m
Planar wing area	0.547 m ²
Planar wing mean chord	0.181 m
Planar wing root chord	0.241 m
Planar wing tip chord	0.120 m
Planar wing mean thickness	20.1 mm
Planar wing aspect ratio	16.77
Planar wing taper ratio	0.5
Planar wing t/c ratio	11.1%

Box tail chord	0.174 m
Box tail width	0.224 m
Box tail height	0.262 m
Box tail total horizontal planform area	0.078 m ²
Box tail total vertical planform area	0.091 m ²
Box tail section t/c ratio	10%
Battery length	0.056 m
Battery width	0.100 m
Battery height	0.100 m
Battery volume	561.1 cm ³
Battery energy capacity	269.3 Wh
Battery maximum power	1.35 kW
HVPC maximum input power	1.05 kW
HVPC maximum output power	0.89 kW
Tail thruster number of stages	12.1
Tail thruster gap spacing	10.0 mm
Tail thruster stage length	0.012 m
Tail thruster duct length	0.145 m
Tail thruster total length	0.174 m
Tail thruster duct cross-sectional area	0.059 m ²
Tail thruster exit cross-sectional area	0.059 m ²
Tail thruster exit area ratio	1

Appendix V MSD surveillance monoplane mass breakdown

A mass breakdown for the MSD surveillance monoplane, taken directly from the optimization results, is given in Table 58.

Table 58: Mass breakdown for the MSD surveillance monoplane.

Component	Mass (kg)	Mass / Total (-)
Fuselage pod	0.22	5.3%
Tail boom	0.17	4.1%
Wing	0.86	20.6%
Box tail	0.19	4.6%
Landing gear	0.15	3.6%
Payload	0.20	4.8%
Payload mount	0.05	1.2%
Battery	1.35	32.2%
Power converter	0.43	10.3%
Box-tail thruster	0.10	2.4%
Avionics	0.08	1.8%
Margin	0.38	9.1%
Total	4.18	100.0%

Appendix W MSD surveillance monoplane performance data

Detailed performance data for the MSD surveillance monoplane, broken down by mission segment, is provided in Table 59. This data is taken directly from the optimization results.

Table 59: Performance data by mission segment for the MSD surveillance monoplane.

Mission segment	Climb	Loiter	Bank	Units
Segment time	1.0	1800.0	6.0	s
Segment distance	0.0	19.6	0.1	km
Segment battery energy	0.3	268.0	1.1	Wh
Airspeed	10.8	10.8	10.8	m/s
Lift coefficient	1.04	1.04	1.20	-
Profile drag coefficient	296.6	296.6	316.7	Counts
Induced drag coefficient	257.5	257.5	343.3	Counts
Margin drag coefficient	55.4	55.4	66.0	Counts
Total drag coefficient	609.5	609.5	725.9	Counts
Lift-to-drag ratio	17.1	17.1	16.6	-
Thrust (total)	4.33	2.40	2.86	N
Power (battery)	1.05	0.54	0.65	kW
Power (HVPC)	0.89	0.46	0.55	kW
Thrust-to-power (tail thruster)	4.87	5.27	5.17	N/kW
Voltage (tail thruster)	8.05	6.39	6.83	kV
Thrust density (tail thruster)	73.9	41.0	48.8	N/m ²
losses due to wall friction	2.9	2.4	2.5	N/m ²
Power density (tail thruster)	15.17	7.78	9.43	kW/m ²
ionization	0.12	0.08	0.09	kW/m ²
acceleration	15.05	7.70	9.34	kW/m ²
Bulk velocity (tail thruster)	15.0	13.5	13.9	m/s
Exit velocity (tail thruster)	15.0	13.5	13.9	m/s
Current density (tail thruster)	154.3	99.4	112.8	mA/m ²
Stage current (tail thruster)	9.0	5.8	6.6	mA
Stage EAD pressure rise (tail thruster)	6.84	4.34	4.95	Pa
Stage electrode losses (tail thruster)	1.38	1.11	1.18	Pa

References

- [1] M. A. V. Chaban, "Deal Restricts Tourist Helicopter Flights Over New York," *The New York Times*, Feb. 01, 2016. Accessed: Mar. 05, 2023. [Online]. Available: <https://www.nytimes.com/2016/02/01/nyregion/deal-restricts-tourist-helicopter-flights-over-new-york.html>
- [2] P. D. Vascik and R. J. Hansman, "Scaling Constraints for Urban Air Mobility Operations: Air Traffic Control, Ground Infrastructure, and Noise," in *2018 Aviation Technology, Integration, and Operations Conference*, Atlanta, GA: American Institute of Aeronautics and Astronautics, 2018, pp. 1–26. doi: 10.2514/6.2018-3849.
- [3] D. Y. Gwak, D. Han, and S. Lee, "Sound quality factors influencing annoyance from hovering UAV," *Journal of Sound and Vibration*, vol. 489, 2020, doi: 10.1016/j.jsv.2020.115651.
- [4] A. J. Torija, Z. Li, and R. H. Self, "Effects of a hovering unmanned aerial vehicle on urban soundscapes perception," *Transportation Research Part D: Transport and Environment*, vol. 78, p. 102195, Jan. 2020, doi: 10.1016/j.trd.2019.11.024.
- [5] S. Barrett, A. Brown, and N. Gomez-Vega, "Silent, Solid-State Propulsion for Advanced Air Mobility Vehicles (submitted)," Phase I final report, NASA Innovative Advanced Concepts (NIAC), Feb. 2023.
- [6] E. A. Christenson and P. S. Moller, "Ion-Neutral Propulsion in Atmospheric Media," *AIAA Journal*, vol. 5, no. 10, pp. 1768–1773, 1967, doi: 10.2514/3.4302.
- [7] K. Masuyama and S. R. H. Barrett, "On the performance of electrohydrodynamic propulsion," *Proceedings of the Royal Society A: Mathematical, Physical and Engineering Sciences*, vol. 469, no. 2154, p. 20120623, 2013, doi: 10.1098/rspa.2012.0623.
- [8] N. Monrolin, F. Plouraboué, and O. Praud, "Electrohydrodynamic Thrust for In-Atmosphere Propulsion," *AIAA Journal*, vol. 55, no. 12, pp. 4296–4305, Sep. 2017, doi: 10.2514/1.j055928.
- [9] C. K. Gilmore and S. R. H. Barrett, "Electrohydrodynamic thrust density using positive corona-induced ionic winds for in-atmosphere propulsion," *Proceedings of the Royal Society A: Mathematical, Physical and Engineering Sciences*, vol. 471, no. 2175, p. 20140912, 2015, doi: 10.1098/rspa.2014.0912.
- [10] Y. He, M. Woolston, and D. Perreault, "Design and implementation of a lightweight high-voltage power converter for electro-aerodynamic propulsion," presented at the 2017 IEEE 18th Workshop on Control and Modeling for Power Electronics (COMPEL), Jul. 2017, pp. 1–9. doi: 10.1109/COMPEL.2017.8013315.
- [11] Y. He and D. J. Perreault, "Lightweight High-Voltage Power Converters for Electroaerodynamic Propulsion," *IEEE Journal of Emerging and Selected Topics in Industrial Electronics*, vol. 2, no. 4, pp. 453–463, Oct. 2021, doi: 10.1109/JESTIE.2021.3087950.

- [12] Z. Zhao, S. He, J. Zhu, J. Lan, Y. Yang, and Y. Huang, “Design of Magnetic Integrated Transformer for Lightweight High Voltage Power Supply to Electro-aerodynamic Propulsion System,” in *2022 IEEE International Power Electronics and Application Conference and Exposition (PEAC)*, Nov. 2022, pp. 1–5. doi: 10.1109/PEAC56338.2022.9959145.
- [13] H. Xu *et al.*, “Flight of an aeroplane with solid-state propulsion,” *Nature*, vol. 563, no. 7732, pp. 532–535, 2018, doi: 10.1038/s41586-018-0707-9.
- [14] A. Brown, H. Xu, C. K. Gilmore, and S. R. H. Barrett, “Solid-State Electroaerodynamic Aircraft Design Using Signomial Programming (under peer review),” *Journal of Aircraft*, 2023.
- [15] C. K. Gilmore, “Electro-Aerodynamic Thrust for Fixed-Wing Aircraft Propulsion,” PhD Thesis, Massachusetts Institute of Technology, 2016.
- [16] A. R. Gnadt, R. L. Speth, J. S. Sabnis, and S. R. H. Barrett, “Technical and environmental assessment of all-electric 180-passenger commercial aircraft,” *Progress in Aerospace Sciences*, vol. 105, pp. 1–30, Feb. 2019, doi: 10.1016/j.paerosci.2018.11.002.
- [17] H. Xu, Y. He, and S. R. H. Barrett, “A dielectric barrier discharge ion source increases thrust and efficiency of electroaerodynamic propulsion,” *Applied Physics Letters*, vol. 114, no. 25, p. 254105, Jun. 2019, doi: 10.1063/1.5100524.
- [18] H. Xu, N. Gomez-Vega, D. R. Agrawal, and S. R. H. Barrett, “Higher thrust-to-power with large electrode gap spacing electroaerodynamic devices for aircraft propulsion,” *Journal of Physics D: Applied Physics*, vol. 53, pp. 1–11, Oct. 2019, doi: 10.1088/1361-6463/ab4a4c.
- [19] N. Gomez-Vega, H. Xu, J. M. Abel, and S. R. H. Barrett, “Performance of decoupled electroaerodynamic thrusters,” *Applied Physics Letters*, vol. 118, no. 7, p. 074101, Feb. 2021, doi: 10.1063/5.0038208.
- [20] N. D. Wilde, H. Xu, N. Gomez-Vega, and S. R. H. Barrett, “A model of surface dielectric barrier discharge power,” *Applied Physics Letters*, vol. 118, no. 15, p. 154102, 2021, doi: 10.1063/5.0043339.
- [21] N. Gomez-Vega, J. D. Kambhampaty, and S. R. H. Barrett, “Mitigating reverse emission in electroaerodynamic thrusters,” *Journal of Physics D: Applied Physics*, vol. 55, no. 50, p. 505202, Nov. 2022, doi: 10.1088/1361-6463/ac9c0f.
- [22] C. K. Gilmore and S. R. H. Barrett, “Electroaerodynamic Thruster Performance as a Function of Altitude and Flight Speed,” *AIAA Journal*, vol. 56, no. 3, pp. 1105–1117, Dec. 2017, doi: 10.2514/1.j056138.
- [23] N. Gomez-Vega, A. Brown, H. Xu, and S. R. H. Barrett, “Model of Multistaged Ducted Thrusters for High-Thrust-Density Electroaerodynamic Propulsion,” *AIAA Journal*, vol. 61, no. 2, pp. 767–779, Feb. 2023, doi: 10.2514/1.J061948.
- [24] S. Chen, Y. Zhu, J. Tu, and F. Wang, “Numerical investigation of an electroaerodynamic driven aeroplane: electrical properties, ionic wind and flight performance,” *Journal of Physics D: Applied Physics*, vol. 52, p. 365203, Jun. 2019, doi: 10.1088/1361-6463/ab2b2a.

- [25] S. Coseru, D. Fabre, and F. Plouraboué, “Numerical study of ElectroAeroDynamic force and current resulting from ionic wind in emitter/collector systems,” *Journal of Applied Physics*, vol. 129, no. 10, p. 103304, Mar. 2021, doi: 10.1063/5.0041061.
- [26] J. R. Casado and A. D. Greig, “Solid State Atmosphere Breathing Plasma Propulsion for an Autonomous Mars Drone,” presented at the ASCEND Conference, American Institute of Aeronautics and Astronautics (AIAA), Nov. 2020. doi: 10.2514/6.2020-4021.
- [27] H. S. Poon, M. K. K. Lam, M. Chow, and W. J. Li, “Noiseless and vibration-free Ionic Propulsion technology for indoor surveillance blimps,” in *2009 IEEE International Conference on Robotics and Automation*, May 2009, pp. 2891–2896. doi: 10.1109/ROBOT.2009.5152843.
- [28] Z. He, P. Li, W. Wang, L. Shao, and X. Chen, “Design of indoor unmanned airship propelled by ionic wind,” *Journal of Physics: Conference Series*, vol. 1748, no. 6, p. 062011, Jan. 2021, doi: 10.1088/1742-6596/1748/6/062011.
- [29] V. Y. Khomich and I. E. Rebrov, “In-atmosphere electrohydrodynamic propulsion aircraft with wireless supply onboard,” *Journal of Electrostatics*, vol. 95, pp. 1–12, Oct. 2018, doi: 10.1016/j.elstat.2018.07.005.
- [30] D. S. Drew, N. O. Lambert, C. B. Schindler, and K. S. J. Pister, “Toward Controlled Flight of the Ionocraft: A Flying Microrobot Using Electrohydrodynamic Thrust With Onboard Sensing and No Moving Parts,” *IEEE Robotics and Automation Letters*, 2018, doi: 10.1109/LRA.2018.2844461.
- [31] A. Ieta and M. Chirita, “Electrohydrodynamic propeller for in-atmosphere propulsion; rotational device first flight,” *Journal of Electrostatics*, vol. 100, Jul. 2019, doi: 10.1016/j.elstat.2019.05.004.
- [32] M. Chirita and A. Ieta, “First Rotary Ionic Engine with Contra-Rotating Propellers,” *Journal of Propulsion and Power*, vol. 38, no. 6, pp. 893–900, Nov. 2022, doi: 10.2514/1.B38521.
- [33] J. R. Roth, “Aerodynamic flow acceleration using paraelectric and peristaltic electrohydrodynamic effects of a One Atmosphere Uniform Glow Discharge Plasma,” *Physics of Plasmas*, vol. 10, no. 5, pp. 2117–2126, May 2003, doi: 10.1063/1.1564823.
- [34] S. Sato, H. Furukawa, A. Komuro, M. Takahashi, and N. Ohnishi, “Successively accelerated ionic wind with integrated dielectric-barrier-discharge plasma actuator for low-voltage operation,” *Scientific Reports*, vol. 9, no. 1, p. 5813, Dec. 2019, doi: 10.1038/s41598-019-42284-w.
- [35] S. Sato, M. Sakurai, and N. Ohnishi, “Enhancement of electrohydrodynamic force with AC bias voltage in three-electrode dielectric barrier discharge plasma actuators,” *Journal of Applied Physics*, vol. 132, no. 11, p. 113301, Sep. 2022, doi: 10.1063/5.0100696.
- [36] F. O. Thomas, A. Kozlov, and T. C. Corke, “Plasma Actuators for Cylinder Flow Control and Noise Reduction,” *AIAA Journal*, vol. 46, no. 8, pp. 1921–1931, Aug. 2008, doi: 10.2514/1.27821.
- [37] X. Huang and X. Zhang, “Plasma Actuators for Noise Control,” *Aeroacoustics*, vol. 9, no. 4 & 5, pp. 679–704, Jan. 2010, doi: <https://doi.org/10.1260/1475-472X.9.4-5.67>.

- [38] T. K. Patel *et al.*, “Fundamental investigation using active plasma control to reduce blade–vortex interaction noise,” *International Journal of Aeroacoustics*, vol. 20, no. 8, pp. 1–31, Nov. 2021, doi: 10.1177/1475472X211052699.
- [39] W. Qiu, X. Lingzhi, L. Yang, Q. Zhang, X. Lei, and C. Li, “Experimental Study on the Velocity and Efficiency Characteristics of a Serial Staged Needle Array-Mesh Type EHD Gas Pump,” *Plasma Science and Technology*, vol. 13, no. 6, pp. 693–697, Dec. 2011, doi: 10.1088/1009-0630/13/6/11.
- [40] M. J. Johnson and D. B. Go, “Recent advances in electrohydrodynamic pumps operated by ionic winds: a review,” *Plasma Sources Science and Technology*, vol. 27, no. 5, May 2018, doi: 10.1088/1361-6595/aabebe.
- [41] M. J. Zeng, Z. G. Qu, and J. F. Zhang, “Negative corona discharge and flow characteristics of a two-stage needle-to-ring configuration ionic wind pump for temperature and relative humidity,” *International Journal of Heat and Mass Transfer*, vol. 201, p. 123561, Feb. 2023, doi: 10.1016/j.ijheatmasstransfer.2022.123561.
- [42] Y. Peng, D. Li, X. Yang, Z. Ma, and Z. Mao, “A Review on Electrohydrodynamic (EHD) Pump,” *Micromachines*, vol. 14, no. 321, pp. 1–23, Feb. 2023, doi: 10.3390/mi14020321.
- [43] M. E. Franke and L. E. Hogue, “Electrostatic Cooling of a Horizontal Cylinder,” *Journal of Heat Transfer*, vol. 113, no. 3, pp. 544–548, Aug. 1991, doi: 10.1115/1.2910597.
- [44] J. Mathew and F. C. Lai, “Enhanced heat transfer in a horizontal channel with double electrodes,” in *IAS '95. Conference Record of the 1995 IEEE Industry Applications Conference Thirtieth IAS Annual Meeting*, Oct. 1995, pp. 1472–1479. doi: 10.1109/IAS.1995.530476.
- [45] A. Ongkodjojo Ong, A. R. Abramson, and N. C. Tien, “Electrohydrodynamic Microfabricated Ionic Wind Pumps for Thermal Management Applications,” *Journal of Heat Transfer*, vol. 136, no. 6, Mar. 2014, doi: 10.1115/1.4026807.
- [46] M. Rickard, D. Dunn-Rankin, F. Weinberg, and F. Carleton, “Characterization of ionic wind velocity,” *Journal of Electrostatics*, vol. 63, no. 6, pp. 711–716, Jun. 2005, doi: 10.1016/j.elstat.2005.03.033.
- [47] H.-J. Kim, B. Han, Y.-J. Kim, and S.-J. Yoa, “Characteristics of an electrostatic precipitator for submicron particles using non-metallic electrodes and collection plates,” *Journal of Aerosol Science*, vol. 41, no. 11, pp. 987–997, Nov. 2010, doi: 10.1016/j.jaerosci.2010.08.001.
- [48] A. Sudrajad and A. F. Yusof, “Review of Electrostatic Precipitator Device for Reduce of Diesel Engine Particulate Matter,” *Energy Procedia*, vol. 68, pp. 370–380, Apr. 2015, doi: 10.1016/j.egypro.2015.03.268.
- [49] A. Afshari *et al.*, “Electrostatic Precipitators as an Indoor Air Cleaner - A Literature Review,” *Sustainability*, vol. 12, no. 21, p. 8774, Jan. 2020, doi: 10.3390/su12218774.
- [50] L. Wescott, *Wind and sand: the story of the Wright brothers at Kitty Hawk*. New York: Harry N Abrams Inc, 1983.

- [51] T. D. Crouch, *First flight: the Wright Brothers and the invention of the airplane*. in Handbook, no. 159. Washington, D.C: Division of Publications, Harpers Ferry Center, National Park Service, U.S. Department of the Interior, 2002.
- [52] “1909 Wright Military Flyer,” *National Air and Space Museum*. https://airandspace.si.edu/collection-objects/1909-wright-military-flyer/nasm_A19120001000 (accessed Feb. 13, 2023).
- [53] Y. Liu, S. Huang, and L. Zhu, “Influence of humidity and air pressure on the ion mobility based on drift tube method,” *CSEE Journal of Power and Energy Systems*, vol. 1, no. 3, pp. 37–41, Sep. 2015, doi: 10.17775/CSEEJPES.2015.00033.
- [54] B. Zhang, J. He, and Y. Ji, “Dependence of the average mobility of ions in air with pressure and humidity,” *IEEE Transactions on Dielectrics and Electrical Insulation*, vol. 24, no. 2, pp. 923–929, Apr. 2017, doi: 10.1109/TDEI.2017.006542.
- [55] J. A. Geurst, “Theory of Space-Charge-Limited Currents in Thin Semiconductor Layers,” *Physica Status Solidi B*, vol. 15, no. 1, pp. 107–118, 1966, doi: 10.1002/pssb.19660150108.
- [56] A. A. Grinberg, S. Luryi, M. R. Pinto, and N. L. Schryer, “Space-Charge-Limited Current in a Film,” *IEEE Transactions on Electron Devices*, vol. 36, no. 6, pp. 1162–1170, Jun. 1989, doi: 10.1109/16.24363.
- [57] P. De Visschere, “Geometry dependence of 2-dimensional space-charge-limited currents,” *Journal of Electrostatics*, vol. 84, pp. 81–89, Dec. 2016, doi: 10.1016/j.elstat.2016.09.005.
- [58] L. Pekker and M. Young, “Model of Ideal Electrohydrodynamic Thruster,” *Journal of Propulsion and Power*, vol. 27, no. 4, pp. 786–792, Jul. 2011, doi: 10.2514/1.b34097.
- [59] J. Lemetayer, C. Marion, D. Fabre, and F. Plouraboué, “Multi-inception patterns of emitter array/collector systems in DC corona discharge,” *J. Phys. D: Appl. Phys.*, vol. 55, no. 18, p. 185203, Feb. 2022, doi: 10.1088/1361-6463/ac4e35.
- [60] E. Özkaya, N. R. Gauger, J. A. Hay, and F. Thiele, “Efficient Design Optimization of Acoustic Liners for Engine Noise Reduction,” *AIAA Journal*, vol. 59, no. 3, pp. 1–17, Mar. 2020, doi: 10.2514/1.J057776.
- [61] S. R. H. Barrett, H. Xu, A. Brown, and N. Gomez Vega, “Ducted Electroaerodynamic Thrusters,” United States Patent 63/252390 (filed), Oct. 05, 2022
- [62] D. P. Raymer, *Aircraft design: a conceptual approach*, 5th ed. in AIAA education series. Reston, VA: American Institute of Aeronautics and Astronautics, 2012.
- [63] W. Hoburg and P. Abbeel, “Geometric Programming for Aircraft Design Optimization,” *AIAA Journal*, vol. 52, no. 11, pp. 2414–2426, 2014, doi: 10.2514/1.J052732.
- [64] N. Gomez Vega, “Advances in electroaerodynamic thrusters for aircraft propulsion,” PhD Thesis, Massachusetts Institute of Technology, Cambridge, MA, 2023.
- [65] B. J. Brelje and J. R. R. A. Martins, “Electric, hybrid, and turboelectric fixed-wing aircraft: A review of concepts, models, and design approaches,” *Progress in Aerospace Sciences*, vol. 104, pp. 1–19, Jan. 2019, doi: 10.1016/j.paerosci.2018.06.004.

- [66] J. Chin, K. Look, E. O. McNichols, D. Hall, J. Gray, and S. L. Schnulo, “Battery Cell-to-Pack Scaling Trends for Electric Aircraft,” in *AIAA Propulsion and Energy 2021 Forum*, Reston, Virginia: American Institute of Aeronautics and Astronautics, Aug. 2021. doi: 10.2514/6.2021-3316.
- [67] V. Viswanathan *et al.*, “The challenges and opportunities of battery-powered flight,” *Nature*, vol. 601, pp. 519–525, 2022, doi: <https://doi.org/10.1038/s41586-021-04139-1>.
- [68] S. Sripad and V. Viswanathan, “The promise of energy-efficient battery-powered urban aircraft,” *Proceedings of the National Academy of Sciences*, vol. 118, no. 45, p. e2111164118, Oct. 2021, doi: <https://doi.org/10.1073/pnas.2111164118>.
- [69] M. Clarke and J. J. Alonso, “Lithium–Ion Battery Modeling for Aerospace Applications,” *Journal of Aircraft*, vol. 58, no. 6, pp. 1–13, Nov. 2021, doi: 10.2514/1.C036209.
- [70] M. A. Clarke and J. J. Alonso, “Forecasting the Operational Lifetime of Battery-Powered Electric Aircraft,” *Journal of Aircraft*, vol. 60, no. 1, pp. 1–9, Jan. 2023, doi: 10.2514/1.c036851.
- [71] N. Perovich, “Design Studies for Future EAD-Propelled Aircraft,” Master’s Thesis, Massachusetts Institute of Technology, 2022.
- [72] M. Streetly and A. Parakala, “AeroVironment Raven,” in *Jane’s All the World’s Aircraft: Unmanned, 2019–2020*, IHS, 2019, pp. 262–265.
- [73] “Soldier Unmanned Aircraft System (SUAS),” www.army.mil. https://www.army.mil/article/239374/soldier_unmanned_aircraft_system_suas (accessed Feb. 15, 2023).
- [74] M. Rickard, D. Dunn-Rankin, F. Weinberg, and F. Carleton, “Maximizing ion-driven gas flows,” *Journal of Electrostatics*, vol. 64, no. 6, pp. 368–376, Jun. 2006, doi: 10.1016/j.elstat.2005.09.005.
- [75] W. Qiu, L. Xia, X. Tan, and L. Yang, “The velocity characteristics of a serial-staged EHD gas pump in air,” *IEEE Transactions on Plasma Science*, vol. 38, no. 10, pp. 2848–2853, Oct. 2010, doi: 10.1109/TPS.2010.2060500.
- [76] S. R. H. Barrett, H. Xu, A. Brown, N. Gomez Vega, and N. Perovich, “Surface-Integrated Electroaerodynamic Thrusters,” United States Patent 63/288731 (filed), Dec. 13, 2021.
- [77] Snorri Gudmundsson, *General Aviation Aircraft Design: Applied Methods and Procedures*. Kidlington, Oxford, UK: Butterworth-Heinemann, 2014.
- [78] P. G. Kirschen and W. W. Hoburg, “The Power of Log Transformation: A Comparison of Geometric and Signomial Programming with General Nonlinear Programming Techniques for Aircraft Design Optimization,” in *AIAA/ASCE/AHS/ASC Structures, Structural Dynamics, and Materials Conference*, Kissimmee, FL: American Institute of Aeronautics and Astronautics, 2018, pp. 1–11. doi: 10.2514/6.2018-0655.
- [79] E. Burnell, N. B. Damen, and W. Hoburg, “GPkit: a Human-Centered Approach to Convex Optimization in Engineering Design,” in *Proceedings of the 2020 CHI Conference on Human Factors in Computing Systems*, Honolulu, HI, 2020. doi: 10.1145/3313831.3376412.

- [80] W. Hoburg, P. Kirschen, and P. Abbeel, “Data fitting with geometric-programming-compatible softmax functions,” *Optimization and Engineering*, vol. 17, pp. 897–918, 2016, doi: 10.1007/s11081-016-9332-3.
- [81] M. Burton and W. Hoburg, “Solar and Gas Powered Long-Endurance Unmanned Aircraft Sizing via Geometric Programming,” *Journal of Aircraft*, vol. 55, no. 1, pp. 212–225, 2018, doi: 10.2514/1.C034405.
- [82] A. Brown and W. L. Harris, “Vehicle Design and Optimization Model for Urban Air Mobility,” *Journal of Aircraft*, vol. 57, no. 6, pp. 1003–1013, Nov. 2020, doi: 10.2514/1.c035756.
- [83] A. R. Gnadt, S. Isaacs, R. Price, M. Dethy, and C. Chappelle, “Hybrid Turbo-Electric STOL Aircraft for Urban Air Mobility,” in *AIAA SciTech 2019 Forum*, San Diego, CA: American Institute of Aeronautics and Astronautics, 2019, pp. 1–22. doi: 10.2514/6.2019-0531.
- [84] C. Courtin and R. J. Hansman, “Model Development for a Comparison of VTOL and STOL Electric Aircraft Using Geometric Programming,” in *AIAA Aviation 2019 Forum*, Dallas, TX, Jun. 2019, pp. 1–18. doi: <https://doi.org/10.2514/6.2019-3477>.
- [85] P. G. Kirschen, M. A. York, B. Ozturk, and W. W. Hoburg, “Application of Signomial Programming to Aircraft Design,” *Journal of Aircraft*, vol. 55, no. 3, pp. 1–23, May 2018, doi: 10.2514/1.C034378.
- [86] D. K. Hall, A. Dowdle, J. Gonzalez, L. Trollinger, and W. Thalheimer, “Assessment of a Boundary Layer Ingesting Turboelectric Aircraft Configuration using Signomial Programming,” in *Aviation Technology, Integration, and Operations Conference*, Atlanta, GA, 2018, pp. 1–16. doi: 10.2514/6.2018-3973.
- [87] D. Chadel *et al.*, “Conceptual Design of Distributed Electrified Boundary Layer Ingesting Propulsors for the CHEETA Aircraft Concept,” presented at the AIAA Propulsion and Energy Forum, American Institute of Aeronautics and Astronautics, 2021, pp. 1–16. doi: 10.2514/6.2021-3287.
- [88] A. P. Dowdle, D. K. Hall, and J. H. Lang, “Electric Propulsion Architecture Assessment via Signomial Programming,” in *AIAA/IEEE Electric Aircraft Technologies Symposium*, Cincinnati, OH, Jul. 2018, pp. 1–23. doi: <https://doi.org/10.2514/6.2018-5026>.
- [89] M. J. Duffy, R. Lacy, M. Stauffer, and R. Hupp, “A Study in Reducing the Cost of Vertical Flight with Electric Propulsion,” in *AIAA Aviation Forum*, American Institute of Aeronautics and Astronautics, Jun. 2017, pp. 1–24. doi: 10.2514/6.2017-3442.
- [90] B. J. Brelje and J. R. Martins, “Development of a Conceptual Design Model for Aircraft Electric Propulsion with Efficient Gradients,” in *AIAA Propulsion and Energy Forum*, Cincinnati, OH: American Institute of Aeronautics and Astronautics, Jul. 2018. doi: 10.2514/6.2018-4979.
- [91] M. Clarke, J. Smart, E. M. Botero, W. Maier, and J. J. Alonso, “Strategies for Posing a Well-Defined Problem for Urban Air Mobility Vehicles,” in *AIAA SciTech Forum*, San Diego, CA: American Institute of Aeronautics and Astronautics (AIAA), Jan. 2019. doi: 10.2514/6.2019-0818.

- [92] Mark Drela, “Wing Bending Calculations (Lab 10 Lecture Notes),” MIT OpenCourseWare, 2006. Accessed: Oct. 19, 2022. [Online]. Available: https://ocw.mit.edu/courses/16-01-unified-engineering-i-ii-iii-iv-fall-2005-spring-2006/c5f687b07f1a376a5c785aab490c06ef_spl10.pdf
- [93] M. Drela, “XFOIL: An Analysis and Design System for Low Reynolds Number Airfoils,” in *Low Reynolds Number Aerodynamics*, T. J. Mueller, Ed., in Lecture Notes in Engineering. Berlin, Heidelberg: Springer, 1989, pp. 1–12. doi: 10.1007/978-3-642-84010-4_1.
- [94] M. Drela, “Lab 8 Notes - Basic Aircraft Design Rules,” Massachusetts Institute of Technology, Cambridge, MA, Unified Engineering notes, Apr. 2006. [Online]. Available: <https://ocw.mit.edu/courses/16-01-unified-engineering-i-ii-iii-iv-fall-2005-spring-2006/resources/spl8/>
- [95] T. M. Reichert and C. D. Robertson, “Snowbird | Technical Information,” *Aerovelo*. <http://www.aerovelo.com/press-releases> (accessed Mar. 06, 2023).
- [96] *Airplane Flying Handbook (FAA-H-8083-3C)*. U.S. Department of Transportation, 2021.
- [97] “14 CFR Part 23 -- Airworthiness Standards: Normal Category Airplanes,” *Electronic Code of Federal Regulations*. <https://www.ecfr.gov/current/title-14/chapter-I/subchapter-C/part-23> (accessed Mar. 01, 2023).
- [98] M. Drela, “RE: Advice on EAD Aircraft Design (email correspondence with the author),” Feb. 03, 2022.
- [99] “Google Wing: how it works,” *Wing*. <https://wing.com/how-it-works/> (accessed Sep. 22, 2022).
- [100] “Amazon Prime Air prepares for drone deliveries,” *About Amazon*, Jun. 13, 2022. <https://www.aboutamazon.com/news/transportation/amazon-prime-air-prepares-for-drone-deliveries> (accessed Oct. 17, 2022).
- [101] N. Boysen, S. Fedtke, and S. Schwerdfeger, “Last-mile delivery concepts: a survey from an operational research perspective,” *OR Spectrum*, vol. 43, no. 1, pp. 1–58, Mar. 2021, doi: 10.1007/s00291-020-00607-8.
- [102] M. Elsayed and M. Mohamed, “The impact of airspace regulations on unmanned aerial vehicles in last-mile operation,” *Transportation Research Part D: Transport and Environment*, vol. 87, p. 102480, Oct. 2020, doi: 10.1016/j.trd.2020.102480.
- [103] J. K. Stolaroff, C. Samaras, E. R. O’Neill, A. Lubers, A. S. Mitchell, and D. Ceperley, “Energy use and life cycle greenhouse gas emissions of drones for commercial package delivery,” *Nature Communications*, vol. 9, no. 1, p. 409, Feb. 2018, doi: 10.1038/s41467-017-02411-5.
- [104] J. Gothe-Snape, “Google-affiliated drone delivery service found to be exceeding noise limits,” *ABC News*, Sep. 11, 2019. <https://www.abc.net.au/news/2019-09-12/canberra-delivery-drone-noise-levels-revealed/11503262> (accessed Oct. 17, 2022).
- [105] S. Robinson, “‘Do it somewhere else’: Glendale residents asking Walmart to stop drone delivery service,” *Arizona’s Family*, Jan. 06, 2023.

<https://www.azfamily.com/video/2023/01/07/glendale-residents-asking-walmart-stop-drone-deliveries/> (accessed Feb. 01, 2023).

- [106] G. Warwick, “The Week In Technology, June 20-24, 2022 | Aviation Week Network,” Jun. 20, 2022. https://aviationweek.com/aerospace/week-technology-june-20-24-2022?elq2=fe0d29ce60404ae287d0937da2ddc7be&sp_eh=b3374dfbe97fe67b4c3beb636192f3726cf2e89c0eebff51c036607de9a6ee41&utm_campaign=33384&utm_emailname=A_W_News_Aerospace_20220620&utm_medium=email&utm_rid=CPEN1000003329014 (accessed Sep. 22, 2022).
- [107] “Choice 20 oz. White Poly Paper Hot Cup and Lid - 100/Pack,” *WebstaurantStore*. <https://www.webstaurantstore.com/choice-20-oz-white-poly-paper-hot-cup-and-lid-pack/99920W100.html> (accessed Oct. 12, 2022).
- [108] L. Getson, “Take-Out Packaging Buying Guide,” *CiboWares*, May 18, 2017. <https://cibowares.com/blogs/news/take-out-packaging-buying-guide> (accessed Oct. 12, 2022).
- [109] R. A. McDonald and J. R. Gloudemans, “Open Vehicle Sketch Pad: An Open Source Parametric Geometry and Analysis Tool for Conceptual Aircraft Design,” in *AIAA SciTech Forum*, San Diego, CA: American Institute of Aeronautics and Astronautics, Jan. 2022. doi: 10.2514/6.2022-0004.
- [110] A. S. Hahn, “Next Generation NASA GA Advanced Concept,” *SAE Technical Paper #:* 2006-01-2430, no. 724, pp. 776–790, 2006, doi: 10.4271/2006-01-2430.
- [111] L. G. Hector and H. L. Schultz, “The Dielectric Constant of Air at Radiofrequencies,” *Physics*, vol. 7, no. 4, pp. 133–136, Apr. 1936, doi: 10.1063/1.1745374.
- [112] S. Macheret, M. Shneider, and R. Miles, “Modeling of air plasma generation by electron beams and high-voltage pulses,” in *31st Plasmadynamics and Lasers Conference*, in Fluid Dynamics and Co-located Conferences. American Institute of Aeronautics and Astronautics, 2000. doi: 10.2514/6.2000-2569.
- [113] Y. P. Raizer, *Gas Discharge Physics*. Berlin: Springer-Verlag, 1991.
- [114] H. Xu, “Experiments in Electroaerodynamic Propulsion,” PhD Thesis, Massachusetts Institute of Technology, 2020.
- [115] K. Kostecka, “Americium - from discovery to the smoke detector and beyond,” *Bulletin for the History of Chemistry*, vol. 33, no. 2, pp. 89–93, 2008.
- [116] “Tungsten-Re3% Wire .0003.” <https://espimetals.com/shop/tungsten-re3-wire-0003.html> (accessed Jan. 27, 2023).
- [117] M. A. Tepeschuk, F. Banag, B. Mcadam, T. Gribben, and Z. Mengad, “A 7.8W continuous and 19.6W burst output power fully integrated 2S Class-D amplifier with 0.005% THD+N,” in *2016 IEEE 7th Latin American Symposium on Circuits & Systems (LASCAS)*, Feb. 2016, pp. 35–38. doi: 10.1109/LASCAS.2016.7451003.

- [118] J. M. Rheaume and C. Lents, “Energy Storage for Commercial Hybrid Electric Aircraft,” in *SAE 2016 Aerospace Systems and Technology Conference*, Hartford, CT, Sep. 2016. doi: 10.4271/2016-01-2014.
- [119] “Battery Modules - Driving Efficiency Speed to Market,” *A123 Systems*. <http://www.a123systems.com/automotive/products/modules/> (accessed Jan. 30, 2023).
- [120] M. Mo and K. Bonatakis, “Approaching wildlife with drones: using scientific literature to identify factors to consider for minimising disturbance,” *Australian Zoologist*, vol. 42, no. 1, pp. 1–29, Jun. 2021, doi: 10.7882/az.2021.015.
- [121] S. Mazumdar, “Drone Applications in Wildlife Research—A Synoptic Review,” in *Environmental Informatics*, Singapore: Springer, 2022, pp. 237–257. doi: 10.1007/978-981-19-2083-7_14.
- [122] A. M. Stoll, J. Bevirt, M. D. Moore, W. J. Fredericks, and N. K. Borer, “Drag Reduction Through Distributed Electric Propulsion,” in *14th AIAA Aviation Technology, Integration, and Operations Conference*, Atlanta, GA, Jun. 2014, pp. 1–10. doi: 10.2514/6.2014-2851.
- [123] A. M. Stoll, “Comparison of CFD and Experimental Results of the LEAPTech Distributed Electric Propulsion Blown Wing,” in *15th AIAA Aviation Technology, Integration, and Operations Conference*, Dallas, TX, Jun. 2015, pp. 1–9. doi: 10.2514/6.2015-3188.
- [124] K. A. Deere, J. K. Viken, S. A. Viken, M. B. Carter, M. R. Wiese, and N. Farr, “Computational Analysis of a Wing Designed for the X-57 Distributed Electric Propulsion Aircraft,” in *35th AIAA Applied Aerodynamics Conference*, Denver, CO, 2017, pp. 1–22. doi: 10.2514/6.2017-3925.
- [125] X. Fei, B. German, and M. D. Patterson, “Exploring the Effects of Installation Geometry in High-Lift Propeller Systems,” in *2018 AIAA Aerospace Sciences Meeting*, Kissimmee, FL, 2018. doi: 10.2514/6.2018-0277.
- [126] C. Casses *et al.*, “Impact of Propulsion Modeling Approach on High-Lift Force Prediction of Propeller-Blown Wings,” in *AIAA AVIATION 2022 Forum*, Reston, Virginia: American Institute of Aeronautics and Astronautics, Jun. 2022. doi: 10.2514/6.2022-3302.
- [127] G. J. J. Ruijgrok, *Elements of Aviation Acoustics*. Delft University Press, 2004.
- [128] J. Revell, G. J. Healy, and J. Gibson, “Methods for the prediction of airframe aerodynamic noise,” in *2nd Aeroacoustics Conference*, Reston, Virginia: American Institute of Aeronautics and Astronautics, Mar. 1975. doi: 10.2514/6.1975-539.
- [129] J. Revell, “Induced Drag Effect on Airframe Noise,” in *2nd Aeroacoustics Conference*, Reston, Virginia: American Institute of Aeronautics and Astronautics, Mar. 1975. doi: 10.2514/6.1975-487.
- [130] M. R. Fink, “Airframe Noise Prediction Method,” US Department of Transportation, Federal Aviation Administration, Washington, DC, 1977.
- [131] M. E. Goldstein, *Aeroacoustics*. McGraw-Hill International Book Company, 1976.

- [132] C. Baird, C. L. Enloe, T. E. McLaughlin, and J. W. Baughn, “Acoustic testing of the dielectric barrier discharge (DBD) plasma actuator,” in *43rd AIAA Aerospace Sciences Meeting and Exhibit - Meeting Papers*, 2005, pp. 2637–2646. doi: 10.2514/6.2005-565.
- [133] B. Eliasson, M. Hirth, and U. Kogelschatz, “Ozone synthesis from oxygen in dielectric barrier discharges,” *Journal of Physics D: Applied Physics*, vol. 20, no. 11, p. 1421, Nov. 1987, doi: 10.1088/0022-3727/20/11/010.
- [134] D. Nuvolone, D. Petri, and F. Voller, “The effects of ozone on human health,” *Environmental Science and Pollution Research*, vol. 25, no. 9, pp. 8074–8088, Mar. 2018, doi: 10.1007/s11356-017-9239-3.
- [135] H. Schlichting and K. Gersten, *Boundary-Layer Theory*, 9th ed. Springer-Verlag Berlin Heidelberg, 2017.
- [136] M. Drela and H. Youngren, “AVL Overview.” <https://web.mit.edu/drela/Public/web/avl/> (accessed Feb. 22, 2023).
- [137] D. Schiktanz and D. Scholz, “Box Wing Fundamentals - an Aircraft Design Perspective,” in *German Aerospace Conference*, Bremen, Germany, 2011, pp. 601–615.
- [138] Aldo Frediani and Guido Montanari, “Best Wing System - An Exact Solution of the Prandtl’s Problem,” in *Variational Analysis and Aerospace Engineering*, in Springer Optimization and Its Applications, vol. 33. New York, NY: Springer, 2009. doi: 10.1007/978-0-387-95857-6.
- [139] M. Nita and D. Scholz, “Estimating the Oswald Factor from Basic Aircraft Geometrical Parameters,” *Deutscher Luft- und Raumfahrtkongress*, pp. 1–19, 2012.